This document was prepared by the DUNE collaboration using the resources of the Fermi National Accelerator Laboratory (Fermilab), a U.S. Department of Energy, Office of Science, HEP User Facility. Fermilab is managed by Fermi Research Alliance, LLC (FRA), acting under Contract No. DE-AC02-07CH11359.

The DUNE collaboration also acknowledges the international, national, and regional funding agencies supporting the institutions who have contributed to completing this Technical Design Report.

Authors

B. Abi,[129] R. Acciarri,[56] Mario A. Acero,[8] G. Adamov,[59] D. Adams,[15] M. Adinolfi,[14] Z. Ahmad,[163] J. Ahmed,[166] T. Alion,[153] S. Alonso Monsalve,[18] C. Alt,[49] J. Anderson,[4] C. Andreopoulos,[109] M. P. Andrews,[56] F. Andrianala,[2] S. Andringa,[103] A. Ankowski,[143] J. Anthony,[28] M. Antonova,[72] S. Antusch,[9] A. Aranda Fernandez,[36] A. Ariga,[10] L. O. Arnold,[39] M. A. Arroyave,[48] J. Asaadi,[157] A. Aurisano,[34] V. Aushev,[101] D. Autiero,[81] F. Azfar,[129] H. Back,[130] J. J. Back,[166] C. Backhouse,[161] P. Baesso,[14] L. Bagby,[56] R. Bajou,[1] S. Balasubramanian,[170] P. Baldi,[23] B. Bambah,[70] F. Barao,[103, 105] G. Barenboim,[72] G. J. Barker,[166] W. Barkhouse,[123] C. Barnes,[116] G. Barr,[129] J. Barranco Monarca,[64] N. Barros,[103, 106] J. L. Barrow,[155, 56] A. Bashyal,[128] V. Basque,[114] F. Bay,[122] J. L. Bazo Alba,[137] J. F. Beacom,[127] E. Bechetoille,[81] B. Behera,[38] L. Bellantoni,[56] G. Bellettini,[135] V. Bellini,[74] O. Beltramello,[18] D. Belver,[19] N. Benekos,[18] F. Bento Neves,[104] J. Berger,[136] S. Berkman,[56] P. Bernardini,[144] R. M. Berner,[10] H. Berns,[22] S. Bertolucci,[73] M. Betancourt,[56] Y. Bezawada,[22] M. Bhattacharjee,[86] B. Bhuyan,[86] S. Biagi,[152] J. Bian,[23] M. Biassoni,[76] K. Biery,[56] B. Bilki,[11] M. Bishai,[15] A. Bitadze,[114] A. Blake,[107] B. Blanco Siffert,[55] F. D. M. Blaszczyk,[56] G. C. Blazey,[124] E. Blucher,[32] J. Boissevain,[110] S. Bolognesi,[17] T. Bolton,[98] M. Bonesini,[76] M. Bongrand,[102] F. Bonini,[15] A. Booth,[153] C. Booth,[146] S. Bordoni,[18] A. Borkum,[153] T. Boschi,[47] N. Bostan,[90] P. Bour,[41] S. B. Boyd,[166] D. Boyden,[124] J. Bracinik,[12] D. Braga,[56] D. Brailsford,[107] A. Brandt,[157] J. Bremer,[18] C. Brew,[142] E. Brianne,[114] S. J. Brice,[56] C. Brizzolari,[76] C. Bromberg,[117] G. Brooijmans,[39] J. Brooke,[14] A. Bross,[56] G. Brunetti,[131] N. Buchanan,[38] H. Budd,[140] D. Caiulo,[81] P. Calafiura,[108] J. Calcutt,[117] M. Calin,[16] S. Calvez,[38] E. Calvo,[19] L. Camilleri,[39] A. Caminata,[75] M. Campanelli,[161] D. Caratelli,[56] G. Carini,[15] B. Carlus,[81] P. Carniti,[76] I. Caro Terrazas,[38] H. Carranza,[157] A. Castillo,[145] C. Castromonte,[89] C. Cattadori,[76] F. Cavalier,[102] F. Cavanna,[56] S. Centro,[131] G. Cerati,[56] A. Cervelli,[73] A. Cervera Villanueva,[72] M. Chalifour,[18] C. Chang,[25] E. Chardonnet,[1] A. Chatterjee,[136] S. Chattopadhyay,[163] J. Chaves,[132] H. Chen,[15] M. Chen,[23] Y. Chen,[10] D. Cherdack,[69] C. Chi,[39] S. Childress,[56] A. Chiriacescu,[16] K. Cho,[97] S. Choubey,[66] A. Christensen,[38] D. Christian,[56] G. Christodoulou,[18] E. Church,[130] P. Clarke,[50] T. E. Coan,[150] A. G. Cocco,[78] J. A. B. Coelho,[102] E. Conley,[46] J. M. Conrad,[115] M. Convery,[143] L. Corwin,[147] P. Cotte,[17] L. Cremaldi,[119] L. Cremonesi,[161] J. I. Crespo-Anadón,[39] E. Cristaldo,[6] R. Cross,[107] C. Cuesta,[19] Y. Cui,[25] D. Cussans,[14] M. Dabrowski,[15] H. da Motta,[30] L. Da Silva Peres,[55] Q. David,[81] G. S. Davies,[119] S. Davini,[75] J. Dawson,[1] K. De,[157] R. M. De Almeida,[58] P. Debbins,[90] I. De Bonis,[20] M. P. Decowski,[122] A. de Gouvêa,[125] P. C. De Holanda,[29] I. L. De Icaza Astiz,[153] A. Deisting,[85] P. De Jong,[122] A. Delbart,[17] D. Delepine,[64] M. Delgado,[3] A. Dell'Acqua,[18] P. De Lurgio,[4] J. R. T. de Mello Neto,[55] D. M. DeMuth,[162] S. Dennis,[109] C. Densham,[142] G. Deptuch,[56] A. De Roeck,[18] V. De Romeri,[72] J. J. De Vries,[28] R. Dharmapalan,[68] F. Diaz,[137] J. S. Díaz,[88] S. Di Domizio,[75] L. Di Giulio,[18] P. Ding,[56] L. Di Noto,[75] C. Distefano,[152] R. Diurba,[160] M. Diwan,[15] Z. Djurcic,[4] N. Dokania,[151] M. J. Dolinski,[45] L. Domine,[143] D. Douglas,[117] F. Drielsma,[143] D. Duchesneau,[20] K. Duffy,[56] P. Dunne,[85] T. Durkin,[142] H. Duyang,[149] O. Dvornikov,[68] D. A. Dwyer,[108] A. S. Dyshkant,[124] M. Eads,[124] D. Edmunds,[117] J. Eisch,[91] S. Emery,[17] A. Ereditato,[10] C. O. Escobar,[56] L. Escudero Sanchez,[28] J. J. Evans,[114] K. Ewart,[88] A. C. Ezeribe,[146] K. Fahey,[56] A. Falcone,[76] C. Farnese,[131] Y. Farzan,[82] J. Felix,[64] E. Fernandez-Martinez,[113] P. Fernandez Menendez,[72] F. Ferraro,[75] L. Fields,[56] A. Filkins,[168] F. Filthaut,[122] R. S. Fitzpatrick,[116] W. Flanagan,[43] B. Fleming,[170] R. Flight,[140] J. Fowler,[46] W. Fox,[88] J. Franc,[41] K. Francis,[124] D. Franco,[170] J. Freeman,[56] J. Freestone,[114] J. Fried,[15] A. Friedland,[143] S. Fuess,[56] I. Furic,[57] A. P. Furmanski,[160] A. Gago,[137] H. Gallagher,[159] A. Gallego-Ros,[19] N. Gallice,[77, 76] V. Galymov,[81] E. Gamberini,[18] T. Gamble,[146] R. Gandhi,[66] R. Gandrajula,[117] S. Gao,[15] D. Garcia-Gamez,[62] M. Á. García-Peris,[72] S. Gardiner,[56] D. Gastler,[13] G. Ge,[39] B. Gelli,[29] A. Gendotti,[49] S. Gent,[148] Z. Ghorbani-Moghaddam,[75] D. Gibin,[131] I. Gil-Botella,[19] C. Girerd,[81] A. K. Giri,[87] D. Gnani,[108] O. Gogota,[101] M. Gold,[120] S. Gollapinni,[110] K. Gollwitzer,[56] R. A. Gomes,[52] L. V. Gomez Bermeo,[145] L. S. Gomez Fajardo,[145] F. Gonnella,[12] J. A. Gonzalez-Cuevas,[6] M. C. Goodman,[4] O. Goodwin,[114] S. Goswami,[134] C. Gotti,[76] E. Goudzovski,[12] C. Grace,[108] M. Graham,[143] E. Gramellini,[170] R. Gran,[118] E. Granados,[64] A. Grant,[44] C. Grant,[13] D. Gratieri,[58] P. Green,[114] S. Green,[28] L. Greenler,[169] M. Greenwood,[128] J. Greer,[14] W. C. Griffith,[153] M. Groh,[88] J. Grudzinski,[4] K. Grzelak,[165] W. Gu,[15] V. Guarino,[4] R. Guenette,[67] A. Guglielmi,[131] B. Guo,[149] K. K. Guthikonda,[65] R. Gutierrez,[3] P. Guzowski,[114] M. M. Guzzo,[29] S. Gwon,[33] A. Habig,[118] A. Hackenburg,[170] H. Hadavand,[157] R. Haenni,[10] A. Hahn,[56] J. Haigh,[166] J. Haiston,[147] T. Hamernik,[56] P. Hamilton,[85] J. Han,[136] K. Harder,[142] D. A. Harris,[172, 56] J. Hartnell,[153] T. Hasegawa,[96] R. Hatcher,[56] E. Hazen,[13] A. Heavey,[56] K. M. Heeger,[170] K. Hennessy,[109] S. Henry,[140] M. A. Hernandez Morquecho,[64] K. Herner,[56] L. Hertel,[23] A. S. Hesam,[18] J. Hewes,[34] A. Higuera,[69] T. Hill,[83] S. J. Hillier,[12] A. Himmel,[56] J. Hoff,[56] C. Hohl,[9] A. Holin,[161] E. Hoppe,[130] G. A. Horton-Smith,[98] M. Hostert,[47] A. Hourlier,[115] B. Howard,[88] R. Howell,[140] J. Huang,[158] J. Huang,[22] J. Hugon,[111] G. Iles,[85] A. M. Iliescu,[73] R. Illingworth,[56] A. Ioannisian,[171] R. Itay,[143]

A. Izmaylov,[72] E. James,[56] B. Jargowsky,[23] F. Jediny,[41] C. Jesús-Valls,[71] X. Ji,[15] L. Jiang,[164] S. Jiménez,[19] A. Jipa,[16] A. Joglekar,[25] C. Johnson,[38] R. Johnson,[34] B. Jones,[157] S. Jones,[161] C. K. Jung,[151] T. Junk,[56] Y. Jwa,[39] M. Kabirnezhad,[129] A. Kaboth,[142] I. Kadenko,[101] F. Kamiya,[54] G. Karagiorgi,[39] A. Karcher,[108] M. Karolak,[17] Y. Karyotakis,[20] S. Kasai,[100] S. P. Kasetti,[111] L. Kashur,[38] N. Kazaryan,[171] E. Kearns,[13] P. Keener,[132] K.J. Kelly,[56] E. Kemp,[29] W. Ketchum,[56] S. H. Kettell,[15] M. Khabibullin,[80] A. Khotjantsev,[80] A. Khvedelidze,[59] D. Kim,[18] B. King,[56] B. Kirby,[15] M. Kirby,[56] J. Klein,[132] K. Koehler,[169] L. W. Koerner,[69] S. Kohn,[21,108] P. P. Koller,[10] M. Kordosky,[168] T. Kosc,[81] U. Kose,[18] V. A. Kostelecký,[88] K. Kothekar,[14] F. Krennrich,[91] I. Kreslo,[10] Y. Kudenko,[80] V. A. Kudryavtsev,[146] S. Kulagin,[80] J. Kumar,[68] R. Kumar,[139] C. Kuruppu,[149] V. Kus,[41] T. Kutter,[111] A. Lambert,[108] K. Lande,[132] C. E. Lane,[45] K. Lang,[158] T. Langford,[170] P. Lasorak,[153] D. Last,[132] C. Lastoria,[19] A. Laundrie,[169] A. Lawrence,[108] I. Lazanu,[16] R. LaZur,[38] T. Le,[159] J. Learned,[68] P. LeBrun,[81] G. Lehmann Miotto,[18] R. Lehnert,[88] M. A. Leigui de Oliveira,[54] M. Leitner,[108] M. Leyton,[71] L. Li,[23] S. Li,[15] S. W. Li,[143] T. Li,[50] Y. Li,[15] H. Liao,[98] C. S. Lin,[108] S. Lin,[38] A. Lister,[169] B. R. Littlejohn,[84] J. Liu,[23] S. Lockwitz,[56] T. Loew,[108] M. Lokajicek,[40] I. Lomidze,[59] K. Long,[85] K. Loo,[95] D. Lorca,[10] T. Lord,[166] J. M. LoSecco,[126] W. C. Louis,[110] K.B. Luk,[21,108] X. Luo,[26] N. Lurkin,[12] T. Lux,[71] V. P. Luzio,[54] D. MacFarland,[143] A. A. Machado,[29] P. Machado,[56] C. T. Macias,[88] J. R. Macier,[56] A. Maddalena,[61] P. Madigan,[21,108] S. Magill,[4] K. Mahn,[117] A. Maio,[103,106] J. A. Maloney,[42] G. Mandrioli,[73] J. C. Maneira,[103,106] L. Manenti,[161] S. Manly,[140] A. Mann,[159] K. Manolopoulos,[142] M. Manrique Plata,[88] A. Marchionni,[56] W. Marciano,[15] D. Marfatia,[68] C. Mariani,[164] J. Maricic,[68] F. Marinho,[53] A. D. Marino,[37] M. Marshak,[160] C. Marshall,[108] J. Marshall,[166] J. Marteau,[81] J. Martin-Albo,[72] N. Martinez,[138] D.A. Martinez Caicedo,[147] S. Martynenko,[151] K. Mason,[159] A. T. Mastbaum,[141] M. Masud,[72] S. Matsuno,[68] J. Matthews,[111] C. Mauger,[132] N. Mauri,[73] K. Mavrokoridis,[109] R. Mazza,[76] A. Mazzacane,[56] E. Mazzucato,[17] E. McCluskey,[56] N. McConkey,[114] K. S. McFarland,[140] C. McGrew,[151] A. McNab,[114] A. Mefodiev,[80] P. Mehta,[94] P. Melas,[7] M. Mellinato,[76] O. Mena,[72] S. Menary,[172] L. Mendes Santos,[29] H. Mendez,[138] A. Menegolli,[79] G. Meng,[131] M. D. Messier,[88] W. Metcalf,[111] M. Mewes,[88] H. Meyer,[167] T. Miao,[56] G. Michna,[148] T. Miedema,[122] J. Migenda,[146] R. Milincic,[68] W. Miller,[160] J. Mills,[159] C. Milne,[83] O. Mineev,[80] O. G. Miranda,[35] S. Miryala,[15] C. S. Mishra,[56] S. R. Mishra,[149] A. Mislivec,[160] D. Mladenov,[18] I. Mocioiu,[133] K. Moffat,[47] N. Moggi,[73] R. Mohanta,[70] T. A. Mohayai,[56] N. Mokhov,[56] J. Molina,[6] L. Molina Bueno,[49] A. Montanari,[73] C. Montanari,[79] D. Montanari,[56] L. M. Montano Zetina,[35] J. Moon,[115] M. Mooney,[38] A. Moor,[28] D. Moreno,[3] B. Morgan,[166] C. Morris,[69] C. Mossey,[56] E. Motuk,[161] C. A. Moura,[54] J. Mousseau,[116] W. Mu,[56] L. Mualem,[27] J. Mueller,[38] M. Muether,[167] S. Mufson,[88] F. Muheim,[50] A. Muir,[44] M. Mulhearn,[22] H. Muramatsu,[160] S. Murphy,[49] J. Musser,[88] J. Nachtman,[90] S. Nagu,[112] M. Nalbandyan,[171] R. Nandakumar,[142] D. Naples,[136] S. Narita,[92] D. Navas-Nicolás,[19] N. Nayak,[23] M. Nebot-Guinot,[50] L. Necib,[27] K. Negishi,[92] J. K. Nelson,[168] J. Nesbit,[169] M. Nessi,[18] D. Newbold,[142] M. Newcomer,[132] D. Newhart,[56] R. Nichol,[161] E. Niner,[56] K. Nishimura,[68] A. Norman,[56] R. Northrop,[32] P. Novella,[72] J. A. Nowak,[107] M. Oberling,[4] A. Olivares Del Campo,[47] A. Olivier,[140] Y. Onel,[90] Y. Onishchuk,[101] J. Ott,[23] L. Pagani,[22] S. Pakvasa,[68] O. Palamara,[56] S. Palestini,[18] J. M. Paley,[56] M. Pallavicini,[75] C. Palomares,[19] E. Pantic,[22] V. Paolone,[136] V. Papadimitriou,[56] R. Papaleo,[152] A. Papanestis,[142] S. Paramesvaran,[14] S. Parke,[56] Z. Parsa,[15] M. Parvu,[16] S. Pascoli,[47] L. Pasqualini,[73] J. Pasternak,[85] J. Pater,[114] C. Patrick,[161] L. Patrizii,[73] R. B. Patterson,[27] S. J. Patton,[108] T. Patzak,[1] A. Paudel,[98] B. Paulos,[169] L. Paulucci,[54] Z. Pavlovic,[56] G. Pawloski,[160] D. Payne,[109] V. Pec,[146] S. J. M. Peeters,[153] Y. Penichot,[17] E. Pennacchio,[81] A. Penzo,[90] O. L. G. Peres,[29] J. Perry,[50] D. Pershey,[46] G. Pessina,[76] G. Petrillo,[143] C. Petta,[74] R. Petti,[149] F. Piastra,[10] L. Pickering,[117] F. Pietropaolo,[18,131] J. Pillow,[166] R. Plunkett,[56] R. Poling,[160] X. Pons,[18] N. Poonthottathil,[91] S. Pordes,[56] M. Potekhin,[15] R. Potenza,[74] B. V. K. S. Potukuchi,[93] J. Pozimski,[85] M. Pozzato,[73] S. Prakash,[29] T. Prakash,[108] S. Prince,[67] D. Pugnere,[81] K. Qi,[151] X. Qian,[15] J. L. Raaf,[56] R. Raboanary,[2] V. Radeka,[15] J. Rademacker,[14] B. Radics,[49] A. Rafique,[4] E. Raguzin,[15] M. Rai,[166] M. Rajaoalisoa,[34] I. Rakhno,[56] H. T. Rakotondramanana,[2] L. Rakotondravohitra,[2] Y. A. Ramachers,[166] R. Rameika,[56] M. A. Ramirez Delgado,[64] B. Ramson,[56] A. Rappoldi,[79] G. Raselli,[79] P. Ratoff,[107] S. Ravat,[18] H. Razafinime,[2] J.S. Real,[63] B. Rebel,[169,56] D. Redondo,[19] M. Reggiani-Guzzo,[29] T. Rehak,[45] J. Reichenbacher,[147] S. D. Reitzner,[56] A. Renshaw,[69] S. Rescia,[15] F. Resnati,[18] A. Reynolds,[129] G. Riccobene,[152] L. C. J. Rice,[136] K. Rielage,[110] Y. Rigaut,[49] D. Rivera,[132] L. Rochester,[143] M. Roda,[109] P. Rodrigues,[129] M. J. Rodriguez Alonso,[18] J. Rodriguez Rondon,[147] A. J. Roeth,[46] H. Rogers,[38] S. Rosauro-Alcaraz,[113] M. Rossella,[79] J. Rout,[94] S. Roy,[66] A. Rubbia,[49] C. Rubbia,[60] B. Russell,[108] J. Russell,[143] D. Ruterbories,[140] R. Saakyan,[161] S. Sacerdoti,[1] T. Safford,[117] N. Sahu,[87] P. Sala,[77,18] N. Samios,[15] M. C. Sanchez,[91] D. A. Sanders,[119] D. Sankey,[142] S. Santana,[138] M. Santos-Maldonado,[138] N. Saoulidou,[7] P. Sapienza,[152] C. Sarasty,[34] I. Sarcevic,[5] G. Savage,[56] V. Savinov,[136] A. Scaramelli,[79] A. Scarff,[146] A. Scarpelli,[1]

T. Schaffer,[118] H. Schellman,[128,56] P. Schlabach,[56] D. Schmitz,[32] K. Scholberg,[46] A. Schukraft,[56] E. Segreto,[29] J. Sensenig,[132] I. Seong,[23] A. Sergi,[12] F. Sergiampietri,[151] D. Sgalaberna,[18] M. H. Shaevitz,[39] S. Shafaq,[94] M. Shamma,[25] H. R. Sharma,[93] R. Sharma,[15] T. Shaw,[56] C. Shepherd-Themistocleous,[142] S. Shin,[32] D. Shooltz,[117] R. Shrock,[151] L. Simard,[102] N. Simos,[15] J. Sinclair,[10] G. Sinev,[46] J. Singh,[112] J. Singh,[112] R. Sipos,[18] F. W. Sippach,[39] G. Sirri,[73] A. Sitraka,[147] K. Siyeon,[33] D. Smargianaki,[151] A. Smith,[46] A. Smith,[28] E. Smith,[88] P. Smith,[88] J. Smolik,[41] M. Smy,[23] P. Snopok,[84] M. Soares Nunes,[29] H. Sobel,[23] M. Soderberg,[154] C. J. Solano Salinas,[89] S. Söldner-Rembold,[114] N. Solomey,[167] V. Solovov,[104] W. E. Sondheim,[110] M. Sorel,[72] J. Soto-Oton,[19] A. Sousa,[34] K. Soustruznik,[31] F. Spagliardi,[129] M. Spanu,[15] J. Spitz,[116] N. J. Spooner,[146] K. Spurgeon,[154] R. Staley,[12] M. Stancari,[56] L. Stanco,[131] H. M. Steiner,[108] J. Stewart,[15] B. Stillwell,[32] J. Stock,[147] F. Stocker,[18] T. Stokes,[111] M. Strait,[160] T. Strauss,[56] S. Striganov,[56] A. Stuart,[36] D. Summers,[119] A. Surdo,[144] V. Susic,[9] L. Suter,[56] C. M. Sutera,[74] R. Svoboda,[22] B. Szczerbinska,[156] A. Szelc,[114] R. Talaga,[4] H. A. Tanaka,[143] B. Tapia Oregui,[158] A. Tapper,[85] S. Tariq,[56] E. Tatar,[83] R. Tayloe,[88] A. M. Teklu,[151] M. Tenti,[73] K. Terao,[143] C. A. Ternes,[72] F. Terranova,[76] G. Testera,[75] A. Thea,[142] J. L. Thompson,[146] C. Thorn,[15] S. C. Timm,[56] A. Tonazzo,[1] M. Torti,[76] M. Tortola,[72] F. Tortorici,[74] D. Totani,[56] M. Toups,[56] C. Touramanis,[109] J. Trevor,[27] W. H. Trzaska,[95] Y. T. Tsai,[143] Z. Tsamalaidze,[59] K. V. Tsang,[143] N. Tsverava,[59] S. Tufanli,[18] C. Tull,[108] E. Tyley,[146] M. Tzanov,[111] M. A. Uchida,[28] J. Urheim,[88] T. Usher,[143] M. R. Vagins,[99] P. Vahle,[168] G. A. Valdiviesso,[51] E. Valencia,[168] Z. Vallari,[27] J. W. F. Valle,[72] S. Vallecorsa,[18] R. Van Berg,[132] R. G. Van de Water,[110] D. Vanegas Forero,[29] F. Varanini,[131] D. Vargas,[71] G. Varner,[68] J. Vasel,[88] G. Vasseur,[17] K. Vaziri,[56] S. Ventura,[131] A. Verdugo,[19] S. Vergani,[28] M. A. Vermeulen,[122] M. Verzocchi,[56] H. Vieira de Souza,[29] C. Vignoli,[61] C. Vilela,[151] B. Viren,[15] T. Vrba,[41] T. Wachala,[121] A. V. Waldron,[85] M. Wallbank,[34] H. Wang,[24] J. Wang,[22] Y. Wang,[24] Y. Wang,[151] K. Warburton,[91] D. Warner,[38] M. Wascko,[85] D. Waters,[161] A. Watson,[12] P. Weatherly,[45] A. Weber,[142,129] M. Weber,[10] H. Wei,[15] A. Weinstein,[91] D. Wenman,[169] M. Wetstein,[91] M. R. While,[147] A. White,[157] L. H. Whitehead,[28] D. Whittington,[154] M. J. Wilking,[151] C. Wilkinson,[10] Z. Williams,[157] F. Wilson,[142] R. J. Wilson,[38] J. Wolcott,[159] T. Wongjirad,[159] K. Wood,[151] L. Wood,[130] E. Worcester,[15] M. Worcester,[15] C. Wret,[140] W. Wu,[56] W. Wu,[23] Y. Xiao,[23] G. Yang,[151] T. Yang,[56] N. Yershov,[80] K. Yonehara,[56] T. Young,[123] B. Yu,[15] J. Yu,[157] J. Zalesak,[40] L. Zambelli,[20] B. Zamorano,[62] A. Zani,[77] L. Zazueta,[168] G. P. Zeller,[56] J. Zennamo,[56] K. Zeug,[169] C. Zhang,[15] M. Zhao,[15] E. Zhivun,[15] G. Zhu,[127] E. D. Zimmerman,[37] M. Zito,[17] S. Zucchelli,[73] J. Zuklin,[40] V. Zutshi,[124] and R. Zwaska[56]

(The DUNE Collaboration)

[1] *APC - Université de Paris, CNRS/IN2P3, CEA/lrfu, Observatoire de Paris, 10, rue Alice Domon et Léonie Duquet, 75205 Paris Cedex 13, France*
[2] *University of Antananarivo, BP 566, Antananarivo 101, Madagascar*
[3] *Universidad Antonio Nariño, Cra 3 Este No 47A-15, Bogotá, Colombia*
[4] *Argonne National Laboratory, Argonne, IL 60439, USA*
[5] *University of Arizona, 1118 E. Fourth Street Tucson, AZ 85721, USA*
[6] *Universidad Nacional de Asunción, San Lorenzo, Paraguay*
[7] *University of Athens, University Campus, Zografou GR 157 84, Greece*
[8] *Universidad del Atlantico, Carrera 30 Número 8- 49 Puerto Colombia - Atlántico, Colombia*
[9] *University of Basel, Klingelbergstrasse 82, CH-4056 Basel, Switzerland*
[10] *University of Bern, Sidlerstrasse 5, CH-3012 Bern, Switzerland*
[11] *Beykent University, Istanbul*
[12] *University of Birmingham, Edgbaston, Birmingham B15 2TT, United Kingdom*
[13] *Boston University, Boston, MA 02215, USA*
[14] *University of Bristol, H. H. Wills Physics Laboratory, Tyndall Avenue Bristol BS8 1TL, United Kingdom*
[15] *Brookhaven National Laboratory, Upton, NY 11973, USA*
[16] *University of Bucharest, Faculty of Physics, Bucharest, Romania*
[17] *CEA/Saclay, IRFU Institut de Recherche sur les Lois Fondamentales de l'Univers, F-91191 Gif-sur-Yvette CEDEX, France*
[18] *CERN, European Organization for Nuclear Research 1211 Genève 23, Switzerland, CERN*
[19] *CIEMAT, Centro de Investigaciones Energéticas, Medioambientales y Tecnológicas, Av. Complutense, 40, E-28040 Madrid, Spain*
[20] *Laboratoire d'Annecy-le-Vieux de Physique des Particules, CNRS/IN2P3 and Université Savoie Mont Blanc, CNRS/IN2P3 and Université Savoie Mont Blanc, 74941 Annecy-le-Vieux, France*
[21] *University of California Berkeley, Berkeley, CA 94720, USA*
[22] *University of California Davis, Davis, CA 95616, USA*
[23] *University of California Irvine, Irvine, CA 92697, USA*
[24] *University of California Los Angeles, Los Angeles, CA 90095, USA*
[25] *University of California Riverside, 900 University Ave, Riverside CA 92521*
[26] *University of California Santa Barbara, Santa Barbara, California 93106 USA*

[27]California Institute of Technology, Pasadena, CA 91125, USA
[28]University of Cambridge, JJ Thomson Avenue, Cambridge CB3 0HE, United Kingdom
[29]Universidade Estadual de Campinas, Campinas - SP, 13083-970, Brazil
[30]Centro Brasileiro de Pesquisas Físicas, Rio de Janeiro, RJ 22290-180, Brazil
[31]Institute of Particle and Nuclear Physics of the Faculty of Mathematics and Physics of the Charles University in Prague, V Holešovičkách 747/2, 180 00 Praha 8-Libeň, Czech Republic
[32]University of Chicago, Chicago, IL 60637, USA
[33]Chung-Ang University, Dongjak-Gu, Seoul 06974, South Korea
[34]University of Cincinnati, Cincinnati, OH 45221, USA
[35]Centro de Investigacion y de Estudios Avanzados del IPN (Cinvestav), Mexico City
[36]Universidad de Colima, 340 Colonia Villa San Sebastian Colima, Colima, Mexico
[37]University of Colorado Boulder, Boulder, CO 80309, USA
[38]Colorado State University, Fort Collins, CO 80523, USA
[39]Columbia University, New York, NY 10027, USA
[40]Institute of Physics, Czech Academy of Sciences, Na Slovance 2, 182 21 Praha 8, Czech Republic
[41]Czech Technical University in Prague, Břehová 78/7, 115 19 Prague 1, Czech Republic
[42]Dakota State University, Madison, SD 57042, USA
[43]University of Dallas, Irving, TX 75062-4736, USA
[44]Daresbury Laboratory, Daresbury Warrington, Cheshire WA4 4AD, United Kingdom
[45]Drexel University, Philadelphia, PA 19104, USA
[46]Duke University, Durham, NC 27708, USA
[47]Durham University, South Road, Durham DH1 3LE, United Kingdom
[48]Universidad EIA, Via José María Córdoba #km 2 + 200, Envigado, Antioquia
[49]ETH Zurich, Institute for Particle Physics, Zurich, Switzerland
[50]University of Edinburgh, Edinburgh EH8 9YL, United Kingdom
[51]Universidade Federal de Alfenas, Poços de Caldas - MG, 37715-400, Brazil
[52]Universidade Federal de Goias, Goiania, GO 74690-900, Brazil
[53]Universidade Federal de São Carlos, Araras - SP, 13604-900, Brazil
[54]Universidade Federal do ABC, Av. dos Estados 5001, Santo André - SP, 09210-580 Brazil
[55]Universidade Federal do Rio de Janeiro, Rio de Janeiro - RJ, 21941-901, Brazil
[56]Fermi National Accelerator Laboratory, Batavia, IL 60510
[57]University of Florida, PO Box 118440 Gainesville, FL 32611-8440, USA
[58]Fluminense Federal University, Rua Miguel de Frias, 9 Icaraí Niterói - RJ, 24220-900, Brazil
[59]Georgian Technical University, 77 Kostava Str. 0160, Tbilisi, Georgia
[60]Gran Sasso Science Institute, Viale Francesco Crispi 7, L'Aquila, Italy
[61]Laboratori Nazionali del Gran Sasso, I-67010 Assergi, AQ, Italy
[62]University of Granada & CAFPE, Campus Fuentenueva (Edif. Mecenas), 18002 Granada, Spain
[63]University Grenoble Alpes, CNRS, Grenoble INP, LPSC-IN2P3, 38000 Grenoble, France
[64]Universidad de Guanajuato, Gto., C.P. 37000, Mexico
[65]Department of Physics, K L E F, Green Fields, Guntur - 522 502, AP, India
[66]Harish-Chandra Research Institute, Jhunsi, Allahabad 211 019, India
[67]Harvard University, 17 Oxford St. Cambridge, MA 02138, USA
[68]University of Hawaii, Honolulu, HI 96822, USA
[69]University of Houston, Houston, TX 77204, USA
[70]University of Hyderabad, Gachibowli, Hyderabad - 500 046, India
[71]Institut de Fìsica d'Altes Energies, Barcelona i.e. Catalan ersitat Autonoma de Barcelona, Campus UAB, Facultat Ciències Nord, 08193 Bellaterra, Barcelona, Spain
[72]Instituto de Fisica Corpuscular, Catedratico Jose Beltran, 2 E-46980 Paterna (Valencia), Spain
[73]Istituto Nazionale di Fisica Nucleare Bologna, 40127 Bologna BO, Italy
[74]Istituto Nazionale di Fisica Nucleare Sezione di Catania, Via Santa Sofia 64, I-95123 Catania, Italy
[75]Università degli studi di Genova, Istituto Nazionale di Fisica Nucleare Genova, 16126 Genova GE, Italy
[76]Istituto Nazionale di Fisica Nucleare Sezione di Milano Bicocca and University of Milano Bicocca, Piazza della Scienza, 3 - I-20126 Milano, Italy
[77]Istituto Nazionale di Fisica Nucleare Milano, I-20133 Milano, Italy
[78]Istituto Nazionale di Fisica Nucleare - Sezione di Napoli, Complesso Universitario di Monte S. Angelo, I-80126 Napoli, Italy
[79]Università degli studi di Pavia, Istituto Nazionale di Fisica Nucleare Sezione di Pavia, I-27100 Pavia, Italy
[80]Institute for Nuclear Research of the Russian Academy of Sciences , prospekt 60-letiya Oktyabrya 7a, Moscow 117312, Russia
[81]Institut de Physique des 2 Infinis de Lyon, Rue E. Fermi 4 69622 Villeurbanne, France
[82]Institute for Research in Fundamental Sciences , Farmanieh St. Tehran, 19538-33511, Iran
[83]Idaho State University, Department of Physics, Pocatello, ID 83209, USA
[84]Illinois Institute of Technology, Chicago, IL 60616, USA
[85]Imperial College of Science Technology and Medicine, Blackett Laboratory Prince Consort Road, London SW7 2BZ, United Kingdom
[86]Indian Institute of Technology Guwahati, Guwahati, 781 039, India

[87]*Indian Institute of Technology Hyderabad, Hyderabad, 502285, India*
[88]*Indiana University, Bloomington, IN 47405, USA*
[89]*Universidad Nacional de Ingeniería, Av. Tupac Amaru 210, Lima 25, Perú*
[90]*University of Iowa, Department of Physics and Astronomy 203 Van Allen Hall Iowa City, IA 52242, USA*
[91]*Iowa State University, Ames, Iowa 50011, USA*
[92]*Iwate University, Morioka, Iwate 020-8551, Japan*
[93]*University of Jammu, Physics Department, JAMMU-180006, India*
[94]*Jawaharlal Nehru University, School of Physical Sciences, New Delhi 110067, India*
[95]*University of Jyvaskyla, P.O. Box 35, FI-40014, Finland*
[96]*High Energy Accelerator Research Organization (KEK), Ibaraki, 305-0801, Japan*
[97]*Korea Institute of Science and Technology Information, Daejeon, 34141, South Korea*
[98]*Kansas State University, Manhattan, KS 66506, USA*
[99]*Kavli Institute for the Physics and Mathematics of the Universe , Kashiwa, Chiba 277-8583, Japan*
[100]*National Institute of Technology, Kure College, Hiroshima, 737-8506, Japan*
[101]*Kyiv National University, 64, 01601 Kyiv, Ukraine*
[102]*Laboratoire de l'Accélérateur Linéaire , Bâtiment 200, 91440 Orsay, France*
[103]*Laboratório de Instrumentação e Física Experimental de Partículas - LIP, Lisboa, Portugal*
[104]*Laboratório de Instrumentação e Física Experimental de Partículas - LIP, Coimbra, Portugal*
[105]*Instituto Superior Técnico - IST, Universidade de Lisboa, Portugal*
[106]*Faculdade de Ciências - FCUL, Universidade de Lisboa, Portugal*
[107]*Lancaster University, Bailrigg, Lancaster LA1 4YB, United Kingdom*
[108]*Lawrence Berkeley National Laboratory, Berkeley, CA 94720, USA*
[109]*University of Liverpool, L69 7ZE, Liverpool, United Kingdom*
[110]*Los Alamos National Laboratory, Los Alamos, NM 87545, USA*
[111]*Louisiana State University, Baton Rouge, LA 70803, USA*
[112]*University of Lucknow, Lucknow 226007, Uttar Pradesh, India*
[113]*Madrid Autonoma University and IFT UAM/CSIC, Ciudad Universitaria de Cantoblanco 28049 Madrid, Spain*
[114]*University of Manchester, Oxford Road, Manchester M13 9PL, United Kingdom*
[115]*Massachusetts Institute of Technology, Cambridge, MA 02139, USA*
[116]*University of Michigan, Ann Arbor, MI 48109, USA*
[117]*Michigan State University, East Lansing, MI 48824, USA*
[118]*University of Minnesota Duluth, Duluth, MN 55812, USA*
[119]*University of Mississippi, P.O. Box 1848, University, MS 38677 USA*
[120]*University of New Mexico, 1919 Lomas Blvd. N.E. Albuquerque, NM 87131, USA*
[121]*H. Niewodniczański Institute of Nuclear Physics, Polish Academy of Sciences, Cracow, Poland*
[122]*Nikhef National Institute of Subatomic Physics, Science Park, Amsterdam, Netherlands*
[123]*University of North Dakota, 3501 University Ave Grand Forks, ND 58202-8357, USA*
[124]*Northern Illinois University, Department of Physics, DeKalb, Illinois 60115, USA*
[125]*Northwestern University, Evanston, Il 60208, USA*
[126]*University of Notre Dame, Notre Dame, IN 46556, USA*
[127]*Ohio State University, 191 W. Woodruff Ave. Columbus, OH 43210, USA*
[128]*Oregon State University, Corvallis, OR 97331, USA*
[129]*University of Oxford, Oxford, OX1 3RH, United Kingdom*
[130]*Pacific Northwest National Laboratory, Richland, WA 99352, USA*
[131]*Universtà Degli Studi di Padova, Dip. Fisica e Astronomia G. Galilei and INFN Sezione di Padova, I-35131 Padova, Italy*
[132]*University of Pennsylvania, Philadelphia, PA 19104, USA*
[133]*Pennsylvania State University, University Park, PA 16802, USA*
[134]*Physical Research Laboratory, Ahmedabad 380 009, India*
[135]*Università di Pisa, Theor. Division; Largo B. Pontecorvo 3, Ed. B-C, I-56127 Pisa, Italy*
[136]*University of Pittsburgh, Pittsburgh, PA 15260, USA*
[137]*Pontificia Universidad Católica del Perú, Apartado 1761, Lima, Perú*
[138]*University of Puerto Rico, Mayaguez, 00681, USA*
[139]*Punjab Agricultural University, Department of Math. Stat. & Physics, Ludhiana 141004, India*
[140]*University of Rochester, Rochester, NY 14627, USA*
[141]*Rutgers University, Piscataway, NJ, 08854, USA*
[142]*STFC Rutherford Appleton Laboratory, OX11 0QX Harwell Campus, Didcot, United Kingdom*
[143]*SLAC National Acceleratory Laboratory, Menlo Park, CA 94025, USA*
[144]*Università del Salento and Istituto Nazionale Fisica Nucleare, Via Provinciale per Arnesano, 73100 Lecce, Italy*
[145]*Universidad Sergio Arboleda, Cll 74 -14 -14, 11022 Bogotá, Colombia*
[146]*University of Sheffield, Department of Physics and Astronomy, Sheffield S3 7RH, United Kingdom*
[147]*South Dakota School of Mines and Technology, Rapid City, SD 57701, USA*
[148]*South Dakota State University, Brookings, SD 57007, USA*
[149]*University of South Carolina, Columbia, SC 29208, USA*
[150]*Southern Methodist University, Dallas, TX 75275, USA*

[151] *Stony Brook University, SUNY, Stony Brook, New York 11794, USA*
[152] *INFN - Laboratori Nazionali del Sud (LNS), Via S. Sofia 62, 95123 Catania, Italy*
[153] *University of Sussex, Brighton, BN1 9RH, United Kingdom*
[154] *Syracuse University, Syracuse, NY 13244, USA*
[155] *University of Tennessee at Knoxville, TN, 37996, USA*
[156] *Texas A&M University (Corpus Christi), Corpus Christi, TX 78412, USA*
[157] *University of Texas at Arlington, Arlington, TX 76019, USA*
[158] *University of Texas at Austin, Austin, TX 78712, USA*
[159] *Tufts University, Medford, MA 02155, USA*
[160] *University of Minnesota Twin Cities, Minneapolis, MN 55455, USA*
[161] *University College London, London, WC1E 6BT, United Kingdom*
[162] *Valley City State University, Valley City, ND 58072, USA*
[163] *Variable Energy Cyclotron Centre, 1/AF, Bidhannagar Kolkata - 700 064 West Bengal, India*
[164] *Virginia Tech, Blacksburg, VA 24060, USA*
[165] *University of Warsaw, Faculty of Physics ul. Pasteura 5 02-093 Warsaw, Poland*
[166] *University of Warwick, Coventry CV4 7AL, United Kingdom*
[167] *Wichita State University, Physics Division, Wichita, KS 67260, USA*
[168] *William and Mary, Williamsburg, VA 23187, USA*
[169] *University of Wisconsin Madison, Madison, WI 53706, USA*
[170] *Yale University, New Haven, CT 06520, USA*
[171] *Yerevan Institute for Theoretical Physics and Modeling, Halabian Str. 34, Yerevan 0036, Armenia*
[172] *York University, Physics and Astronomy Department, 4700 Keele St. Toronto M3J 1P3, Canada*

Contents

Contents i

List of Figures iii

List of Tables 1

A Roadmap of the DUNE Technical Design Report 1

A The Near Detector Purpose and Conceptual Design 2
A.1 Overview of the DUNE Near Detector . . . 2
A.1.1 Motivation . . . 2
A.1.2 Design . . . 3
A.2 Role of the ND in the DUNE Oscillation Program . . . 6
A.3 Lessons Learned . . . 8
A.3.1 Current Experiments . . . 8
A.3.2 Past Experience . . . 12
A.4 Constraining the Flux in the ND . . . 13
A.4.1 Neutrino-Electron Elastic Scattering . . . 15
A.4.2 The Low-ν Method . . . 16
A.4.3 Coherent Neutrino-Nucleus Scattering . . . 16
A.4.4 Beam ν_e Content . . . 16
A.5 Movable components of the ND and the DUNE-PRISM program . . . 17
A.5.1 Introduction to DUNE-PRISM . . . 17
A.5.2 LArTPC Component in the DUNE ND: ArgonCube . . . 18
A.5.3 Multipurpose Detector . . . 33
A.5.4 The DUNE-PRISM Program . . . 53
A.6 Fixed On-axis Component of the DUNE ND . . . 56
A.6.1 Motivation and Introduction . . . 56
A.6.2 Three-Dimensional Projection Scintillator Tracker Spectrometer . . . 59
A.7 Meeting the Near Detector Requirements . . . 68
A.7.1 Overarching Requirements . . . 69
A.7.2 Event Rate and Flux Measurements . . . 70
A.7.3 Control of Systematic Errors . . . 71

B ND Hall and Construction 75

Glossary 78

References 84

List of Figures

A.1 MINERvA medium energy NuMI flux for low-ν events . . . 10
A.2 Variation of neutrino energy spectrum as a function of off-axis angle . . . 18
A.3 ArgonCube 2×2 demonstrator . . . 19
A.4 Cutaway drawing of an ArgonCube 2×2 demonstrator module . . . 20
A.5 A prototype ArgonCube light readout paddle and a mounted ArCLight paddle . . . 22
A.6 Influence of the LArTPC size on hadron containment . . . 23
A.7 The current ArgonCube dimensions for the DUNE ND . . . 25
A.8 All neutrino events in the nominal 25 t ArgonCube fiducial volume . . . 25
A.9 Events where the visible hadronic system is contained in ArgonCube fiducial volume . . . 26
A.10 Muon acceptance as a function of true neutrino energy and true muon energy . . . 26
A.11 Neutrino acceptance as a function of energy and momentum transfer . . . 27
A.12 Neutrino acceptance in the (q_3, q_0) plane as a function of neutrino energy . . . 29
A.13 A beam spill in the LAr component of the DUNE ND . . . 30
A.14 Temporal distribution of ν vertices within a beam spill in the ND LAr component . . . 31
A.15 FHC flux covariance matrices for nominal 35 t ArgonCube . . . 32
A.16 Rate+shape and shape-only bin-by-bin flux uncertainties . . . 32
A.17 Reconstructed ν energy spectra for CC ν_μ interactions with charged pions . . . 37
A.18 Momentum spectra of protons ejected from ν interactions in Ar . . . 38
A.19 The ALICE TPC . . . 39
A.20 The ALICE MWPC-based ROC with pad plane readout . . . 39
A.21 Pressure vessel preliminary design . . . 40
A.22 MPD ECAL conceptual design . . . 41
A.23 Conceptual layout of the MPD ECAL . . . 41
A.24 Helmholz coil arrangement . . . 42
A.25 Field map of the superconducting magnet along the z axis . . . 43
A.26 Track-reconstructed ν_e CC event in the HPgTPC . . . 46
A.27 Efficiency of track finding in the HPgTPC . . . 47
A.28 Tracking efficiency for protons in the HPgTPC . . . 47
A.29 ALICE and PEP-4 dE/dx-based particle identification as a function of momentum . . . 48
A.30 The TPC stand-alone p_T resolution in ALICE for p–Pb collisions . . . 49
A.31 Momentum and angular resolutions for muons in GArSoft . . . 50
A.32 Machine learning residuals for protons in the MPD . . . 51
A.33 Energy and angular resolutions for photons in the MPD ECAL . . . 52
A.34 Oscillation fits to nominal and fake data sets for DUNE-PRISM fake data study . . . 55
A.35 Reconstructed energy distributions for nominal and fake data sets; on- and off-axis . . . 55

A.36 Linear combinations of off-axis fluxes giving FD oscillated spectra; range of parameters . 57
A.37 The MINOS near detector event spectrum shown in run periods 58
A.38 Rate vs spectral monitoring of ν beam for 1 σ shifts of the horn positions 59
A.39 A few plastic scintillator cubes assembled with WLS fibers. 60
A.40 The SAND detector configuration 61
A.41 Charge and time spectra for a single 3DST cube 62
A.42 Event displays from the 2018 test beam 63
A.43 SAND beam monitoring capability. 64
A.44 Sample antineutrino interaction in the 3DST 66
A.45 Reconstructed neutron energy residual in the 3DST 66
A.46 Time between ν interaction vertex in 3DST and earliest neutron-induced hit 67
A.47 Purity of neutron-induced hit in the (time, lever arm) space for the 3DST 68
A.48 Energy resolution for neutron candidates in the (time, lever arm) space for the 3DST . . 69

B.1 DUNE ND hall from above and side (transverse to beam) 76

List of Tables

A.1 Event rates for flux constraining processes 6
A.2 MPD performance parameters 44
A.3 SAND event rates 64

Appendix A

The Near Detector Purpose and Conceptual Design

A.1 Overview of the DUNE Near Detector

A.1.1 Motivation

A primary aim of the Deep Underground Neutrino Experiment (DUNE) experiment is to measure the oscillation probabilities for muon neutrino and muon antineutrinos to either remain the same flavor or oscillate to electron (anti)neutrinos. Measuring these probabilities as a function of the neutrino energy will allow definitive determination of the neutrino mass ordering, observation of leptonic charge parity (CP) violation for a significant range of δ_{CP} values, and precision measurement of Pontecorvo-Maki-Nakagawa-Sakata (PMNS) parameters.

The role of the near detector (ND) is to serve as the experiment's control. The ND establishes the null hypothesis (i.e., no oscillations) and constrains systematic errors. It measures the initial unoscillated ν_μ and ν_e energy spectra, and that of the corresponding antineutrinos. Of course, neutrino energy is not measured directly. What is seen in the detector is a the convolution of flux, cross section, and detector response to the particles produced in the neutrino interactions, all of which have energy dependence. The neutrino energy is reconstructed from observed quantities. [1]

To first order, a "far/near" ratio (or migration matrix), derived from the simulation, can predict the unoscillated energy spectra at the far detector (FD) based on the ND measurements. The energy spectra at the FD are then sensitive to the oscillation parameters, which can be extracted via a fit. The ND plays a critical role in establishing what the oscillation signal spectrum should look like in the FD because the expectations for the spectra in both the disappearance and appearance

[1] In experimental neutrino physics, it is common practice to refer to the neutrino energy (and spectra) when, in fact, it is the reconstructed neutrino energy (spectra) which is meant, along with all of the flux, cross section, and detector response complexities that implies.

signals are based on the precisely measured spectra for ν_μ and $\overline{\nu}_\mu$ interactions in the ND.

To achieve the precision needed for DUNE, the experiment will have to operate beyond the first-order paradigm. With finite energy resolution and nonzero biases, the reconstructed energy spectrum is an unresolved convolution of cross section, flux, and energy response. The ND must independently constrain each of those components. The ND must provide information that can be used to model well each component. Models of the detector, beam, and interactions fill in holes and biases left by imperfect understanding and they are used to estimate the size of many systematic effects. When imperfect models are not able to match observations, the ND must provide the information needed to deal with that and estimate the impact of the imperfect modeling on final measurements. In general, this requires that the ND significantly outperform the FD, which is limited by the need for a large, underground mass. The ND must have multiple methods for measuring neutrino fluxes as independently of cross section uncertainties as possible. With the necessity of relying on models, the ND needs to measure neutrino interactions with much better detail than the FD. This includes having a larger efficiency across the kinematically allowed phase space of all relevant reaction channels, superior identification of charged and neutral particles, better energy reconstruction, and better controls on experimental biases. The ND must also have the ability to measure events in a similar way to the FD, so that it can determine the ramifications of the more limited FD performance, provide corrections, and take advantage of effects canceling to some extent in the near to far extrapolation.

The conceptual design of the ND is based on the collective experience of the many DUNE collaborators who have had significant roles in the current generation of neutrino experiments (MINOS, MiniBooNE, T2K, NOvA, MINERvA, and the Short-Baseline Neutrino (SBN) program). These programs have provided (and will provide) a wealth of useful data and experience that has led to improved neutrino interaction models, powerful new analyses and reconstruction techniques, a deep appreciation of analysis pitfalls, and a better understanding of the error budget. These experiments, while similar to DUNE, were all done with a lower precision, in a different energy range, or with very different detector technologies. While the existing and projected experience and data from those experiments provide a strong base for DUNE, it is not sufficient to enable DUNE to accomplish its physics goals without a highly performing ND.

The DUNE ND will also have a physics program of its own measuring cross sections, non-standard interactions (NSI), searching for sterile neutrinos, dark photons, and other exotic particles. These are important aims that expand the physics impact of the ND complex. Furthermore, the cross section program is coupled to the oscillation measurement insofar as the cross sections will be useful as input to theory and model development. (Note that many of the ND data samples are incorporated into the oscillation fits directly.)

A.1.2 Design

The DUNE ND is formed from three primary detector components and the capability for two of these components to move off the beam axis. The three detector components serve important individual and overlapping functions with regard to the mission of the ND. Because these components have standalone features, the DUNE ND is often discussed as a suite or complex of detectors and

capabilities. The movement off axis provides a valuable extra degree of freedom in the data which is discussed extensively in this report. The power in the DUNE ND concept lies in the collective set of capabilities. It is not unreasonable to think of the component detectors in the DUNE ND as being somewhat analogous to subsystems in a collider experiment, the difference being that, with one important exception (higher momentum muons), individual events are contained within the subsystems. The DUNE ND is shown in the DUNE ND hall in Figure **??**. Table **??** provides a high-level overview of the three components of the DUNE ND along with the off-axis capability that is sometimes described as a fourth component.

The core part of the DUNE ND is a liquid argon time-projection chamber (LArTPC) called ArgonCube. The particular implementation of the LArTPC technology in this detector is described in Section A.5.2 below. This detector has the same target nucleus and shares some aspects of form and functionality with the FD, while the differences are necessitated by the expected intensity of the beam at the ND. This similarity in target nucleus and, to some extent, technology, reduces sensitivity to nuclear effects and detector-driven systematic errors in the extraction of the oscillation signal at the FD. The LArTPC is large enough to provide high statistics ($1 \times 10^8 \nu_\mu$-CC events/year on axis) and a sufficient volume to provide good hadron containment. The tracking and energy resolution, combined with the mass of the LArTPC, will allow for the measurement of the flux in the beam using several techniques, including the rare process of ν-e$^-$ scattering.

The LArTPC begins to lose acceptance for muons above $\sim$0.7 GeV/c due to lack of containment. Because the muon momentum is a critical component of the neutrino energy determination, a magnetic spectrometer is needed downstream of the LArTPC to measure the charge sign and momentum of these muons. In the DUNE ND concept, this function is accomplished by the multi-purpose detector (MPD), which consists of a high-pressure gaseous argon TPC (HPgTPC) surrounded by an electromagnetic calorimeter (ECAL) in a 0.5 T magnetic field. The HPgTPC provides a lower density medium with excellent tracking resolution for the muons from the LArTPC. In addition, with this choice of technology for the tracker, neutrinos interacting on the argon in the HPgTPC constitute a large (approximately $1 \times 10^6 \nu_\mu$-charged current (CC) events/year on axis) independent sample of ν-Ar events that can be studied with a very low momentum threshold for tracking charged particles, excellent resolution, and with systematic errors that differ from the liquid detector. These events will be valuable for studying the charged particle activity near the interaction vertex, since this detector can access lower-momentum protons than the LArTPC and has better particle identification of charged pions. Misidentification of pions as knock-out protons (or vice versa) causes a mistake in the reconstructed neutrino energy, moving it away from its true value by the amount of a pion mass. This mistake can become quite significant at the lower-energy second oscillation maximum. The gas detector will play an important role in mitigating this mistake, since pions are rarely misidentified as protons in the HPgTPC. In addition, the relatively low level of secondary interactions in the gas samples will be helpful for identifying the particles produced in the primary interaction and modeling secondary interactions in denser detectors, which are known to be important effects[1]. The high pressure increases the statistics for these studies, improves the particle identification capabilities, and improves the momentum resolution. The MPD is discussed further in Section A.5.3.

The LArTPC and MPD can move to take data in positions off the beam axis. This capability is referred to as DUNE Precision Reaction-Independent Spectrum Measurement (DUNE-PRISM). As the detectors move off-axis, the incident neutrino flux spectrum changes, with the mean energy

dropping and the spectrum becoming somewhat monochromatic. Though the neutrino interaction rate drops off-axis, the intensity of the beam and the size of the LArTPC combine to yield ample statistics even in the off-axis positions. Data taken at different off-axis angles allow deconvolution of the neutrino flux and interaction cross section and the mapping of the reconstructed versus true energy response of the detector. This latter mapping is applicable at the FD up to the level to which the near and far liquid argon (LAr) detectors are similar. Stated a different way, it is possible to use information from a linear combination of the different fluxes to create a data sample at the ND with an effective neutrino energy distribution that is close to that of the oscillated spectrum at the FD. This data-driven technique will reduce systematic effects coming from differences in the energy spectra of the oscillated signal events in the FD and the ND samples used to constrain the interaction model. Finally, the off-axis degree of freedom provides a sensitivity to some forms of mismodeling in the beam and/or interaction models. The DUNE-PRISM program is discussed further in Section A.5.4.

The final component of the DUNE ND suite is the beam monitor, called the System for on-Axis Neutrino Detection (SAND). The core part of it, the 3D scintillator tracker (3DST), is a plastic scintillator detector made of $1\,\mathrm{cm}^3$ cubes read out along each of three orthogonal dimensions. The design eliminates the typical planar-strip geometry common to scintillator detectors, leading to improved acceptance at large angles relative to the beam direction. It is mounted inside an envelope of high-resolution, normal pressure time projection chambers (TPCs) and an ECAL, all of which are surrounded by a magnet, as illustrated in Figure A.40. The reference design uses a repurposed magnet and ECAL from the KLOE experiment. The 3DST serves as a dedicated neutrino spectrum monitor that never moves off-axis. It also provides an excellent on-axis, neutrino flux determination using many of the methods discussed in Section A.4. The neutrino flux determined using this detector, with technologies, targets, and interaction systematic errors that are different from ArgonCube, is an important point of comparison and a systematic cross-check for the flux as determined by ArgonCube.

SAND provides very fast timing and can isolate small energy depositions from neutrons in three dimensions. This provides the capability to incorporate neutrons in the event reconstruction using energy determination via time-of-flight with a high efficiency. This capability is expected to be useful for the low-ν flux determination since it allows for tagging of events with a significant neutron energy component[2]. The inclusion of the neutron reconstruction also provides a handle for improving the neutrino energy reconstruction in $\overline{\nu}_\mu$ CCQE events, which is helpful for the $\overline{\nu}_\mu$ flux determination. The different mass number A of the carbon target relative to argon may prove to be useful for developing models of nuclear effects and building confidence in the interaction model and the size of numerous systematic errors. The addition of the neutron reconstruction capability extends the DUNE ND theme of including regions of phase space in neutrino interactions not seen in previous experiments. This capability may provide insights that foster improvements in the neutrino interaction model on carbon. Though extrapolating such improvements to argon is not straightforward, the development of current generators has benefited from data taken with different nuclear targets, including carbon. The SAND component of the ND is discussed more in Section A.6.2.

[2]The low-ν technique involves measuring the flux for events with low energy transfer because the cross section is approximately constant with energy for this sample. It provides a nice way to measure the shape of the spectrum. This is discussed further in Section A.4.

Table A.1 shows the statistics expected in the different ND components for a few processes that are important for constraining the neutrino flux. Some additional information on constraining the flux is provided in Section A.4.

Table A.1: Event rates for processes that can be used to constrain the neutrino flux. The rates are given per year for a 1 ton (fiducial volume (FV)) HPgTPC, a 25 ton (FV) LArTPC [2], and a 9 t (FV) 3DST. The flux for the HPgTPC and LArTPC is from the simulated "2017 engineered" Long-Baseline Neutrino Facility (LBNF) beam with a primary momentum of 120 GeV/c and 1.1×10^{21} POT/year. The flux for the 3DST is the 80 GeV, three-horn, optimized beam with 1.46×10^{21} POT/year. The detectors are assumed to be on-axis. Fiducial volumes are analysis dependent and in the case of the LArTPC, it is likely the volume could be made larger by a factor of two for many analyses.

Event class	LArTPC	HPgTPC	3DST
$\nu_\mu + e^-$ elastic ($E_e > 500$ MeV)	3.3×10^3	1.3×10^2	1.1×10^3
ν_μ low-ν ($\nu < 250$ MeV)	5.3×10^6	2.1×10^5	1.48×10^6
ν_μ CC coherent	2.2×10^5	8.8×10^3	
$\bar{\nu}_\mu$ CC coherent	2.1×10^4	8.4×10^2	

A.2 Role of the ND in the DUNE Oscillation Program

Oscillation experiments need to accomplish three main tasks. First, they must identify the flavor of interacting neutrinos in CC events, or identify the events as neutral current (NC) interactions. Second, they need to measure the energy of the neutrinos since oscillations occur as a function of baseline length over neutrino energy, L/E. Third, they need to compare the observed event spectrum in the FD to predictions based on differing sets of oscillation parameters, subject to constraints from the data observed in the ND. That comparison and how it varies with the oscillation parameters allows for the extraction of the measured oscillation parameters and errors.

The connection between the observations in the ND and the FD is made using a simulation that convolves models of the neutrino flux, neutrino interactions, nuclear effects, and detector response. This gives rise to a host of complicating effects that muddy the simple picture. They come from two main sources. First, the identification efficiency is not 100 % and there is some background (e.g., NC events with a π^0 are a background to ν_e CC interactions). Both the efficiency and the background are imperfectly known. Generally, it is helpful to have a ND that is as similar as feasible to the FD because a bias in the efficiency as a function of energy will cancel between the two detectors. Since the background level tends to be similar between the two detectors, it is helpful if the ND is more capable than the FD at characterizing backgrounds, either due to its technology, or by leveraging the much larger statistics and freedom to take data in alternative beam configuration modes (e.g., different horn currents or movement off the beam axis).

The second major source of complication occurs because the FD (and the similar ND) has to be made of heavy nuclei rather than hydrogen. Neutrino interactions can be idealized as a three stage process: (1) a neutrino impinges on a nucleus with nucleons in some initial state configuration, (2) scattering occurs with one of the nucleons, perhaps creating mesons, and (3) the hadrons reinteract

with the remnant nucleus on their way out (so called final-state interactions (FSI)). The presence of the nucleus impacts all three stages in ways that ultimately drive the design of the ND complex. To better understand this it is useful to consider what would happen if the detectors were made of hydrogen.

In a detector made of hydrogen, the initial state is a proton at rest and there are no FSI. The scattering consists of a variety of processes. The simplest is quasi-elastic (QE) scattering: $\bar{\nu}_\ell p \to \ell^+ n$. The detector sees a lepton (which establishes the flavor of the neutrino), no mesons, and perhaps a neutron interaction away from the lepton's vertex. Because there are no mesons the kinematics is that of two body scattering and the neutrino energy can be reconstructed from the the lepton's angle (with respect to the ν beam) and energy. This is independent of whether the neutron is observed.

For ν_ℓ interactions on hydrogen there is no QE process. The simplest scattering channel is single pion production $\nu_\ell p \to \ell^- \pi^{(+,0)}(n,p)$. In that case the neutrino energy may be reconstructed from the energy of the muon and pion, and their angles with respect to the beam[3]. In both cases, the neutrino energy can be measured without bias so long as the detector itself measures lepton and meson momenta and angles without bias. The neutrino energy in complicated scattering channels, such as ones with multiple pions or heavy baryons can be measured in a similar way (at least in principle).

A key simplifying feature offered by a hypothetical hydrogen detector is simply that there are enough constraints to measure the neutrino energy without needing to measure the single nucleon (especially a neutron escaping the detector). Additionally, the cross sections for different scattering channels (particularly the simpler ones) can be expressed in terms of leptonic and hadronic currents. The leptonic current is well understood. The structural elements of the hadronic current are known on general theoretical grounds. The current is often represented by form factors that are constrained by electron scattering experiments, beta decay, and neutrino scattering measurements that the detector can make itself (or take from other experiments).

The situation is significantly more complicated in a detector with heavy nuclei. The nucleons in the initial state of the nucleus are mutually interacting and exhibit Fermi motion. This motion ruins the key momentum conservation constraint available in hydrogen due to the target being at rest. Scattering at lower momentum transfer is suppressed because the nucleon in the final state would have a momentum that is excluded by the Pauli principle.

The nucleon momentum distribution in heavy nuclei is commonly modeled as a Fermi gas with a cutoff momentum $k_F \approx 250\,\mathrm{MeV/c}$ [3]. This picture is overly simplistic. For example, there are nucleons with momenta larger than k_F due to short-range correlated nucleon-nucleon interactions (SRC)[4]. Scattering on a nucleon with $p > k_F$ implies that there is a spectator nucleon recoiling against the target with a significant momentum. SRC have been the subject of much investigation but are not fully understood or fully implemented in neutrino event generators.

Additionally, there is a second multi-body effect. For the few-GeV neutrinos of interest to DUNE,

[3]The nucleon does not need to be observed. This is a consequence of having four energy-momentum conservation constraints, which allows E_ν and $\vec{p}_N$ to be computed.

the typical momentum transfer corresponds to a probe that has a wavelength on par with the size of a nucleon. In this case, the scattering can occur on two targets in the nucleus which may be closely correlated (2p2h scattering). Experiments can easily confuse this process for QE scattering since there are no mesons and one or both of the two nucleons may have low energy, evading detection. The presence of two nucleons in the initial and final state again ruins the kinematic constraints available in hydrogen. It is now known that 2p2h scattering is a significant part of the total scattering cross section at DUNE energies [5]. The 2p2h cross section is difficult to compute because it cannot be expressed as the sum over cross sections on individual nucleons. The dependence on atomic number and the fine details of the interaction (e.g., the final energies of the two particles) are also currently unknown. Finally, it is widely expected that there are components of 2p2h and SRC scattering that result in meson production. Event generators do not currently include such processes.

Neutrino scattering on nuclei is also subject to FSI. FSI collectively refers to the process by which nucleons and mesons produced by the neutrino interaction traverse the remnant nucleus. The hadrons reinteract with a variety of consequences: additional nucleons can be liberated; "thermal" energy can be imparted to the nucleus; pions can be created and absorbed; and pions and nucleons can undergo charge exchange scattering (e.g., $\pi^- p \to \pi^0 n$). Event generators include phenomenological models for FSI, anchoring to hadron-nucleus scattering data.

The heavy nuclei in a detector also act as targets for the particles that have escaped the struck nucleus. Generally speaking, the denser the detector and the more crudely it samples deposited energy, the more difficult it is to observe low-energy particles. Negatively and positively charged pions leave different signatures in a detector since the former are readily absorbed while the latter are likely to decay. Neutrons can be produced from the struck nucleus, but also from follow-on interactions of the neutrino's reaction products with other nuclei. The energy carried away by neutrons is challenging to detect and can bias the reconstructed neutrino energy.

Finally, it is important to note that a significant fraction of the neutrino interactions in DUNE will come from deep inelastic scattering rather than the simpler QE scattering discussed above. This leads typically to a more complex morphology for events (beyond the heavy nucleus complications) and greater challenges for the detector and the modeling.

A.3 Lessons Learned

A.3.1 Current Experiments

Neutrino beams are notoriously difficult to model at the precision and accuracy required for modern accelerator-based experiments. Recent long-baseline (LBL) experiments make use of a ND placed close to the beam source, where oscillations are not yet a significant effect. The beam model, the neutrino interaction model, and perhaps the detector response model are tuned, or calibrated, by the data recorded in the ND. The tuned model is used in the extraction of the oscillation signal at the FD. Known effects that are not understood or modeled well must be propagated

into the final results as part of the systematic error budget. Unknown effects that manifest as disagreements between the model and observations in the ND also must be propagated into the final results as part of the systematic error budget. These kinds of disagreements have happened historically to every precision accelerator oscillation experiment. When such disagreements arise, some assumption or range of assumptions must be made about the source of the disagreement. Without narrowing down the range of possibilities, this can become a leading systematic error.

Since the final results depend on the comparison of what is seen in the FD to that in the ND, having functionally identical detectors (i.e., the same target nucleus and similar detector response) is helpful. In a similar vein, differences between the neutrino spectrum at the ND and the oscillated spectrum seen at the FD lead to increased sensitivity to systematic effects propagated from the ND to the FD.

The past experience of the neutrino community is a driving force in the design of the DUNE ND complex. The performance of current, state-of-the-art long baseline oscillation experiments provides a practical guide to many of the errors and potential limitations DUNE can expect to encounter, as well as case studies of issues that arose which were unanticipated at the design stage.

The T2K experiment uses an off-axis neutrino beam that has a narrow energy distribution peaked below 1 GeV. This means, relative to DUNE, interactions in T2K are predominantly CCQE and have relatively simple morphologies. The data sample has little feed-down from higher energy interactions. The T2K ND (plastic scintillator and TPC) technology is very different from its FD (water Cerenkov), though the ND contains embedded water targets that provide samples of interactions on the same target used in the FD. The experiment relies on the flux and neutrino interaction models, as well as the ND and FD response models to extrapolate the constraint from the ND to the FD. In the most recent oscillation results released by T2K, the ND data constraint reduces the flux and interaction model uncertainties at the FD from 11—14% down to 2.5—4% [6]. Inclusion of the water target data was responsible for a factor of two reduction in the systematic uncertainties, highlighting the importance of measuring interactions on the same target nucleus as the FD.[4]

The NOvA experiment uses an off-axis neutrino beam from NuMI that has a narrow energy distribution peaked around 2 GeV. The NOvA ND is functionally identical to its FD. Still, it is significantly smaller than the FD and it sees a different neutrino spectrum due to geometry and oscillations. Even with the functionally identical near and far detectors, NOvA uses a model to subtract NC background and relies on a model-dependent response matrix to translate what is seen in the ND to the "true" spectrum, which is then extrapolated to the FD where it is put through a model again to predict what is seen in the FD [7, 8]. Within the extrapolation, the functional similarity of the near and far detectors reduces but does not eliminate many systematic effects. Uncertainties arising from the neutrino cross section model dominate the NOvA ν_e appearance systematic error budget and are among the larger errors in the ν_μ disappearance results. The ND constraint is significant. For the ν_e appearance signal sample in the latest NOvA results, for example, a measure of the systematic error arising from cross section uncertainties without using the ND extrapolation is 12 % and this drops to 5 % if the ND extrapolation is used [8].

[4] These numbers are not used directly in the analysis but were extracted to provide an indication of the power of the ND constraint.

The process of implementing the ND constraint in both T2K and NOvA is less straightforward than the typical description implies. It will not be any more straightforward for DUNE. One issue is that there are unavoidable near and far differences. Even in the case of functionally identical detectors, the beam spectrum and intensity are very different near to far. For DUNE, in particular, ArgonCube is smaller than the FD and is divided into modular, optically isolated regions that have a pixelated readout rather than the wire readout of the FD. Space charge effects will differ near to far. All of this imposes model dependence on the extrapolation from near to far. This is mitigated by collecting data at differing off-axis angles with DUNE-PRISM, where an analysis can be done with an ND flux that is similar to the oscillated FD flux (see Section A.5.4). (Data from ProtoDUNE will also be useful to understand the energy-dependent detector response for the FD.) Regardless, near to far differences will persist and must be accounted for through the beam, detector, and neutrino interaction models.

Although long baseline oscillation experiments use the correlation of fluxes at the ND and the FD to reduce sensitivity to flux modeling, the beam model is a critical component in understanding this correlation. Recently, the MINERvA experiment used spectral information in the data to diagnose a discrepancy between the expected and observed neutrino event energy distribution in the NuMI medium energy beam [9]. In investigating this issue, MINERvA compared the observed and simulated neutrino event energy distribution for low-ν events, as shown in Figure A.1. Since the cross section is known to be relatively flat as a function of neutrino energy for this sample, the observed disagreement as a function of energy indicated a clear problem in the flux model or reconstruction. MINERvA believes the observed discrepancy between the data and simulation is best described by what is a mismodeling in horn focusing combined with an error in the muon energy reconstruction (using range traversed in the downstream spectrometer). This is notable, in part, because the two identified culprits in this saga would manifest differently in the extrapolation to the far detector in an oscillation experiment. The spectral analysis provided critical information in arriving at the final conclusion. This experience illustrates the importance of good monitoring/measurements of the neutrino beam spectrum.

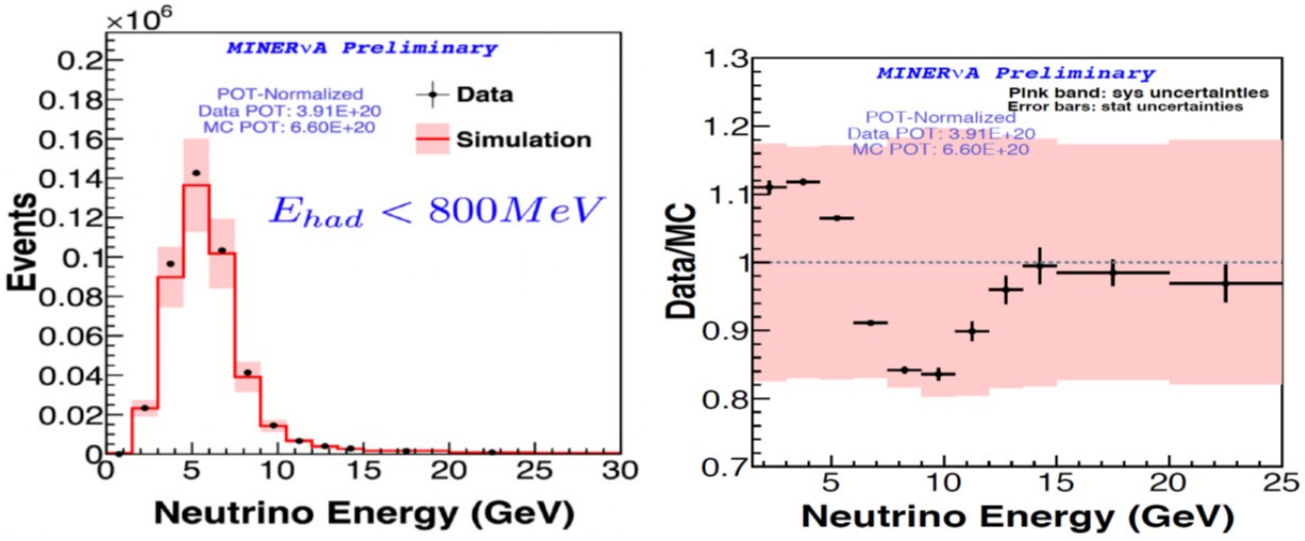


Figure A.1: Reconstructed MINERvA medium energy NuMI neutrino event spectrum for low-energy transfer events compared to simulation (left) and same comparison shown as a ratio (right). From [9].

Another important issue is that the neutrino interaction model is not perfect, regardless of the

experiment and implementation. With an underlying model that does not describe reality, even a model tuned to ND data will have residual disagreements with that data. These disagreements must be accounted for in the systematic error budget of the ultimate oscillation measurements. Although the model(s) may improve before DUNE operation, the degree of that improvement cannot be predicted and the DUNE ND complex should have the capability to gather as much information as possible to help improve and tune the model(s) during the lifetime of the experiment. In other words, the ND needs to be capable of narrowing the range of plausible possibilities giving rise to data-model differences at the ND in order to limit the systematic error incurred in the results extracted from the FD.

Recent history provides illustrations of progress and continuing struggles to improve neutrino interaction models. The MiniBooNE collaboration published results in 2010 showing a disagreement between the data and the expected distribution of CCQE events as a function of Q^2 [10, 11]. They brought the model into agreement with the data by increasing the axial mass form factor used in the model. K2K [11] and MINOS [12] made similar measurements. It has since been shown that the observed disagreement is due to the need to include multi-nucleon processes and that the use of the large effective axial mass form factor used by these experiments to fit the data leads to a misreconstruction of the neutrino energy.

The importance of modeling multi-nucleon (2p2h) processes for oscillation experiments is underscored by the fact that such interactions when reconstructed as a CCQE (1p1h) process lead to a significant low-side tail in the reconstructed neutrino energy [13]. Multi-nucleon processes also change the hadronic calorimetric response. The first NOvA ν_μ disappearance oscillation results had a dominant systematic error driven by the disagreement of their model to the data in their hadronic energy distribution [14]. In more recent work, the inclusion of multi-nucleon processes in the interaction model contributed to a substantial reduction of this disagreement [7].

The MINERvA experiment has compiled a significant catalog of neutrino and antineutrino results and recently developed a model tuned to their QE-like (NuMI low energy) data [5]. The tune is based on a modern neutrino interaction generator (Generates Events for Neutrino Interaction Experiments (GENIE) 2.8.4 [15], using a global Fermi gas model [3] with a Bodek-Ritchie tail [16] and the INTRANUKE-hA FSI model [17]). Even so, MINERvA scales down non-resonance pion production [18], includes a random phase approximation model (RPA) [19, 20], and incorporates a multi-nucleon model [21, 22, 23] with an empirical enhancement in the dip region between the QE and Δ region that is determined by a fit to the neutrino data [5]. The same tune as developed on the neutrino data also fits well the MINERvA antineutrino QE-like data (with no additional tuning or ingredient). The required enhancement of the multi-nucleon contribution to the model implies shortcomings in the interaction model, but the decent fit to data for both neutrinos and antineutrinos implies that the tune is effectively making up for some imperfections in the model.

More recent versions of GENIE include some of the modifications incorporated by MINERvA in the tune discussed above [24]. This illustrates the dynamic nature of neutrino interaction modeling and the interplay between the experiments and generator developers. The evolution of the field continues as illustrated with a snapshot of some of the current questions and areas of focus:

- There is a pronounced deficit of pions produced at low Q^2 in CC1π° events as compared to

expectations [25, 26, 27, 28, 29]. Current models take this into account by tuning to data without any underlying physical explanation for how or why this happens.

- The MINERvA tune that fits both neutrino and antineutrino CCQE data involves a significant enhancement and distortion of the 2p2h contribution to the cross section. The real physical origin of this cross section strength is unknown. Models of multi-nucleon processes disagree significantly in predicted rates.
- Multi-nucleon processes likely contribute to resonance production. This is neither modeled nor well constrained.
- Cross section measurements used for comparison to models are a convolution of what the models view as initial state, hard scattering, and final state physics. Measurements able to deconvolve these contributions are expected to be very useful for model refinements.
- Most neutrino generators make assumptions about the form of form factors and factorize nuclear effects in neutrino interactions into initial and final state effects via the impulse approximation. These are likely oversimplifications. The models will evolve and the systematic errors will need to be evaluated in light of that evolution.
- Neutrino detectors are largely blind to neutrons and low-momentum protons and pions (though some π^+ are visible via Michel decay). This leads to smearing in the reconstructed energy and transverse momentum, as well as a reduced ability to accurately identify specific interaction morphologies. The closure of these holes in the reconstructed particle phase space is expected to provide improved handles for model refinement.
- There may be small but significant differences in the ν_μ and ν_e CCQE cross sections which are poorly constrained [30].

Given the critical importance of neutrino interaction models and the likelihood that the process of refining these models will continue through the lifetime of DUNE, it is important the DUNE ND suite be highly capable.

A.3.2 Past Experience

The philosophy driving the DUNE ND concept is to provide sufficient redundancy to address areas of known weaknesses in previous experiments and known issues in the interaction modeling insofar as possible, while providing a powerful suite of measurements that is likely to be sensitive to unanticipated issues and useful for continued model improvements. Anything less reduces DUNE's potential to achieve significantly improved systematic errors over previous experiments in the LBL analyses.

The DUNE ND incorporates many elements in response to lessons learned from previous experiments. The massive ND LArTPC has the same target nucleus and a similar technology to the FD. These characteristics reduce the detector and target systematic sensitivity in the extrapolation of flux constraints from this detector to the FD. This detector is capable of providing the primary sample of CC ν_μ interactions to constrain the flux at the FD, along with other important measurements of the flux from processes like ν-e$^-$ scattering and low-ν. Samples taken with this detector at off-axis angles (DUNE-PRISM) will allow the deconvolution of the flux and cross section errors

and provide potential sensitivity to mismodeling. The off-axis data can, in addition, be used to map out the detector response function and construct effective ND samples that mimic the energy distribution of the oscillated sample at the FD.

The DUNE ND provides access to particles produced in neutrino interactions that have been largely invisible in previous experiments, such as low-momentum protons and charged pions measured in the HPgTPC and neutrons in the 3DST and ECAL. The HPgTPC provides data on interactions that minimize the effect of secondary interactions on the produced particles. These capabilities improve the experiment's ability to identify specific interaction morphologies, study samples with improved energy resolution, and extract samples potentially useful for improved tuning of model(s) of multi-nucleon processes. The neutron content in neutrino and antineutrino interactions is different and this will lead to differences in the detector response. For an experiment that is measuring charge-parity symmetry violation (CPV), data on neutron production in neutrino interactions is likely to be an important handle in the tuning of the interaction model and the flavor-dependent detector response function model.

The 3DST provides dedicated beam spectrum monitoring on axis, as well as high statistics samples useful for the on-axis flux determination as a crosscheck on the primary flux determination (which has different detector and target systematic errors). The beam spectrum monitoring is useful for identifying and diagnosing unexpected changes in the beam. This proved useful for NuMI and is likely to be more important for DUNE given the need to associate data taken at different times and off-axis angles.

The large data sets that will be accumulated by the three main detectors in the ND suite will allow for differential studies and the use of transverse kinematic imbalance variables, where each detector brings its unique strengths to the study: the LArTPC has good tracking resolution and containment and massive statistics; the HPgTPC has excellent tracking resolution, very low charged particle tracking thresholds, and unambiguous track charge sign determination; and the 3DST has good containment and can include neutrons on an event-by-event basis. The neutrino interaction samples acquired by this array of detectors will constitute a powerful laboratory for deconvoluting the initial state, hard scattering, and final state physics, which, in turn, will lead to improved modeling and confidence in the final results extracted from the FD.

A.4 Constraining the Flux in the ND

The DUNE FD will not measure the neutrino oscillation probability directly. Instead, it will measure the neutrino interaction rate for different neutrino flavors as a function of the reconstructed neutrino energy. It is useful to formalize the measurements that are performed in the near and far detector modules in the following equations:

$$\frac{dN_x^{FD}}{dE_{rec}}(E_{rec}) = \int \Phi_{\nu_\mu}^{FD}(E_\nu) P_{\nu_\mu \to x}(E_\nu) \sigma_x^{Ar}(E_\nu) T_x^{FD,Ar}(E_\nu, E_{rec}) dE_\nu \quad \text{(A.1)}$$

$$\frac{dN_x^{ND}}{dE_{rec}}(E_{rec}) = \int \Phi_x^{ND}(E_\nu) \sigma_x^{m}(E_\nu) T_x^{d,m}(E_\nu, E_{rec}) dE_\nu \quad \text{(A.2)}$$

with

- $x = \nu_e$, ν_μ
- d = detector index(ND,FD)
- m = interaction target/material, (e.g., H, C, or Ar)
- E_ν = true neutrino energy
- E_{rec} = reconstructed neutrino energy
- $T_x^{d,m}(E_\nu, E_{rec})$ = true-to-reconstruction transfer function
- $\sigma_x^m(E_\nu)$ = neutrino interaction cross section
- $\Phi_x^d(E_\mu)$ = un-oscillated neutrino flux
- $\frac{dN_x^d}{dE_{rec}}(E_{rec})$ = measured differential event rate per target (nucleus/electron)

There are equivalent formulae for antineutrinos. For simplicity, the instrumental backgrounds (wrongly selected events) and the intrinsic beam contaminations (ν_e interactions in case of the appearance measurement) have been ignored. But an important function of the ND is also to quantify and characterize those backgrounds.

It is not possible to constrain the FD neutrino flux directly, but the near-to-far flux ratio is believed to be tightly constrained by existing hadron production data and the beamline optics. As such Equation A.1 can be rewritten as

$$\frac{dN_x^{FD}}{dE_{rec}}(E_{rec}) = \int \Phi_{\nu_\mu}^{ND}(E_\nu) R(E_\nu) P_{\nu_\mu \to x}(E_\nu) \sigma_x^{Ar}(E_\nu) T_x^{d,Ar}(E_\nu, E_{rec}) dE_\nu \quad \text{(A.3)}$$

$$\text{(A.4)}$$

with

$$R(E_\nu) = \frac{\Phi_{\nu_\mu}^{FD}(E_\nu)}{\Phi_{\nu_\mu}^{ND}(E_\nu)} \quad \text{(A.5)}$$

taken from the beam simulation. It is not possible to measure only a near-to-far event ratio and extract the oscillation probability since many effects do not cancel trivially. This is due to the non-diagonal true-to-reconstruction matrix, which not only depends on the underlying differential cross section, but also on the detector used to measure a specific reaction.

$$\frac{dN_x^{FD}}{dE_{rec}}(E_{rec}) / \frac{dN_{\nu_\mu}^{ND}}{dE_{rec}}(E_{rec}) \neq R(E_\nu) P_{\nu_\mu \to x}(E_\nu) \frac{\sigma_x^{Ar}(E_\nu)}{\sigma_{\nu_\mu}^{m}(E_\nu)} \quad \text{(A.6)}$$

It is therefore important that the DUNE ND suite constrain as many components as possible.

While the near-to-far flux ratio is tightly constrained to the level of 1 % to 2 %, the same is not true for the absolute flux itself. T2K, using hadron production data obtained from a replica target, can constrain the absolute flux at the ND to 5 % to 6 % in the peak region and to around 10% in most of its energy range. The NuMI beam has been constrained to 8% using a suite of thin target hadron production data. The better the ND flux is known, the easier it is to constrain modeling uncertainties by measuring flux-integrated cross sections. Predicting the event rate at the FD to a few percent will require additional constraints to be placed with the ND or substantial improvements in our understanding of the hadron production and focusing uncertainties.

Several handles to constrain the flux are addressed below. Briefly they offer the following constraints:

- The overall flux normalization and spectrum can be constrained by measuring neutrino scattering off of atomic electrons.
- The energy dependence ("shape") of the ν_μ and $\bar{\nu}_\mu$ flux can be constrained using the "low-ν" scattering process.
- The flux ratio $\bar{\nu}_\mu/\nu_\mu$ can be constrained using CC coherent neutrino scattering.
- The ν_e/ν_μ flux ratio in the energy region where standard oscillations occur is well-constrained by the beam simulation. The experiment can also measure the ν_e/ν_μ interaction ratio and constrain the flux ratio using cross section universality.

A.4.1 Neutrino-Electron Elastic Scattering

Neutrino-electron scattering ($\nu\, e \to \nu\, e$) is a pure electroweak process with calculable cross section at tree level. The final state consists of a single electron, subject to the kinematic constraint

$$1 - \cos\theta = \frac{m_e(1-y)}{E_e}, \tag{A.7}$$

where θ is the angle between the electron and incoming neutrino, E_e and m_e are the electron mass and total energy, respectively, and $y = T_e/E_\nu$ is the fraction of the neutrino energy transferred to the electron. For DUNE energies, $E_e \gg m_e$, and the angle θ is very small, such that $E_e\theta^2 < 2m_e$.

The overall flux normalization can be determined by counting $\nu\, e \to \nu\, e$ events. Events can be identified by searching for a single electromagnetic shower with no other visible particles. Backgrounds from ν_e CC scattering can be rejected by looking for large energy deposits near the interaction vertex, which are evidence of nuclear breakup. Photon-induced showers from NC π^0 events can be distinguished from electrons by the energy profile at the start of the track. The dominant background is expected to be ν_e CC scattering at very low Q^2, where final-state hadrons are below threshold, and $E_e\theta^2$ happens to be small. The background rate can be constrained with a control sample at higher $E_e\theta^2$, but the shape extrapolation to $E_e\theta^2 \to 0$ is uncertain at the 10 % to 20 %

level.

For the DUNE flux, approximately 100 events per year per ton of fiducial mass are expected with electron energy above 0.5 GeV. For a LArTPC mass of 25 tons, this corresponds to 3300 events per year. The statistical uncertainty on the flux normalization from this technique is expected to be ∼1%. MINERvA has achieved a systematic uncertainty just under 2% and it seems plausible that DUNE could do at least as well[31]. The 3DST can also do this measurement with significant statistics and with detector and reconstruction systematics largely uncorrelated with ArgonCube. The signal is independent of the atomic number A and the background is small; so, it seems plausible the samples can be combined to good effect.

A.4.2 The Low-ν Method

The inclusive cross section for CC scattering ($\nu_l + N \rightarrow l^- + X$) does not depend on the neutrino energy in the limit where the energy transferred to the nucleus $\nu = E_\nu - E_l$ is zero [32]. In that limit, the event rate is proportional to the flux, and by measuring the rate as a function of energy, one can get the flux "shape." This measurement has been used in previous experiments and has the potential to provide a constraint in DUNE with a statistical uncertainty $< 1\%$.

In practice, one cannot measure the rate at $\nu = 0$. Instead it is necessary to restrict ν to be less than a few 100 MeV. This introduces a relatively small E_ν dependence into the cross section that must be accounted for to obtain the flux shape. Thus the measurement technique depends on the cross section model but the uncertainty is manageable [33]. This is particularly true if low-energy protons and neutrons produced in the neutrino interaction can be detected.

A.4.3 Coherent Neutrino-Nucleus Scattering

The interactions $\nu_\ell + A \rightarrow \ell^- + \pi^+ + A$ and $\overline{\nu}_\ell + N \rightarrow \ell^+ + \pi^- + N$ occur with very low three momentum transfer to the target nucleus (A). As such, the interactions proceed coherently with the entire nucleus, and do not suffer from nuclear effects (though background channels certainly do). These coherent interactions are most useful as a constraint on the $\bar{\nu}_\mu/\nu_\mu$ flux ratio. Identifying with high efficiency and purity requires a detector with excellent momentum and angular resolution.

A.4.4 Beam ν_e Content

Electron neutrinos in a wide-band beam come from two primary sources: kaon decays and muon decays. These "beam" ν_e are an irreducible background in $\nu_\mu \rightarrow \nu_e$ oscillation searches. As such, the LBNF beam was optimized to make the ν_e flux as small as possible while maximizing the ν_μ flux. In the energy range relevant for oscillations (0.5 GeV - 4.0 GeV) the predicted ν_e/ν_μ ratio varies between 0.5% and 1.2% as a function of energy. The beam ν_e flux in the same energy range is strongly correlated with the ν_μ flux due to the decay chain $\pi^+ \rightarrow \mu^+\nu_\mu$ followed by $\mu^+ \rightarrow \bar{\nu}_\mu e^+\nu_e$

(and likewise for $\bar{\nu}_e$). As a result, the LBNF beam simulation predicts that the uncertainty on the ν_e/ν_μ ratio varies from 2.0 % to 4.5 %. At the FD, in a 3.5 year run, the statistical uncertainty on the beam ν_e component is expected to be 7% for the ν mode beam and 10% for the $\bar{\nu}$ mode beam. The systematic uncertainty on the beam ν_e flux is therefore subdominant, but not negligible.

A.5 Movable components of the ND and the DUNE-PRISM program

A.5.1 Introduction to DUNE-PRISM

One of the primary challenges for DUNE will be controlling systematic uncertainties from the modeling of neutrino-argon interactions. The relationship between the observable final state particles from a neutrino interaction and the incident neutrino energy is currently not understood with sufficient precision to achieve DUNE physics goals. This is due in part to mismodeling of the outgoing particle composition and kinematics and due to missing energy from undetected particles, such a neutrons and low energy charged pions, and misidentified particles. The latter effects tend to cause a “feed-down" in reconstructed neutrino energy relative to the true energy. Since neutrino energy spectra at the FD and ND have substantially different features due to the presence of oscillations at the FD, these mismodeling and neutrino energy feed-down effects do not cancel in a far-to-near ratio as a function of neutrino energy, and lead to biases in the measured oscillation parameters.

Understanding ND constraints on neutrino-nucleus interaction uncertainties is challenging, since no complete model of neutrino-argon interactions is available. If it were possible to construct a model that was known to be correct, even with a large number of unknown parameters, then the task of a ND would much simpler: to build a detector that can constrain the unknown parameters of the model. However, in the absence of such a model, this procedure will be subject to unknown biases due to the interaction model itself, which are difficult to quantify or constrain.

The DUNE-PRISM ND program consists of a mobile ND that can perform measurements over a range of angles off-axis from the neutrino beam direction in order to sample many different neutrino energy distributions, as shown in Figure A.2. By measuring the neutrino-interaction final state observables over these continuously varying incident neutrino energy spectra, it is possible to experimentally determine the relationship between neutrino energy and what is measured in the detector (i.e., some observable such as reconstructed energy).

In the DUNE ND, the movable components of the detector that are used in the DUNE-PRISM program are ArgonCube and the MPD. These components of the ND will take data both on the beam axis and off-axis. In the following sections, ArgonCube and the MPD will be described in some detail and then the DUNE-PRISM program will be described in more detail.

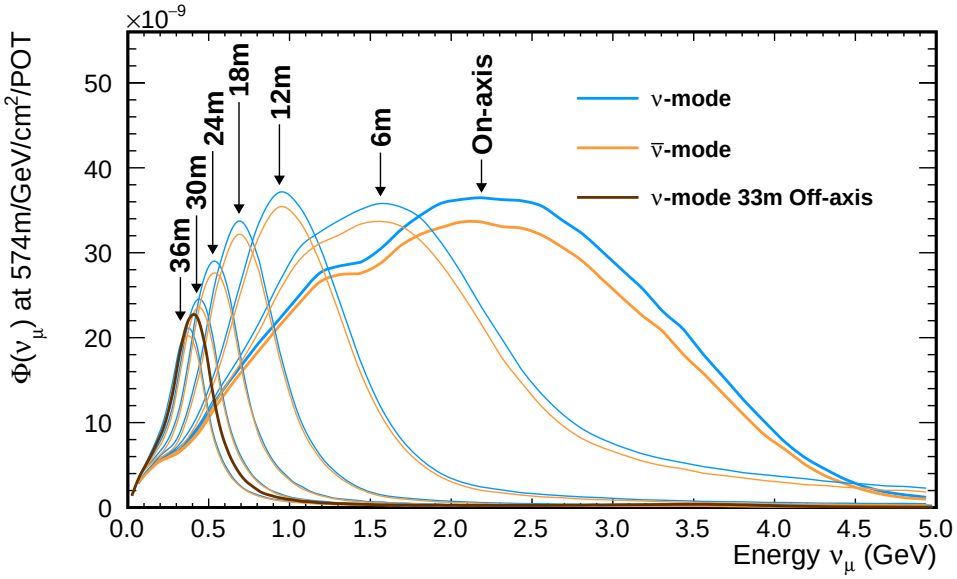


Figure A.2: The variation in the neutrino energy spectrum is shown as a function of detector off-axis position, assuming the nominal ND location 574 m downstream from the production target.

A.5.2 LArTPC Component in the DUNE ND: ArgonCube

As the DUNE FDs have LAr targets, there needs to be a major LAr component in the DUNE ND complex in order to reduce cross section and detector systematic uncertainties for oscillation analyses [34, 35]. However, the intense neutrino flux and high event rate at the ND makes traditional, monolithic, projective wire readout TPCs unsuitable. This has motivated a program of R&D into a new LArTPC design, suitable for such a high-rate environment, known as ArgonCube [36]. ArgonCube utilizes detector modularization to improve drift field stability, reducing high voltage (HV) and the LAr purity requirements; pixelized charge readout [37, 38], which provides unambiguous 3D imaging of particle interactions, drastically simplifying the reconstruction; and new dielectric light detection techniques with ArCLight [39], which can be placed inside the field cage (FC) to increase light yield, and improve the localization of light signals. Additionally, ArgonCube uses a resistive field shell, instead of traditional field shaping rings, to maximize the active volume, and to minimize the power release in the event of a breakdown [40].

The program of ArgonCube R&D has been very successful to date, working on small component prototypes and is summarized in references [41, 42, 43, 37, 44, 38, 40, 39]. With the various technological developments demonstrated with small-scale TPCs, the next step in the ArgonCube program is to demonstrate the scalability of the pixelized charge readout and light detection systems, and to show that information from separate modules can be combined to produce high-quality event reconstruction for particle interactions. To that end, a mid-scale (1.4 m × 1.4 m × 1.2 m) modular TPC, dubbed the ArgonCube 2×2 demonstrator, with four independent LArTPC modules arranged in a 2×2 grid has been designed, and is currently under construction.

After a period of testing at the University of Bern, the ArgonCube 2×2 demonstrator will be placed in the MINOS ND hall at Fermi National Accelerator Laboratory (Fermilab) where it will form the core of a prototype DUNE ND, ProtoDUNE-ND [45]. As part of ProtoDUNE ND, the ArgonCube

concept can be studied and operated in an intense, few-GeV neutrino beam. This program aims to demonstrate stable operation and the ability to handle backgrounds, relate energy associated with a single event across ArgonCube modules, and connect tracks to detector elements outside of ArgonCube. The ArgonCube 2×2 demonstrator is described below in some detail since the DUNE ND modules are anticipated to be very similar.

A.5.2.1 ArgonCube in ProtoDUNE-ND

The ArgonCube concept is a detector made of self-contained TPC modules sharing a common cryostat. Each module is made of a rectangular box with a square footprint and a height optimized to meet the physics goals and/or sensitivity constraints. The ArgonCube 2×2 demonstrator module will be housed within an existing LN_2-cooled and vacuum-insulated cryostat, which is ∼2.2 m in diameter and ∼2.8 m deep, for a total volume of ∼10.6 m^3. The size of the cryostat sets the dimensions of the modules for the demonstrator. The square base of each module will be 0.67 m × 0.67 m, and the height will be 1.81 m. This makes the modules comparable in size to, but slightly smaller than, the proposed ArgonCube DUNE ND modules, which will have a base of 1 m × 1 m and a 3.5 m height.

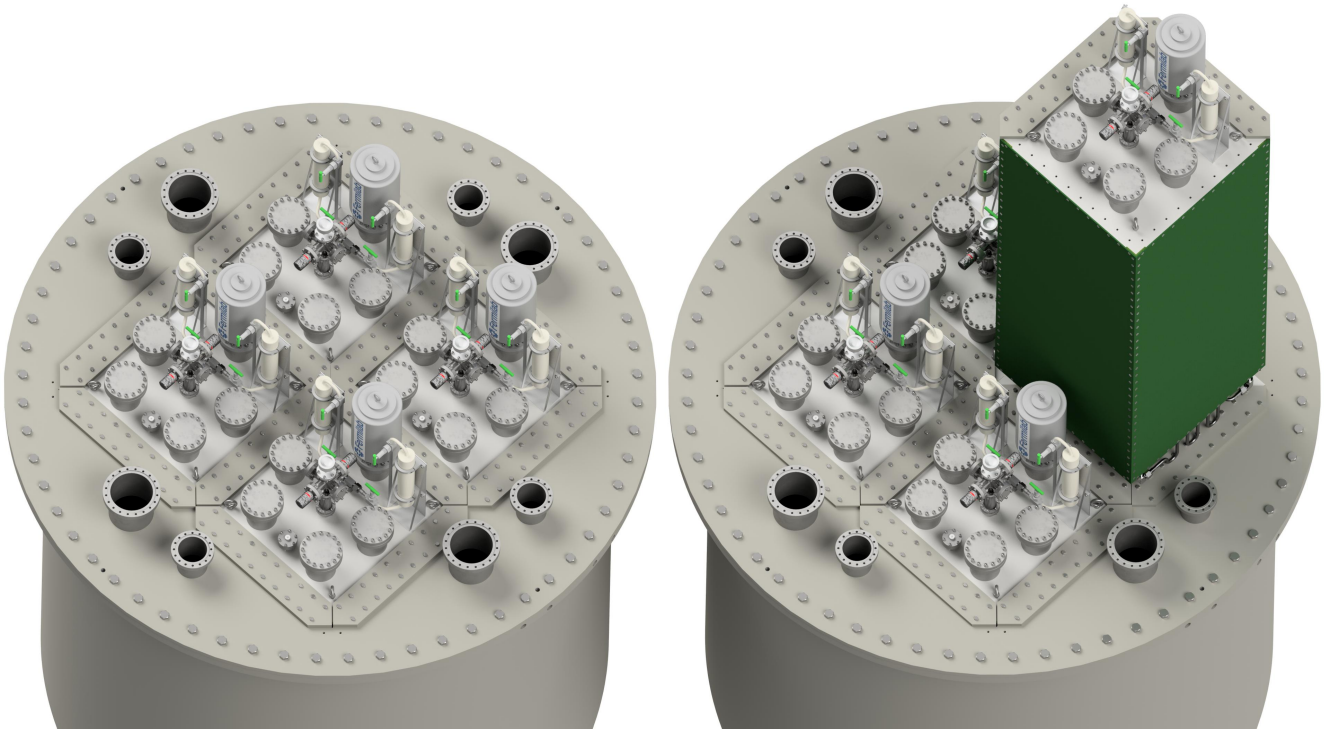


Figure A.3: Illustration of the ArgonCube 2×2 demonstrator module. The four modules are visible, with one of them partly extracted, on the right. This figure has been reproduced from Ref. [36].

Individual modules can be extracted or reinserted into a common LAr bath as needed, as is illustrated in Figure A.3. This feature will be demonstrated during a commissioning run at the University of Bern, but is not intended to be part of the detector engineering studies in the

MINOS-ND hall. The pressure inside the modules is kept close to the bath pressure, putting almost no hydrostatic force on the module walls. This allows the walls to be thin, minimizing the quantity of inactive material in the walls. The purity of the LAr is maintained within the modules, independent of the bath, as will be described below. The argon surrounding the modules need not meet as stringent purity requirements as the argon inside. Under normal operating conditions, all modules are inserted with clearance distances of only 1.5 mm between modules. Cooling power to the bath is supplied by liquid nitrogen circulated through lines on the outer surface of the inner cryostat vessel.

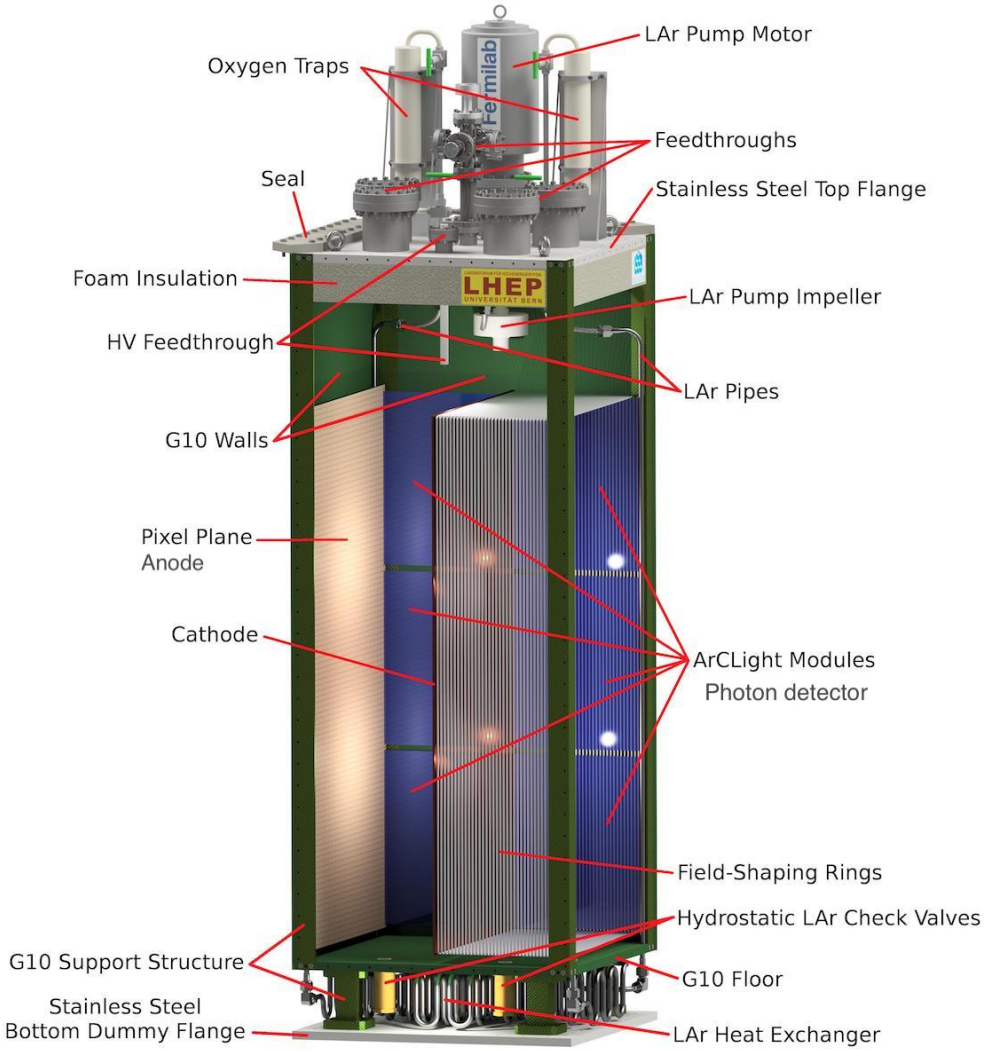


Figure A.4: Cutaway drawing of a 0.67 m × 0.67 m × 1.81 m ArgonCube module for the 2×2 demonstrator module. For illustrative purposes the drawing shows traditional field-shaping rings instead of a resistive field shell. The G10 walls will completely seal the module, isolating it from the neighboring modules and the outer LAr bath. The 2×2 modules will not have individual pumps and filters.

A cutaway drawing of an individual 2×2 module is shown in Figure A.4. The side walls of each module are made from 1 cm G10 sheets, to which the resistive field shell is laminated. The G10 radiation length ($X_0 = 19.4\,\text{cm}$) and hadronic interaction length ($\lambda_{\text{int}} = 53.1\,\text{cm}$) [46] are both comparable to LAr (14.0 cm and 83.7 cm respectively). G10 provides a strong dielectric, capable of $200\,\text{kV} \cdot \text{cm}^{-1}$ when 1 cm thick [47]. This dielectric shielding eliminates the need for a clearance

volume between the TPCs and the cryostat, while also shielding the TPC from field breakdowns in a neighboring module.

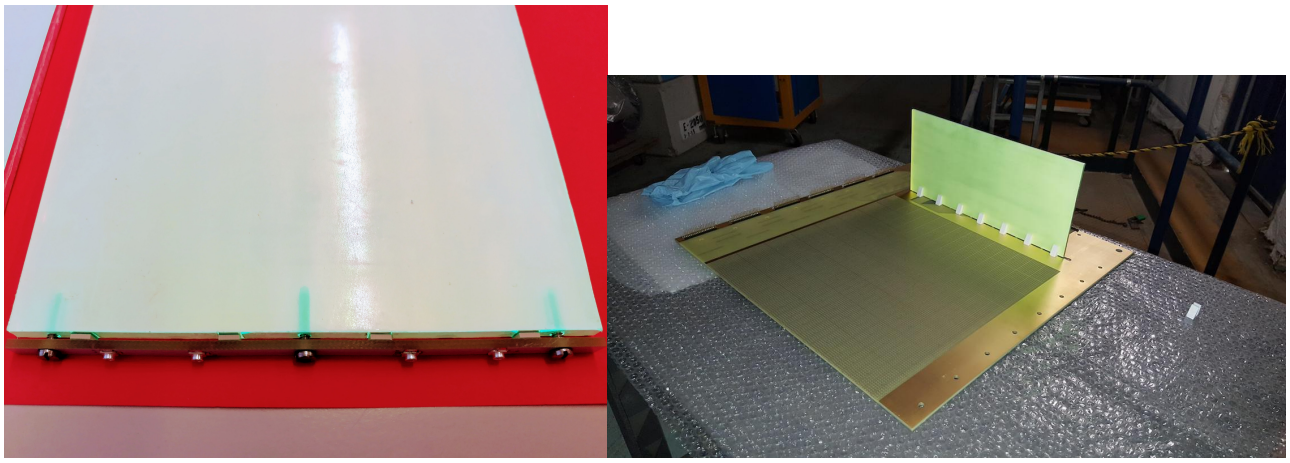
Each module is split into two TPCs by a central cathode made of an additional resistive layer on a G10 substrate. The segmented drift length does not require a high cathode voltage, and minimizes stored energy. For the 2×2 module footprint of $0.67\,\mathrm{m} \times 0.67\,\mathrm{m}$, and an E field of $1\,\mathrm{kV} \cdot \mathrm{cm}^{-1}$, a cathode potential of only 33 kV is required. Operating a LArTPC at this voltage is feasible without a prohibitive loss of active volume [42]. The high field is helpful for reducing drift time and the potential for pileup, minimizing the slow component of the scintillation light, reducing space charge effects, and providing robustness against loss of LAr purity.

The detector is oriented such that the cathodes are parallel to the beam. This minimizes the load on the readout electronics by spreading the event over more channels and reducing the required digitization rate for hit channels. In turn, this reduces the heat load generated at the charge readout and prevents localized boiling.

During filling and emptying of the cryostat, the argon flow is controlled by hydrostatic check valves located at the lower flange of the module, which require a minimal differential pressure of 15 mbar to open. The purity inside each module is maintained by means of continuous LAr recirculation through oxygen traps. Dirty argon is extracted from the base of the module, and is then pushed through oxygen traps outside the cryostat, clean argon then re-enters the module above the active volume. For optimal heat transport, the argon flow is directed along the cold electronics. To prevent dirty argon from the bath entering the modules, their interior is held at a slight over-pressure. For the 2×2, the dirty argon from all four modules is extracted by a single pump at the base of the cryostat with a four-to-one line, and after being filtered and cooled, the clean argon is pumped back in the module via a one-to-four line. A more extensive version of the same scheme is envisaged for the DUNE ND.

ArgonCube offers true 3D tracking information using the LArPix cryogenic ASIC [38] pixelated charge readout. LArPix ASICs amplify and digitize the charge collected at single-pixels in the cold to mitigate the need for analogue signal multiplexing, and thus produce unambiguous 3D information. Sixty-four pixels can be connected to a single LArPix ASIC. The baseline design for the 2×2 is a 4 mm pixel pitch, corresponding to 62.5k pixels m^{-2}. Pixelated anode planes are located on the two module walls parallel to the cathode; each plane is $1.28\,\mathrm{m}^2 \times 0.64\,\mathrm{m}^2$. The total area across all four modules is $6.6\,\mathrm{m}^2$, which corresponds to 410k pixels. The readout electronics utilize two field programmable gate array (FPGA) boards per module, connected to a single Ethernet switch. It should be noted that the pixel pitch may be reduced as prototypes develop, but this can be accommodated in the readout design.

The charge readout window (drift time) of 137 µs is long compared to the 10 µs [48] beam spill length in the NuMI and LBNF beams. For a 1 MW beam intensity, the expected rate of neutrino interactions at the DUNE ND is roughly 0.5 per spill per ArgonCube module. With LArPix, reconstruction issues are greatly simplified compared to a projective readout TPC. Tracks and connected energy deposits will frequently overlap in any 2D projection, but can be resolved easily with the full 3D readout. However, disconnected energy deposits, such as those from photon conversions or neutron interactions in the detector, cannot be associated easily to a specific neutrino interaction. This problem can be solved by incorporating fast timing information from the prompt



(a) ArCLight paddle (b) ArCLight mounted on a pixel readout PCB

Figure A.5: (a) A prototype ArgonCube light readout paddle. The paddle is 50 cm long and 10 cm, with four silicon photomultipliers (SiPMs) coupled to one end. Reproduced from Ref. [36]. (b) ArCLight paddle mounted on the PixLAr pixelated charge readout plane, as used in test beam studies at Fermilab.

scintillation light emitted in LAr. The module's opaque cathode and walls contain scintillation light within each TPC (half module), improving the detection efficiency of the prompt component of the scintillation light. Furthermore, attenuation due to Rayleigh scattering, characterized by an attenuation length of 0.66 m in LAr [49], is mitigated by the maximum photon propagation length of 0.3 m. It is desirable to have a large area photon detection system (PD system) to maximize the utility of scintillation light signals in the detector. To minimize any dead material within the active volume, it is also desirable that the light detection be as compact as possible. The solution pursued for the ArgonCube effort is ArCLight [39], which is a very compact dielectric light trap that allows for light collection from a large area, inside high E fields. An example ArCLight sheet is shown in Figure A.5. These sheets are mounted on the walls of the module, inside the field shell, aligned with the drift direction, between the anode and the cathode. The additional 5 mm deep dead volume is similar to the one caused by the charge readout in the perpendicular direction.

A.5.2.2 Dimensions of the ArgonCube Component of the DUNE ND

Since it is unrealistic to build a 25 m long LArTPC in order to contain a 5 GeV muon, the LArTPC dimensions have instead been optimized for hadronic shower containment [50], relying on a downstream spectrometer to analyze crossing muons. Hadronic showers are defined as contained if a reasonable efficiency across a wide range of kinematics is maintained, and there is no phase space with zero acceptance. The specific metric used is that >95% of hadronic energy has to be contained for interactions in the FV, excluding neutrons and their descendants.

To assess the efficiency, detector volumes of varying sizes were simulated in a neutrino beam. This provides a good measure of the efficiency of a given volume to contain different events, but it is not necessarily a good quantity to assess the required detector size. Many events are not contained because of their specific location and/or orientation. Cross section coverage remedies this deficiency by looking at the actual extent of the event, instead of its containment, at a random

position inside a realistic detector volume. However, events extending through the full detector will very likely never be contained in a real detector due to the low probability of such an event happening in exactly the right location (e.g., at the upstream edge of the detector). Therefore, the maximum event size needs to be smaller than the full detector size. For the ND simulation this buffer was chosen to be 0.5 m in all directions. In this way, this measure of cross section coverage allows us to look for phase-space regions which are inaccessible to particular detector volume configurations.

To find the optimal detector size in each dimension, two are held constant at their nominal values, while the third dimension is varied and the cross section coverage is plotted as a function of neutrino energy. This is shown for the dimension along the beam direction in Figure A.6. In this case, Figure A.6 shows us that 4.5 m would be sufficient, but to avoid model dependencies, 5 m has been selected. Increasing the length beyond 5 m does little to improve cross section coverage, but reducing to 4 m begins to limit coverage at higher energies. Note that 1 minus the cross section coverage gives the fraction of events that cannot be well reconstructed no matter where their vertex is, or how they are rotated within the FV. The optimized dimensions found using this technique were 3 m tall, 4 m wide, and 5 m along the beam direction. There is also a need to measure large angle muons that do not go into the HPgTPC. Widening the detector to 7 m accomplishes that goal without the added complication of a side muon detector.

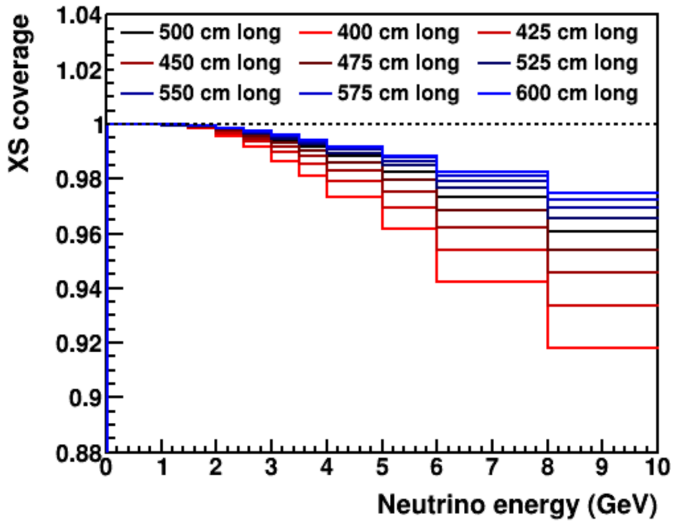


Figure A.6: Influence of the LArTPC size on hadron containment, expressed in terms of cross section coverage as a function of neutrino energy. Two dimensions are held constant at their nominal values, while the third is varied, in this case the height is held at 2.5 m and the width at 4 m. The optimal length is found to be 5 m. See text for explanation of cross section coverage [50].

A.5.2.3 ArgonCube Module Dimensions

The DUNE ND ArgonCube module dimensions are set to maintain a high drift field, $1\,\mathrm{kV}\cdot\mathrm{cm}^{-1}$, with minimal bias voltage, and to allow for the detection of prompt scintillation light while mitigating the effects of diffusion on drifting electrons. The prompt scintillation light, τ <6.2 ns [51], can be efficiently measured with a dielectric light readout with $\mathcal{O}(1)$ ns timing resolution, such

as ArCLight [39]. To reduce attenuation and smearing due to Rayleigh scattering, the optical path must be kept below the 0.66 m [49] scattering length. Additionally, the slow scintillation component can be further suppressed by operating at higher E fields [52], effectively reducing the ionization density [53] required to produce excited states.

A module with a 1 m × 1 m footprint split into two TPCs with drift lengths of 50 cm requires only a 50 kV bias. With ArCLight mounted either side of the 1 m wide TPC, the maximal optical path is only 50 cm. For a nonzero drift field, diffusion needs to be split into longitudinal and transverse components. Gushchin [54] report a transverse diffusion of $13\,\mathrm{cm}^2 \cdot \mathrm{s}^{-1}$ at $1\,\mathrm{kV} \cdot \mathrm{cm}^{-1}$. This results [55] in a transverse spread of 0.8 mm for the drift time of 250 µs, well below the proposed pixel pitch of 3 mm. The longitudinal component is smaller than the transverse [55], and is therefore negligible.

A.5.2.4 ND Dimensions

Though the acceptance study discussed in Section A.5.2.2 indicated a width of 4 m is sufficient to contain the hadronic component of most events of interest, the width has been increased to 7 m in order to mitigate the need for a side-going muon spectrometer. Figure A.7 shows the overall dimensions of the planned ArgonCube deployment in the DUNE ND. With an active volume of 1 m × 1 m × 3 m per module, the full ArgonCube detector corresponds to seven modules transverse to the beam direction, and five modules along it. It should be noted that the cryostat design is currently based on ProtoDUNE [56], and will be optimized for the ND pending a full engineering study.

A.5.2.4.1 Statistics in Fiducial Volume

Figure A.8 shows 37 million total CC ν_μ neutrino events per year within a 25 t FV in FHC mode at 1.07 MW (on-axis). Figure A.9 shows only the event rate for events where the visible hadronic system is fully contained, for the same FV and beam configuration. Note that for the visible hadronic system to be contained, all energy not associated with the outgoing lepton, or outgoing neutrons, was required to be contained.

For hadronic containment, there is a 30 cm veto region upstream and on all sides of the active volume, and 50 cm veto region downstream. The FV is then defined as 50 cm from all edges, with 150 cm downstream. Within the 25 t FV in FHC mode at 1.07 MW the number of fully reconstructed (contained or matched muon, discussed below, plus contained hadrons) CC ν_μ events per year is 14 million.

A.5.2.4.2 Muon Acceptance

Muons are considered as useful for physics if they stop in the active region of ArgonCube or if they leave the LAr detector and are reconstructed in a magnetic spectrometer downstream. Under the

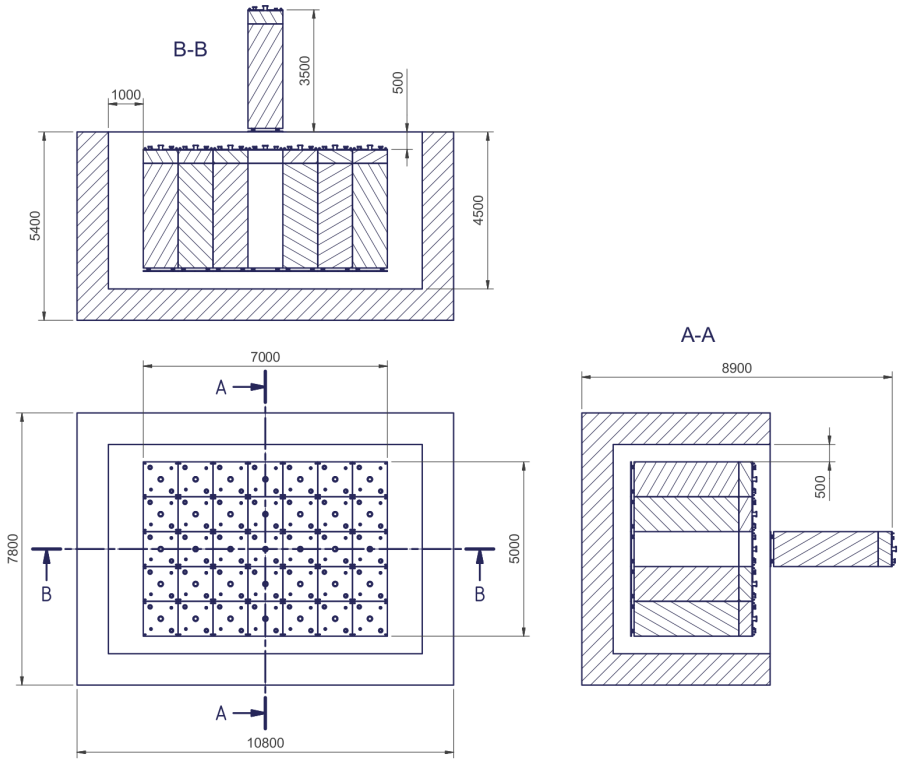


Figure A.7: The current ArgonCube Dimensions for the DUNE ND. The cryostat is based on Proto-DUNE [56], and yet to be optimized for the DUNE ND.

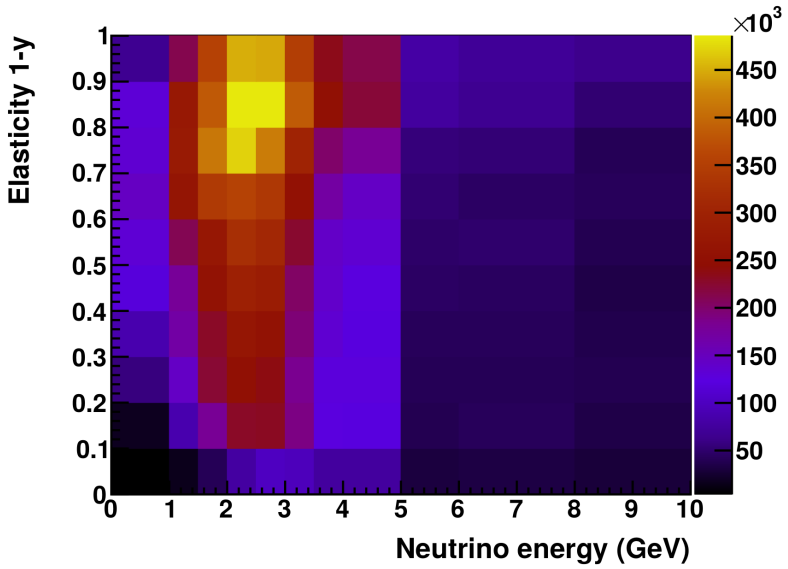


Figure A.8: All neutrino events in the nominal 25 t FV, in FHC at 1.07 MW, per year, rates are per bin. The elasticity is the fraction of the original neutrino energy carried by the outgoing lepton.

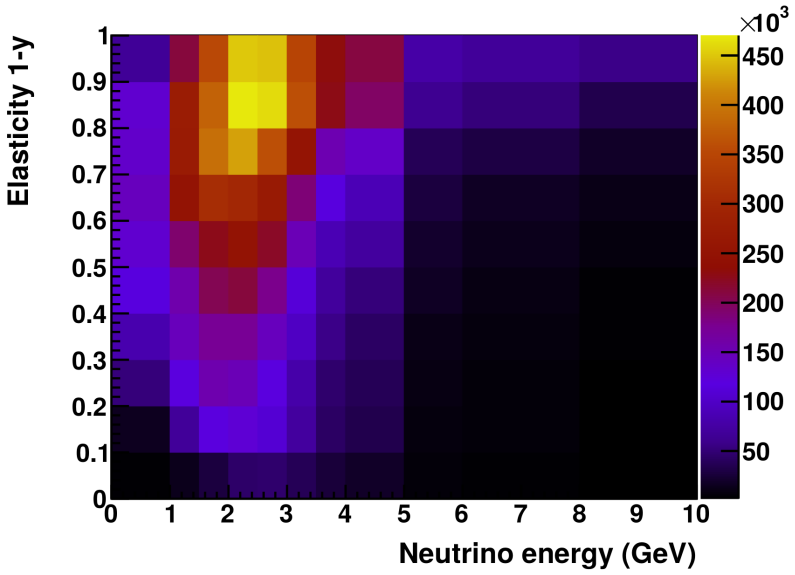


Figure A.9: Events where the visible hadronic system is contained within the nominal 25 t FV, in FHC at 1.07 MW, per year, rates are per bin. The elasticity is the fraction of the original neutrino energy that is carried by the outgoing lepton.

assumption that the downstream magnetic spectrometer is the multipurpose detector described in Section A.5.3, Figure A.10 shows the muon acceptance as a function of true neutrino energy (on the left) and muon energy (on the right). The acceptance dip at 1 GeV in muon energy is from muons that exit ArgonCube and are not reconstructed in the MPD downstream. This dip can be reduced by minimizing the passive material between the liquid argon and high pressure gaseous argon detectors.

ICARUS and MicroBooNE have used multiple Coulomb scattering to determine muon momentum [57]. This technique may prove to be useful for muons in ArgonCube and could mitigate somewhat the size of the dip in Figure A.10.

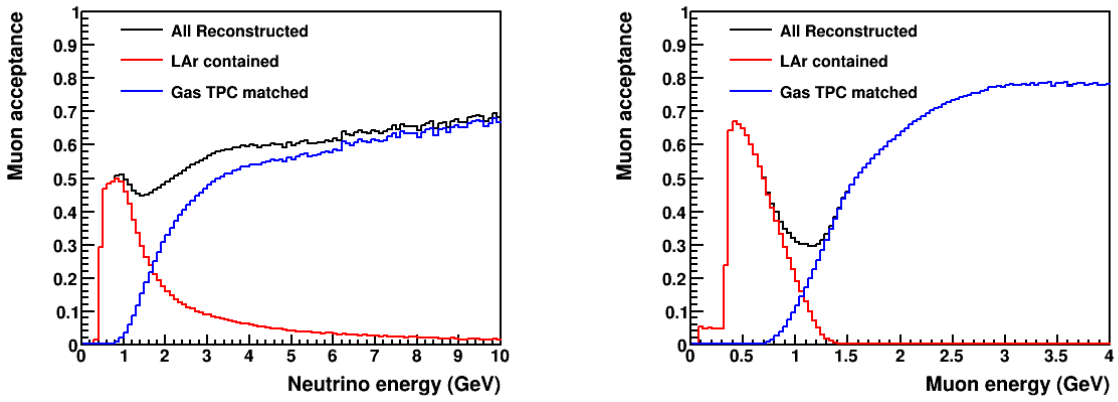


Figure A.10: Muon acceptance shown as a function of true neutrino energy (left) and true muon energy (right). The acceptance for muons that stop in ArgonCube is shown in red and that for muons reconstructed in the downstream magnetic spectrometer is shown in blue.

A.5.2.5 Acceptance vs. energy and momentum transfer

The acceptance of ArgonCube with the MPD acting as a downstream spectrometer can be studied in a more nuanced way by looking at it as a function of the energy q_0 and three-momentum q_3 transferred to the target nucleus. The energy transfer is simply $q_0 = E_\nu - E_\mu$. The three-momentum transfer is related to the four-momentum transfer Q and q_0 by $q_3 = \sqrt{Q^2 + q_0^2}$. These variables have long been used to study nuclear structure in electron scattering experiments.

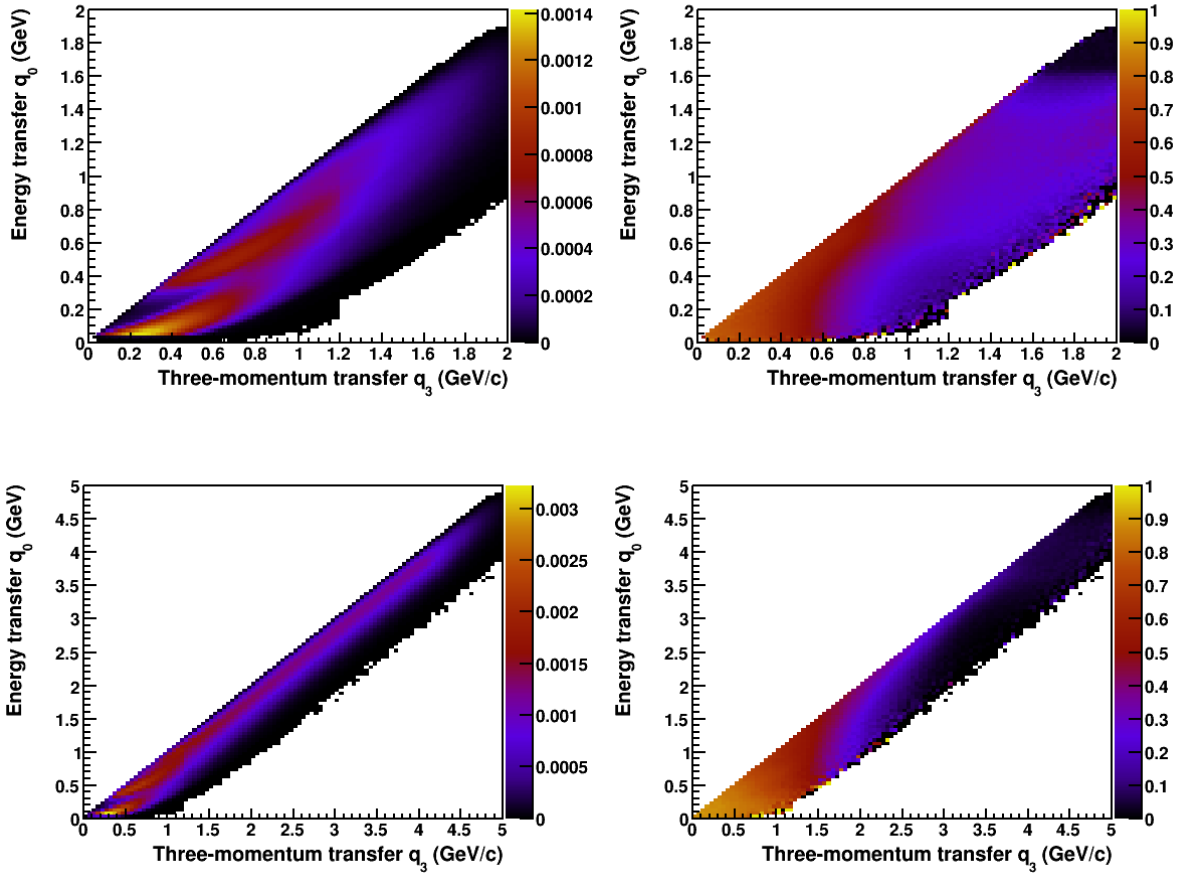


Figure A.11: Neutrino acceptance shown as a function of energy transfer and momentum transfer (q_0 and q_3) to the target nucleus. The units for q_0 and q_3 are GeV and GeV/c, respectively. The figures show the event rate (left) and the acceptance (right) for reconstructing the muon and containing the hadronic system. The top row was made for neutrinos with true neutrino energy between 1.0 and 2.0 GeV and the bottom was made for neutrinos between 4.0 and 5.0 GeV.

Figure A.11 shows the event rate (left figures) and acceptance (right figures) in bins of (q_3, q_0). The rows correspond to two neutrino energy bins. The top row is for E_ν between 1.0-2.0 GeV and it covers the first oscillation maximum. The second bin is for E_ν between 4.0-5.0 GeV. The rate histograms have "islands" corresponding to hadronic systems with fixed invariant mass. The islands are smeared by Fermi motion and decay width. The lower island in (q_3, q_0) corresponds to the quasi-elastic peak while the upper corresponds to the Δ resonance. One should note that the axes in the lower row cover a larger range of kinematic space than those in the upper row.

The acceptance is generally very good in the kinematic region where the vast majority of the events occur but is nowhere perfect. This is not necessarily a problem because the loss is chiefly geometrical. Losses typically occur in events with a vertex near one boundary of the detector where the muon, or hadronic system exits out that boundary. However for each lost event there is generally a set of symmetric events that are accepted because the final state is rotated by some angle about the neutrino beam axis (ϕ symmetry) or is closer to the center of the fiducial volume (x,y symmetry).

Regions where the acceptance is zero are problematic because they will introduce model dependence into the prediction of the rate at the far detector (which has a nearly 4π acceptance). Acceptances of even a few % in some kinematic regions are not necessarily a problem as long as the event rate is large enough to accumulate a statistically significant number of events. There is a potential danger if the acceptance varies quickly as a function of the kinematic variables because a small mismodeling of the detector boundaries or neutrino cross-sections could translate into a large mismodeling in the number of accepted events.

The size of the accepted event set decreases as a function of both q_0 and q_3 (and therefore E_ν) due to more energetic hadronic systems and larger angle muons. This can clearly be seen in the transition from the colored region to the black region in the $4.0 < E_\nu < 5.0\,\text{GeV}$ acceptance histogram shown in the lower right-hand corner of Figure A.11. The transition is smooth and gradual.

The acceptance for $1.0 < E_\nu < 2.0\,\text{GeV}$ (shown in the upper right-hand corner of Figure A.11) is larger than 10% except in a small region at high q_0 and q_3. Events in that region have a low-energy muon and are misidentified as neutral-current according to the simple event selection applied in the study. The fraction of events in that region is quite small, as can be seen in the upper left-hand plot of Figure A.11.

Figure A.12 summarizes the neutrino acceptance in the (q_3, q_0) plane as function of neutrino energy. The y axis shows the fraction of events coming from (q_3, q_0) bins with an acceptance greater than A_{cc}. The $A_{cc} > 0.00$ curve shows the fraction of events for which there is nonzero acceptance. For $E_\nu < 5.0\,\text{GeV}$ (the oscillation region) that fraction is greater than 99%. So, there are no significant acceptance holes. In the same energy region, more than 96% of events come from regions where the acceptance is greater than 3%.

A.5.2.6 Muon and Electron Momentum Resolution and Scale Error

For muons stopping in the LAr and for those with momentum measured in the downstream tracker (MPD), the energy scale uncertainty from ArgonCube is driven by the material model of the LAr and passive materials. This is expected to be known to <1%. Note that the B field in the MPD is expected to be known to about 0.5% from simulation and field maps made with Hall and NMR probes.

For electrons, the energy will be measured calorimetrically, rather than by range. The minimum ionizing particle (MIP) energy scale (charge/MeV) will be set by rock muons. The scaling to

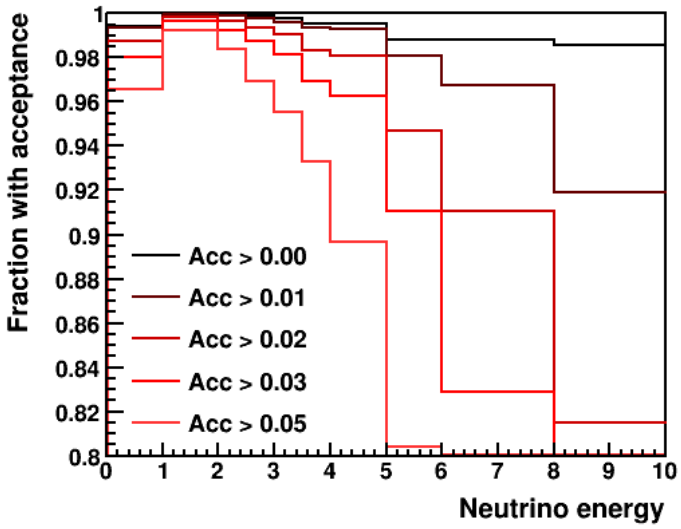


Figure A.12: This figure summarizes the neutrino acceptance in the (q_3, q_0) plane, as shown in Figure A.11, for all bins of neutrino energy (plotted in GeV). Here the quantity on the vertical axis is the fraction of events that come from bins in (q_3, q_0) with an acceptance greater than A_{cc}. As an example we consider the 4.0-5.0 GeV neutrino energy bin. The $A_{cc} > 0.03$ curve in that neutrino energy bin indicates that 96% of events come from (q_3, q_0) bins that have an acceptance greater than 3%.

more dense deposits from EM showers can give rise to uncertainties, i.e., recombination could be different. Such uncertainties can be reduced by taking data with ArgonCube modules in a test beam. Outside of this, a useful calibration sample of electrons up to 50 MeV comes from Michel electrons from stopping rock muons. The π^0 invariant mass peak is another good standard candle.

A.5.2.7 Tagging Fast Neutrons

Studies have shown that contained prompt scintillation light provides an important handle for neutron tagging, allowing for the association of detached energy deposits to the correct neutrino interaction using timing information. Such neutron tagging is important for minimizing the uncertainty on neutrino energy reconstruction, both for neutrons generated at a neutrino vertex and for hadronic showers that fluctuate to neutrons.

Figure A.13 shows a simulated beam spill in the 5 m × 4 m × 3 m LAr component of the DUNE ND[5]. It highlights the problem of associating fast-neutron induced energy deposits to a neutrino vertex using only collected charge.

By containing scintillation light, prompt light signals can be used to associate fast-neutron induced deposits back to a neutrino vertex anywhere within the detector. Figure A.14 shows the temporal distribution of neutrino vertices within a representative, randomly selected, beam spill. The mean

[5]Note that this study was performed before the detector width was increased to 7 m, as described in Section A.5.2.4.

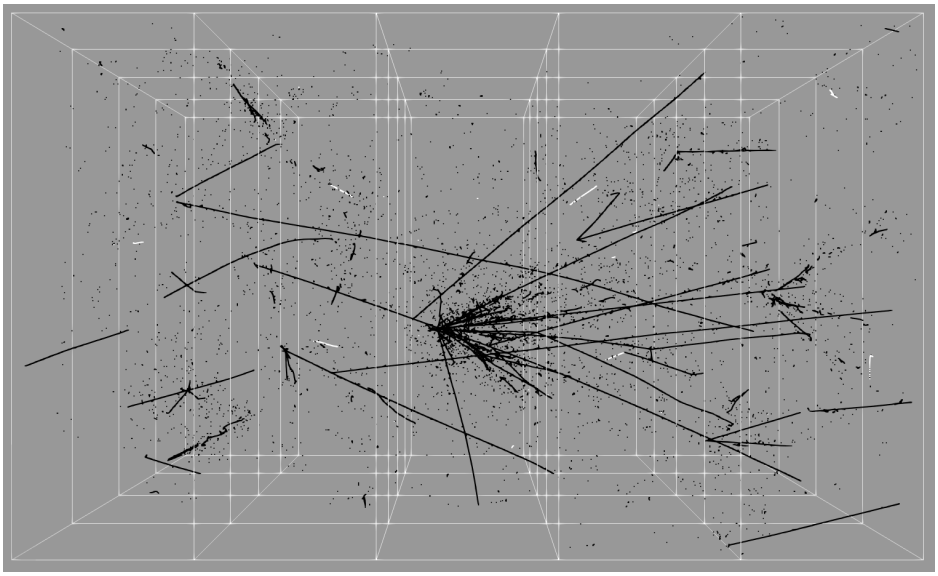


Figure A.13: A beam spill in the LAr component of the DUNE ND. The detector volume is 5 m × 4 m × 3 m. Fast-neutron induced recoiling proton tracks, with an energy threshold greater than ∼ 10 MeV, are shown in white. The black tracks are all other energy deposits sufficient to cause charge collected at the pixel planes.

separation of neutrino vertices is 279 ns, with all fast-neutron induced energy deposits occurring <10 ns after each neutrino interaction.

A.5.2.8 Neutrino-Electron Elastic Scattering

Neutrino scattering on atomic shell electrons, $\nu_l(\overline{\nu}_l) + e^- \rightarrow \nu_l(\overline{\nu}_l) + e^-$, is a purely electroweak process with a known cross section as function of neutrino energy, E_ν, in which all neutrino flavors participate, albeit with different cross sections. This process is not affected by nuclear interactions and has a clean signal of a single very forward-going electron. MINERvA [58] has used this technique to characterize the NuMI beam flux normalization (running in the NuMI low-energy mode), although the rate and detector resolution were insufficient to make a shape constraint. It has been investigated as a cross section model-independent way to constrain the neutrino flux at the DUNE ND.

For a neutrino-electron sample, E_ν could, in principle, be reconstructed event-by-event in an ideal detector using the formula

$$E_\nu = \frac{E_e}{1 - \frac{E_e(1-\cos\theta_e)}{m_e}}, \tag{A.8}$$

where m_e and E_e are the electron mass and outgoing energy, and θ_e is the angle between the outgoing electron and the incoming neutrino direction. The initial energy of the electrons are low enough to be safely neglected (∼10 keV). It is clear from Equation A.8 that the ability to constrain the shape of the flux is critically dependent on the energy- and, in particular, angular-resolution of electrons. For a realistic detector, the granularity of the E_ν shape constraint (the binning) depends on its performance. Additionally, the divergence of the beam (few mrad) at the DUNE ND site is

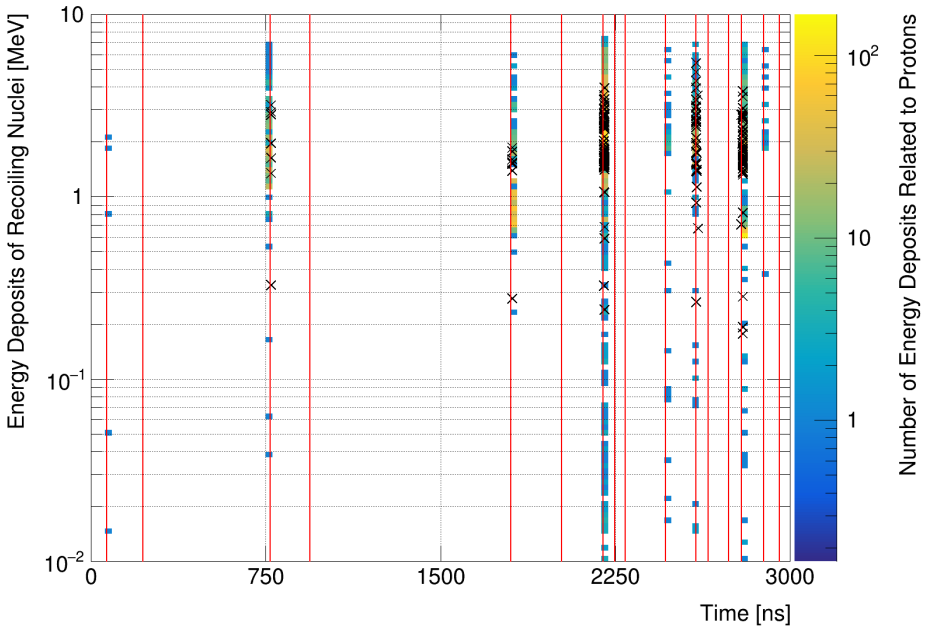


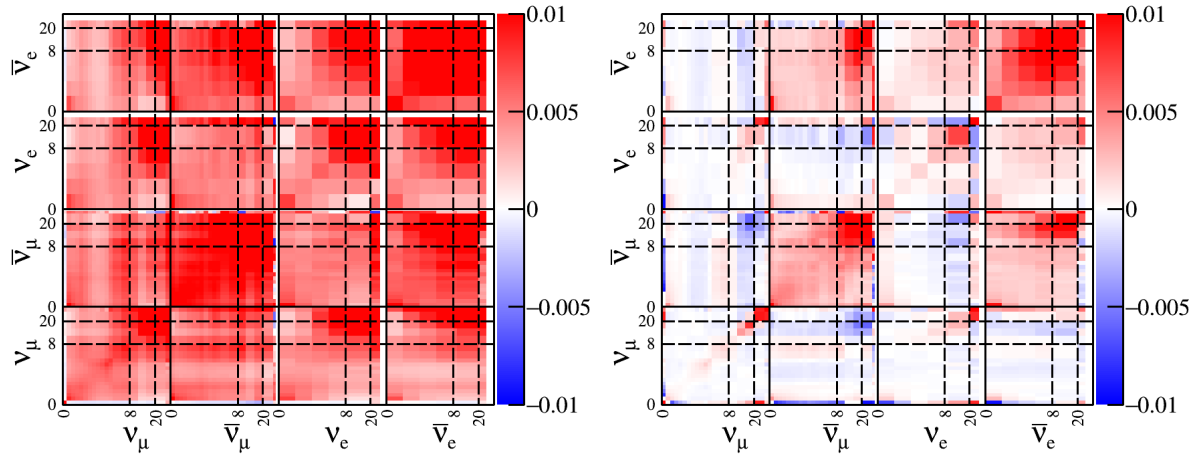
Figure A.14: The temporal distribution of neutrino vertices (red lines) within a beam spill in the LAr component of DUNE ND. The mean separation of neutrino vertices is 279 ns. The filled bins show the number of hits due to recoiling protons, crosses indicate a hit due to a recoiling ^{2}H, ^{3}H, ^{2}He or ^{3}He nucleus. All fast-neutron induced energy deposits occur <10 ns after each neutrino interaction.

a limiting factor to how well the incoming neutrino direction is known.

In work described in Ref. [59], the ability for various proposed DUNE ND components to constrain the DUNE flux is shown using the latest three-horn optimized flux and including full flavor and correlation information. This was used to determine what is achievable relative to the best performance expected from hadron production target models. When producing the input flux covariance matrix, it was assumed that an NA61 [60] style replica-target experiment was already used to provide a strong prior shape constraint. Detector reconstruction effects and potential background processes are included, and a constrained flux-covariance is produced following the method used in Ref. [58].

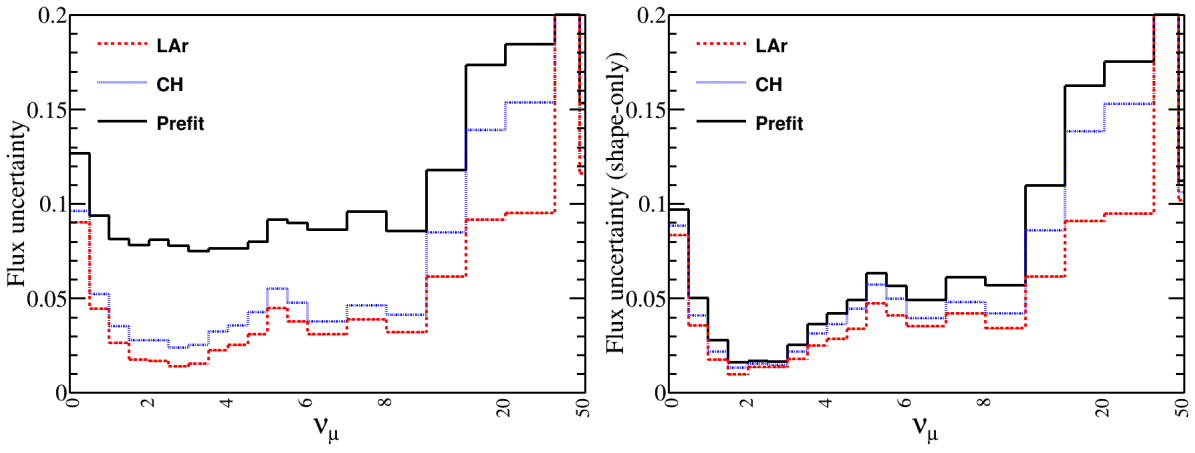
The impact of the neutrino-electron scattering constraint on the flux covariance is shown in Figure A.15 for FHC and a five year exposure of the nominal 35 t ArgonCube LAr detector (corresponding to ∼22k neutrino-electron events). It is clear that the overall uncertainty on the flux has decreased dramatically, although, as expected, an anticorrelated component has been introduced between flavors (as it is not possible to tell what flavor contributed to the signal on an event-by-event basis). Similar constraints are obtained for RHC running.

Figure A.16 shows the flux uncertainty as a function of E_ν for the ν_μ-FHC flux, for a variety of ND options. In each case, the constraint on the full covariance matrix is calculated (as in Figure A.15), but only the diagonal of the ν_μ portion is shown. In the flux peak of ∼2.5 GeV, the total flux uncertainty can be constrained to ∼2% for the nominal LAr scenario, and the constraint from other detector types is largely dictated by the detector mass. Clearly the neutrino-electron



(a) FHC pre-fit (b) FHC post-fit

Figure A.15: Pre- and post-fit FHC flux covariance matrices for the nominal 35 t ArgonCube LAr detector using a five-year exposure.



(a) Rate+shape (b) Shape-only

Figure A.16: Rate+shape and shape-only bin-by-bin flux uncertainties as a function of neutrino energy for a five year exposure with various detector options, compared with the input flux covariance matrix before constraint.

scattering sample at the DUNE ND will be a powerful flux constraint. However, it is also clear that the ability to constrain the shape of the flux is not a drastic improvement on the existing flux covariance matrix, and none of the possible detectors investigated added a significantly stronger constraint. That said, the neutrino-electron sample is able to make in situ measurements of the flux prediction, and is able to diagnose problems with the flux prediction in a unique way.

A.5.3 Multipurpose Detector

The multipurpose detector (MPD) extends and enhances the capabilities of the LArTPC. It does this by providing a system that will measure the momentum and sign of charged particles exiting the LArTPC and, for neutrino interactions taking place in the MPD, it will extend charged particle measurement capabilities to lower energies than achievable in the far or near LArTPCs. This capability enables further constraints of systematic uncertainties for the LBL oscillation analysis. The MPD is a magnetized system consisting of a high-pressure gaseous argon time projection chamber (HPgTPC) and a surrounding ECAL. The detector design will be discussed in more detail in a later section.

MPD goals

- Measure particles that leave the LAr ND component and enter the MPD

  The LAr component of the DUNE ND will not fully contain high-energy muons or measure lepton charge. A downstream MPD will be able to determine the charge sign and measure the momenta of the muons that enter its acceptance, using the curvature of the associated track in the magnetic field.
- Constrain neutrino-nucleus interaction systematic uncertainties

  In its 1-ton gaseous argon FV, the MPD will collect 1.5×10^6 CC muon neutrino interactions per year (plus 5×10^5 NC muon neutrino interactions). The very low energy threshold for reconstruction of tracks in the HPgTPC gives it a view of interactions that is more detailed than what is seen in the LAr, and on the same target nucleus. The associated ECAL provides excellent ability to detect neutral pions, enabling the MPD to measure this important component of the total event energy while also tagging the presence of these pions for interaction model studies.

  The ability to constrain "known unknowns" is a high priority of the MPD. One example is nucleon-nucleon correlation effects and meson exchange currents in neutrino-nucleus scattering. Although a few theoretical models that account for these effects are available in neutrino event generators, no model reproduces well the observed data in NOvA, MINERvA, or T2K. These experiments therefore use empirical models tuned to the limited observables in their detector data. Tuning results in better agreement between simulation and data, although still not perfect. In addition, this type of empirical tuning leaves some large uncertainties, such as the four-momentum transfer response, the neutrino energy dependence of the cross sections (where models disagree, and a "model spread" is typically used for the uncertainty), and the relative fractions of final state nucleon pairs (pp vs. np).

  Another example of a "known unknown" for which the MPD will provide a more stringent

cross section constraint than the LArTPC is the case of single and multiple pion production in CC neutrino interactions. An MPD-based measurement of these processes will be implemented in the DUNE LBL oscillation analysis in the near future, making use of the high-purity samples of CC-0π, CC-1π, and CC-multi-π events in the gaseous argon, separated into π^+ and π^- subsamples and binned in neutrino energy and other variables of interest. Figure A.17 illustrates two simple differences among the HPgTPC CC-1π subsamples; it is still to be determined which variables will be the most useful in the LBL oscillation analysis.

The relative lack of secondary interactions for particles formed in neutrino interactions in the gaseous argon FV will provide samples with a less model dependent connection to the particles produced in the primary interaction. These secondary interactions are a significant effect in denser detectors [1] and this crosscheck/validation of the reinteraction model is likely to be useful in understanding the full energy response of the liquid detectors.

The MPD will measure ratios of inclusive, semi-exclusive, and exclusive cross sections as functions of neutrino energy, where the flux cancels in the ratio. These ratios will be measured separately for NC and CC events, and the NC to CC ratio itself will be measured precisely with the MPD. The ratios of cross sections for different pion, proton, and kaon multiplicity will help constrain interaction models used in the near and far liquid detectors.

The HPgTPC will have better capability than the LArTPC to distinguish among particle species at low momentum using dE/dx measurements. Some muon/pion separation is possible via dE/dx for very low momenta, and protons are very easily distinguished from pions, muons, and kaons for momenta below 2 GeV/c, as shown in Figure A.29. At higher momenta, the magnet makes it possible to easily distinguish π^+ from μ^- (or π^- from μ^+), as has been done in T2K near-detector fits for oscillation analyses. The fact that pions will interact hadronically far less often in the gas than in the liquid will give another important handle for constraining uncertainties in the LArTPC. These aspects give the MPD a significant complementarity to the LArTPC, which is not magnetized. Since the target nucleus in the MPD is the same as that in the near and far LArTPCs this information feeds directly into the interaction model constraints without complicating nuclear physics concerns.

Finally, having a ND that can see one level deeper than the far detector keeps open the possibility to investigate "unknown unknowns" as well. Since the MPD will identify and measure interactions more accurately than can be done in the LArTPC, it will provide the ability to investigate more deeply our observations in the liquid argon, and the flexibility to address other unexpected things we may encounter.

- **Precisely and accurately measure all components of the neutrino flux**

  The magnetic field of the MPD enables the precise determination of momenta of charged particles escaping the upstream LArTPC. Because the ND is necessarily smaller than the FD, near-far differences arising from the different containment fractions are compensated by the fact that the ND has a magnetic spectrometer. Also, higher-energy particles from the neutrino interaction will be measured better in the MPD than in the liquid ND or FD (for example, non-contained muons), constraining the effects of energy feed-down in the liquid detectors.

  The ability to separate charge signs will allow the MPD to measure the relative contributions of ν_μ and $\bar{\nu}_\mu$ in both the neutrino beam and the antineutrino beam, as well as distinguishing ν_e from $\bar{\nu}_e$ components. These components are important to anchor the oscillation fit. Otherwise, reliance on the beam modeling is needed to predict the small but uncertain fractions

of wrong-sign neutrinos in the beams. Stopping muons' Michel signatures can be used on a statistical basis in the far detector, as the decay rates differ for μ^+ and μ^-, but that is after oscillation has distorted the spectrum. No corresponding test is present for ν_e.

- **Constrain π^0 backgrounds to ν_e events**

  An accurate measurement of backgrounds to the ν_e appearance measurement is a critical input for far detector oscillation analyses. In the LArTPC, the largest background to ν_e's is NC-π^0 interactions in which one photon is not detected and the other is mistakenly identified as an electron. The HPgTPC and ECAL together provide a unique capability to constrain NC-π^0 backgrounds that are misidentified as ν_e CC in the LArTPC. The HPgTPC will collect a reduced background sample of $\sim$ 20k ν_e CC events per year. The LArTPC detector measures ν_e+ mis-ID'ed π^0 events, while the MPD measures ν_e CC events alone (by rejecting all π^0 events using the ECAL). The MPD sample will reduce backgrounds from NC-π^0 events because the photon conversion length in gas is much greater than that in the liquid, and photons from π^0 decays will not often convert in the gas volume of the HPgTPC in such a way as to fake $e^{\pm}$ from ν_e interactions. The ECAL, however, will have excellent ability to detect the π^0 decays, enabling the MPD to reject π^0 events as background to ν_e's.

  The MPD measurement of ν_e CC events can be scaled to the LArTPC density and volume and corrected to the same acceptance as the LArTPC in order to provide a constraint on the π^0-misID. The difference of the two: $(\nu_e^{\text{LAr}}$ + mis-ID'ed $\pi^0) - (\nu_e^{\text{GAr-scaled-to-LAr}})$ yields the π^0-misID rate in LArTPC. This measurement of the backgrounds to ν_e's would not be possible at all if the MPD were replaced by a simple muon range detector. It would also not be easy to extrapolate to the LArTPC if the target material of the MPD were not argon.

- **Measure energetic neutrons from ν-Ar interactions via time-of-flight with the ECAL**

  Neutron production in neutrino and antineutrino interactions is highly uncertain, and is a large source of neutrino energy misreconstruction. In the HPgTPC+ECAL system, a preliminary study of the time-of-flight from the HPgTPC neutrino interaction point to hits in the ECAL is encouraging, indicating that ToF can be used to detect and correctly identify neutrons. With the current ECAL design, an average neutron detection efficiency of 60% is achieved by selecting events in which an ECAL cell has one hit with more than 3 MeV. This is still very preliminary work, and further studies to understand the impact of backgrounds and ECAL optimization (strip vs. tile, overall thickness) are underway.

- **Reconstruct neutrino energy via spectrometry and calorimetry**

  Although all neutral particles from an event must be measured with the ECAL in the MPD, the HPgTPC will be able to make very precise momentum measurements of charged particle tracks with a larger acceptance than the upstream LArTPC, including tracks created by high-momentum exiting particles, which allows the measurement of the entire neutrino spectrum. In addition, short and/or stopping tracks will be measured via dE/dx. The sum of this capability provides a complementary event sample to that obtained in the LAr, whose much higher density leads to many secondary interactions for charged particles. The two methods of measurement in the MPD will help in understanding the LAr energy resolution.

- **Constrain LArTPC detector response and selection efficiency**

  The MPD will collect large amounts of data in each of the exclusive neutrino interaction channels, with the exception of $\nu - e$ elastic scattering, where the HPgTPC sample will be too small to be useful. The high statistics ν-Ar interaction samples will make it possible to directly crosscheck every kinematic distribution that will be used to constrain the fluxes and

cross sections. Typically these checks will be over an extended range of that variable. The high purity of the MPD samples and low detection threshold for final state particles in the HPgTPC will give a benchmark or constraint on LArTPC detector response and selection efficiencies for each of the interaction channels.

Using the events collected in the HPgTPC (where selection and energy reconstruction are easy), the performance of LAr event selection and energy reconstruction metrics can be tested by simulating the well-measured HPgTPC four-vectors in the LArTPC. This allows the validation of the LArTPC reconstruction performance on these events. This process is expected to reduce the errors in the LArTPC detector energy response model.

MPD strengths The strengths of the MPD enable it to reach the goals above and to augment the capabilities of the LArTPC. Below are a few examples of its strengths relative to the LArTPC:

- High-fidelity particle charge determination via magnetic curvature. This is the only detector that can measure electron and positron charge.
- Precise and independent measurement of particle momentum, via magnetic curvature, will allow the measurement of the momentum of higher-energy charged particles without requiring containment. This extends the utility of the ND, especially for the high-energy beam tune. The absolute momentum scale is easily calibrated in the magnetic spectrometer and provides a cross-check on energy loss through ionization measurements. Calibration strategies for the magnetic tracking include pre-assembly field maps, *in situ* NMR probes, and K^0_s and Λ^0 reconstruction.
- Particle identification through dE/dx. The gaseous argon TPC has better separation power of particle species by dE/dx than the liquid because the momentum can be measured along with energy loss.
- High-resolution imaging of particles emerging from the ν-Ar vertex (including nucleons). The reconstruction threshold in the gas phase is much lower than the threshold in liquid because particles travel further in the low density medium, e.g., a proton requires only 3.7 MeV kinetic energy to make a 2 cm track in 10 atmospheres of gaseous argon, while a 3.7 MeV proton in liquid can only travel 0.02 cm. Figure A.18 demonstrates the difference in the thresholds for reconstructing protons in the HPgTPC and the LArTPC in light of the energy spectra of final state protons from a selection of types of neutrino interactions at the DUNE ND. The LArTPC threshold is what has been achieved in MicroBooNE up to now, and the HPgTPC threshold is what has been achieved with the tools discussed in Section A.5.3.2.3.
- Separation of tracks and showers for less-ambiguous reconstruction. Particle tracks are locally helical and tend to bend away from each other in the magnetic field as they travel from a dense vertex. Electromagnetic showers do not occur in the gas, but in the physically separate ECAL. By contrast, in a LArTPC tracks and showers frequently overlap. The measurement resolution scales are comparable between the liquid and the gas, but the distance scales on which interactions occur are much longer in the gas, allowing particles to be identified and measured separately more easily.
- The measurement of energetic neutrons through time-of-flight with ECAL is a potential game-changer for validating energy reconstruction. Preliminary studies of the HPgTPC+ECAL system indicate that an average neutron detection efficiency of 60% can be achieved via a

time-of-flight analysis. A study of the impact of backgrounds is underway, but initial studies are encouraging.

- The HPgTPC is able to measure the momentum of particles over almost the full solid angle. Particles that are emitted at a large angle with respect to the beam have a high probability of exiting the LAr without leaving a matching track in the MPD. However, events collected in the HPgTPC, with its $\simeq 4\pi$ coverage, can be used in the regions of phase space where the exiting fraction is high in the liquid argon to ensure that the events are accurately modeled in all directions in the FD.
- The MPD neutrino event sample, while smaller than the LArTPC sample, is a statistically independent sample. Moreover, the systematic uncertainties of the MPD will be very different than the LArTPC and likely smaller in many cases. This will allow the MPD to act as a systematics constraint for the LArTPC.

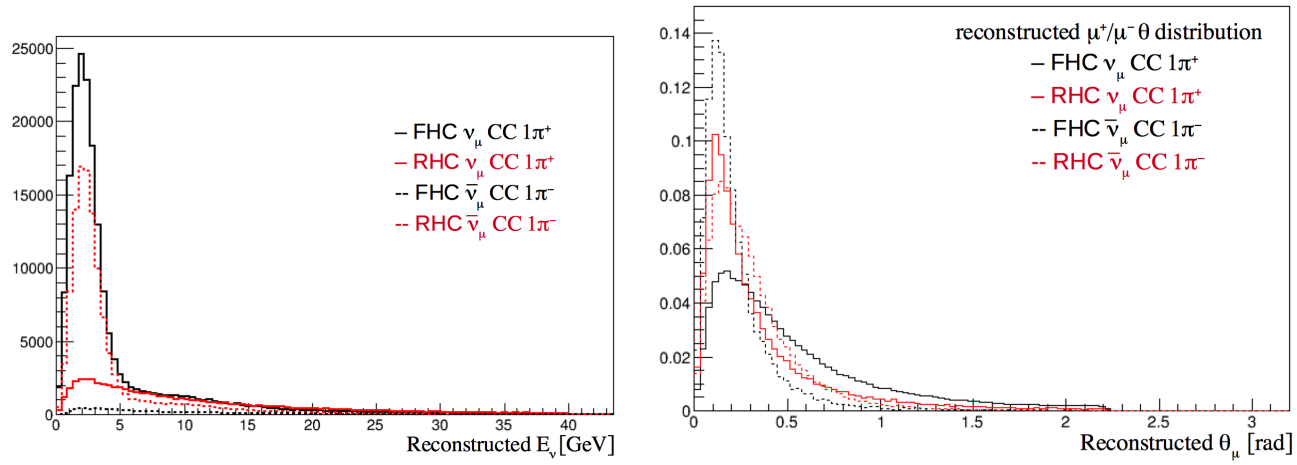


Figure A.17: Representative differences among subsamples of CC ν_μ interactions with one π^+ (solid lines) and CC $\bar{\nu}_\mu$ interactions with one π^- (dashed lines). The forward- and reverse- horn current samples are shown in black and red, respectively. Left: Reconstructed neutrino energy spectra, normalized to the same number of protons on target. Right: Angle of outgoing muon relative to neutrino direction, normalized to unit area for shape comparison.

A.5.3.1 MPD Technical Details

A.5.3.1.1 High-Pressure Gaseous Argon TPC

The basic geometry of the HPgTPC is a gas-filled cylinder with a HV electrode at its mid-plane, providing the drift field for ionization electrons. It is oriented inside the magnet such that the magnetic and E fields are parallel, reducing transverse diffusion to give better point resolution. Primary ionization electrons drift to the end plates of the cylinder, which are instrumented with multi-wire proportional chambers to initiate avalanches (gas gain) at the anode wires. Signals proportional to the avalanches are induced on cathode pads situated behind the wires; readout of the induced pad signals provides the hit coordinates in two dimensions. The drift time provides the third coordinate of the hit.

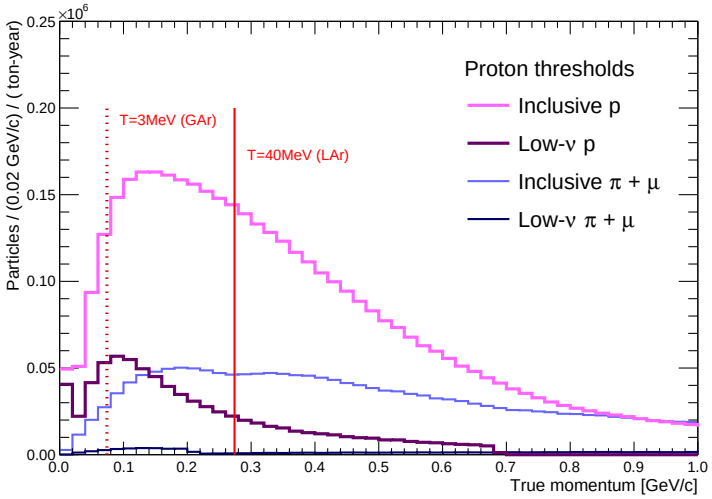


Figure A.18: The momentum spectra of protons ejected from neutrino interactions in argon, for several categories of interaction types. The vertical lines indicate the lowest momentum protons that have been reconstructed using existing automated reconstruction tools, where the dotted line is the HPgTPC threshold, and the solid line is the LArTPC threshold (from MicroBooNE).

The details of the HPgTPC design will be based closely on the design of the ALICE detector [61] shown in Figure A.19. Two readout planes sandwich a central HV electrode (25 μm of aluminized mylar) at HV that generates the drift field, which is parallel to a 0.5 T magnetic field. On each side of the electrode, primary ionization electrons drift up to 2.5 m to reach the endplates, which are segmented azimuthally into 18 trapezoidal regions instrumented with readout chambers (ROCs) that consist of MWPC amplification regions and cathode pad planes to read out the signals. A cross sectional view of an ALICE MWPC-based ROC is shown in Figure A.20. The ROCs are built in two sizes: a smaller inner readout chamber (IROC) and a larger outer readout chamber (OROC). The trapezoidal segments of the endplates are divided radially into inner and outer sections, and the IROCs and OROCs are installed in those sections. The existing IROCs and OROCs will become available in 2019, when they are scheduled to be replaced by new GEM-based ROCs for upgraded pileup capability in the high rate environment of the LHC. For the DUNE HPgTPC, the existing ROCs are more than capable of providing the necessary performance in a neutrino beam.

In the ALICE design, the innermost barrel region was isolated from the TPC and instrumented with a silicon-based inner tracker; for the DUNE HPgTPC, the inner field cage labeled in Figure A.19 will be removed, and the entire inner region will be combined to make a single gas volume for the TPC. New ROCs will be built to fill in the central uninstrumented region, which is 1.6 m in diameter, left by reusing the existing ALICE chambers. The active dimensions of the HPgTPC will be 5.2 m in diameter and 5 m long, which yields an active mass of $\simeq$ 1.8 t.

MPD Pressure Vessel The preliminary design of the pressure vessel, presented in Figure A.21, accounts for the additional volume needed to accommodate the TPC field cage, the ROC support structure, front-end (FE) electronics, and possibly part of the ECAL.

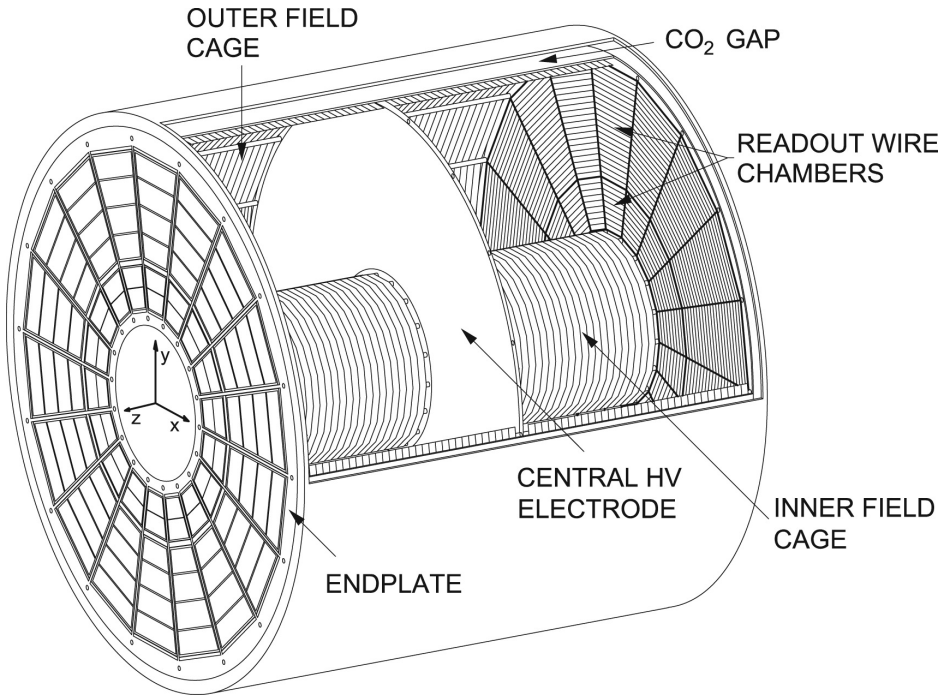


Figure A.19: Diagram of the ALICE TPC, from Ref. [62]. The drift HV cathode is located at the center of the TPC, defining two drift volumes, each with 2.5 m of drift along the axis of the cylinder toward the endplate. The endplates are divided into 18 sectors, and each endplate holds 36 readout chambers.

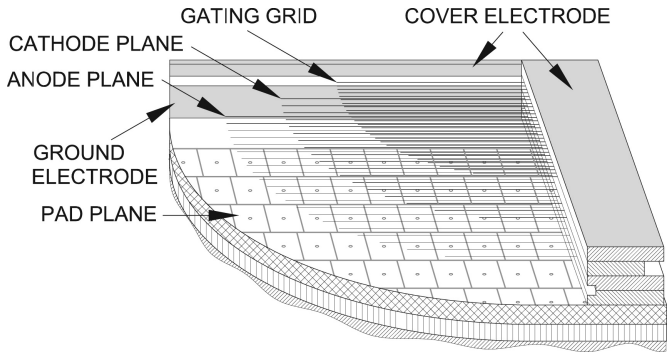


Figure A.20: Schematic diagram of the ALICE MWPC-based ROC with pad plane readout, from Ref. [62].

The pressure vessel can be fabricated from aluminum or stainless steel, has a cylindrical section that is 6 m in diameter and 6 m long and utilizes two semi-elliptical end pieces with flanges. The walls of the cylinder barrel section are $\simeq 1.6X_0$ in thickness in the case of stainless steel or $\simeq 0.3X_0$ in the case of Al 5083. Further reduction of the thickness in radiation lengths can be accomplished with the addition of stiffening rings. This preliminary design includes two flanged endcaps. However, these large flanges are the cost driver for the pressure vessel and, therefore, vessel designs with a single flange will also be considered. As an example, DOE/NETL-2002/1169 (Process Equipment Cost Estimation Final Report) indicates that a horizontal pressure vessel of the size indicated here and rated at 1034 kPag (150 psig) (approximately 10 atmospheres) is costed at \$150k ($\simeq$ \$210k in 2019 dollars). The budgetary estimate for a vessel with two flanges was \$1.2M with the flanges driving the cost. DOE/NETL-2002/1169 also indicates that pressure is not a significant cost driver. Reducing the pressure from 1034 kPag to 103 kPag (15 psig) only reduces the basic (\$150k) vessel cost by a factor of two.

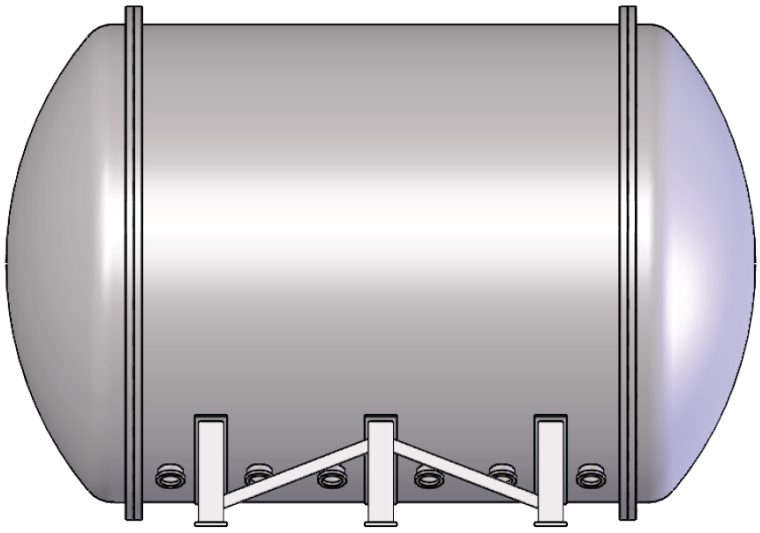


Figure A.21: Pressure vessel preliminary design.

A.5.3.1.2 Electromagnetic Calorimeter (ECAL)

The MPD ECAL concept is based on a high granularity calorimeter to provide direction information in addition to the energy measurement of electromagnetic showers and an efficient rejection of background. The principal role of the ECAL is to reconstruct photons directly produced in neutrino interactions and originating from π^0 decays, providing a measurement of the photon's energy and direction to enable the association of photons to interactions observed in the HPgTPC and the determination of the decay vertex of the π^0s. In the case of ν_e measurements in the HPgTPC, the ECAL will play an important role in rejecting events with π^0 decays, which represent a background to ν_e interactions in the LArTPC. The ECAL can also be used to reject external backgrounds, such as rock neutrons and muons, providing a sub-nanosecond timestamp [63] for each hit in the detector. As the ECAL uses hydrogen-rich scintillator, it is assumed to have capabilities to provide neutron detection, and studies are underway to determine the performance of neutron detection.

ECAL Design The ECAL design is inspired by the design of the CALICE analog hadron calorimeter (AHCAL) [64].

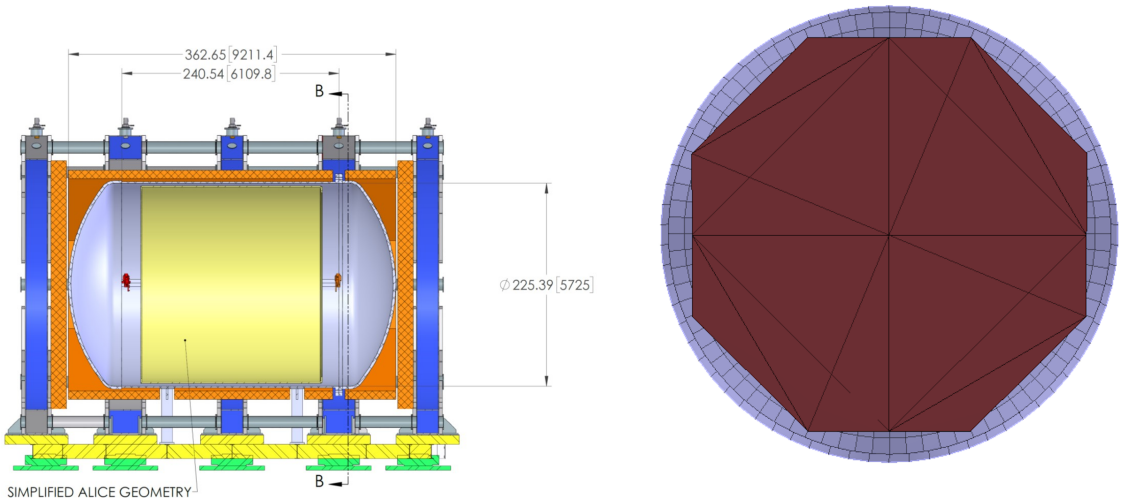


Figure A.22: On the left, the conceptual design of the MPD system for the ND. The ECAL (orange) is located outside the HPgTPC pressure vessel. On the right, a conceptual design of the ECAL endcap system.

The ECAL is shown in Figure A.22. The barrel has an octagonal shape with each quadrant composed of several trapezoidal modules. The ECAL endcap has a similar design providing hermeticity and a large solid-angle coverage. Each module consists of scintillating layers of polystyrene as active material read out by SiPMs, sandwiched between absorber sheets. The scintillating layers consist of a mix of tiles with dimensions between 2×2 cm^2 to 3×3 cm^2 (see Figure A.23) and cross-strips with embedded wavelength shifting fibers to achieve a comparable effective granularity. The high-granularity layers are concentrated in the front part of the detector, since that has been shown to be the most relevant factor for the angular resolution [65]. With the current design, the number of channels is of the order 2.5 to 3 million. A first design of the ECAL and the simulated performance has already been studied in [65].

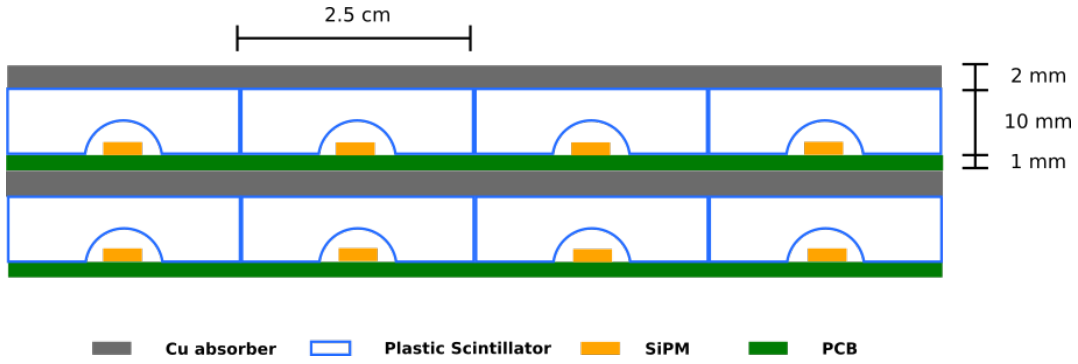


Figure A.23: Conceptual layout of the ECAL showing the absorber structure, scintillator tiles, SiPMs and PCB.

In the preliminary design, it was assumed that the full ECAL barrel is outside the pressure vessel. The thickness of the pressure vessel has an impact on the calorimeter energy resolution [65], and

more recent designs of the pressure vessel have reduced its thickness. Currently, the ECAL design is undergoing a detailed design study in order to further optimize the detector design, cost, and performance.

A.5.3.1.3 Magnet

Two magnet designs are under consideration to house the HPgTPC and the ECAL. One is a UA1-type conventional electromagnet, the other is based on a superconducting Helmholtz-coil-like design. The common requirement is a central magnetic field of 0.5 T with ±20% uniformity over the TPC volume (5 m long and 5 m in diameter). With the current design of the access shaft (11.8 m diameter), the clear diameter is about 7.8 m. Recent studies for the construction of an electromagnet similar to the UA1 magnet predict that the cost of the design, procurement, infrastructure (power and cooling) and assembly will be in excess of $20 million, with operation costs of approximately $1.6M per year of running. Because of this, the main focus has been on the superconducting design.

Superconducting Magnet The SC magnet design is a Helmholtz-coil-like configuration, air core, five coil magnet system. Three central coils produce the analyzing field and two outer shielding coils help contain stray field. The advantage of this design is that little or no iron is used for field containment or shaping. This eliminates background coming from neutrino interactions in the iron, which for the normal-conducting magnet case is the largest component of the background. Figure A.24 shows the magnet concept indicating the five-coil arrangement and support structure.

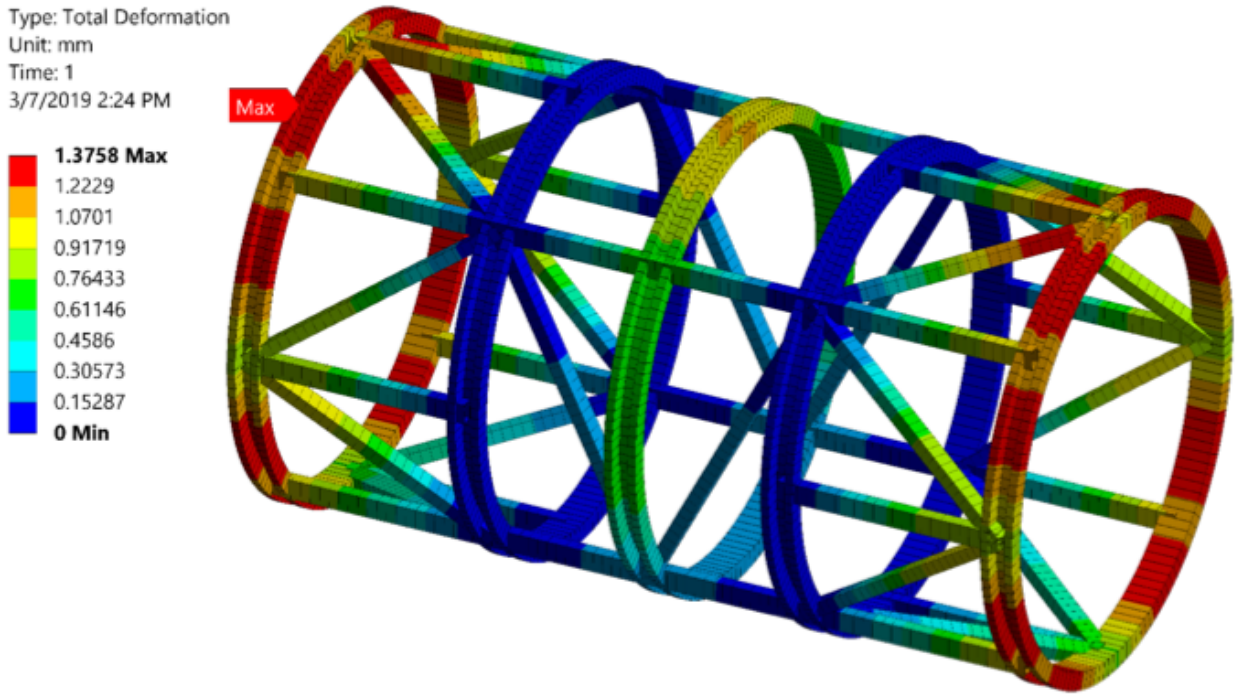


Figure A.24: Helmholz coil arrangement for MPD superconducting magnet.

All five coils have the same inner radius of 3.5 m. The center and shielding coils are identical with the same number of ampere-turns. The side coils are placed at 2.5 m, the shielding coils at 6 m from the magnet center along z. The case where the shielding coils are at 5 m from the magnet center so that the magnet system would be the same width as the LAr detector is also being examined. The magnet system will have a stored energy of about 110 MJ, using a conventional NbTi superconducting cable design, a SSC-type Rutherford cable soldered in a copper channel with a 50% margin. All coils should be wired in series to reduce imbalanced forces during a possible quench. Small transverse centering force components are possible due to coil de-centering from mechanical errors. Shown in Figure A.25 is the field along the z-axis at different radii. The peak field in the coils is 2.14 T (center), 5 T (side) and 2.03 T (shield). The resulting forces are only along the z-axis, F_z is 0.0 MN (center), −6.81 MN (side) and 2.2 MN (shield). The fringe field at the shielding coil is rather large but can be reduced further; more studies will be needed. There is a preliminary mechanical support design. A first glimpse at the radiative heat load assumes a coil and support surface of 180 m^2, resulting in a load of 5.4 W from 77 K to 4.5 K. The coil support and leads will likely have a much larger contribution (power leads usually have 15 W for 10 kA). With a mass of 42 t the magnets are in some aspects similar to the Mu2e solenoids.

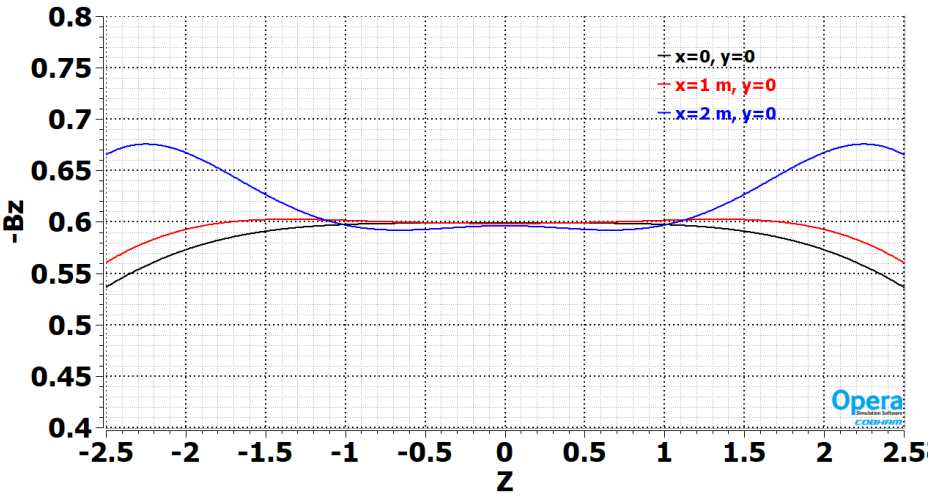


Figure A.25: Field map of the superconducting magnet along the z axis. The colors represent different radii from the center line.

Normal Conducting Magnet Although the SC magnet design is the favored option, the normal conducting magnet design produced for the LBNE CDR is also being revised and studied. Due to the cylindrical geometry imposed by the HPgTPC, a cylindrical coil design for the normal conducting magnet is the baseline. The cooling requirement of the coil is approximately 3.5 MW and involves a substantial cooling water flow. A thermal shield between the coils and the detector volume is required in order to minimize heat flow to the HPgTPC and the ECAL. The coil thickness becomes excessive (in order to maintain a maximum 5° C temperature in the coil) if the thermal shield is not used. The shield does take up space in the magnet volume, however. Note: the iron end-walls will most likely not be needed. The estimated magnet weight is well over 1 kt, and this mass provides a significant source of background for the high pressure gas TPC and, perhaps, the LAr. There is a significant amount of material between the LArTPC and the HPgTPC in the MPD in this configuration, which will affect the acceptance for muons emanating from events in the LAr. This option will continue to be studied as part of the optimization process.

A.5.3.1.4 Size optimization

The process of optimizing the design of the MPD is in progress. One of the more critical issues is the size of the MPD. This is an important factor in the angular acceptance of particles exiting the upstream LArTPC. A preliminary study of geometries shows that reducing the HPgTPC diameter by more than 1 meter, or reducing the length by more than 1.5 meters would have significant consequences on the acceptance. Reducing the HPgTPC diameter from its nominal 5 meters to a slightly smaller 4.5 meters while increasing its length in the direction transverse to the neutrino beam improves acceptance, since the HPgTPC would better match the 7-meter width of the LArTPC in the transverse direction. It should be noted, however, that reducing the diameter may actually result in a higher-cost MPD, since the ALICE TPC readout chambers would not be used in the configuration for which they were designed. Increasing the length of the HPgTPC is feasible, but will require additional studies of high voltage stability in the gas, since HV breakdown in gas is proportional to the pressure (in the absence of field enhancements). The HPgTPC operating pressure will be nominally 10 times that of ALICE, so extending the drift distance from 2.5 meters to 3 meters while keeping the same drift velocity will require raising the drift HV by approximately 20 kV.

A.5.3.2 MPD performance

The expected performance of the MPD is summarized in Table A.2. Details of the HPgTPC performance are based upon experience from operation of the PEP-4 [66, 67, 68] and ALICE [69] time projection chambers. Performance of the ECAL is based on experience from operation of similar ECALs and on simulations.

Table A.2: Expected MPD performance, extrapolated from ALICE

Parameter	Value	units
σ_x	250	μm
σ_y	250	μm
σ_z	1500	μm
$\sigma_{r\phi}$	$<$1000	μm
Two-track separation	1	cm
Angular resolution	2-4	mrad
$\sigma(dE/dx)$	5	%
σ_{p_T}/p_T	0.7	% (10-1 GeV/c)
σ_{p_T}/p_T	1-2	% (1 GeV/c to 0.1 GeV/c)
Energy scale uncertainty	$\lesssim 1$	% (dominated by δ_p/p)
Charged particle detection thresh.	5	MeV (K.E.)
ECAL energy resolution	5-7/$\sqrt{E/\mathrm{GeV}}$	%
ECAL pointing resolution	$\simeq 6$ at 500 MeV	degrees

A.5.3.2.1 Track Reconstruction and Particle Identification

The combination of very high resolution magnetic analysis and superb particle identification from the HPgTPC, coupled with a high-performance ECAL will lead to excellent event reconstruction capabilities and potent tools to use in neutrino event analysis. As an example of this capability, the top panel of Figure A.26 shows a $\nu_e + {}^{(N)}Ar \rightarrow e^- + \pi^+ + n + {}^{(N-1)}Ar$ in the HPgTPC with automatically-reconstructed tracks. The same event was simulated in a FD SP module, and is shown in the bottom panel of Figure A.26.

Since important components of the hardware and design for the HPgTPC are taken from or duplicated from the ALICE detector, the ALICE reconstruction is a useful point of reference in this discussion. Track reconstruction in ALICE is achieved by combining hits recorded on the ROC pads into tracks following a trajectory that a charged particle traveled through the TPC drift volume. The HPgTPC is oriented so that the neutrino beam is perpendicular to the magnetic field, which is the most favorable orientation for measuring charged particles traveling along the neutrino beam direction.

The GArSoft simulation and reconstruction package borrows heavily from LArTPC, and is based on the *art* event processing framework and `GEANT4`. It is designed to be able to reconstruct tracks with a full 4π acceptance. GArSoft simulates a 10 atmosphere gaseous argon detector with readout chambers filling in the central holes in the ALICE geometry. GArSoft's tracking efficiency has been evaluated in a large sample of GENIE ν_μ events interacting in the TPC gas at least 40 cm from the edges, generated using the optimized LBNF forward horn current beam spectra. The efficiency for reconstructing tracks associated with pions and muons as a function of track momentum p is shown in Figure A.27. The efficiency is above 90% for tracks with $p > 40$ MeV/c, and it steadily rises with increasing momentum.

Also shown is the efficiency for reconstructing all charged particles with $p > 200\,\mathrm{MeV/c}$ as a function of λ, the track angle with respect to the center plane. The tracking efficiency for protons is shown in Figure A.28 as a function of kinetic energy, T_p. Currently, the tracking works well down to $T_p \simeq 20\,\mathrm{MeV}$. For $T_p < 20\,\mathrm{MeV}$, a machine-learning algorithm is in development, targeting short tracks near the primary vertex. This algorithm, although currently in a very early stage of development, is already showing good performance, and efficiency improvements are expected with more development. The machine learning algorithm is described in Section A.5.3.2.3.

The ALICE detector, as it runs at the LHC, typically operates with particle densities ranging from 2000 to 8000 charged particles per unit rapidity (dN/dy) for central Pb-Pb interactions [70]. The expected particle densities in the DUNE neutrino beam will be much lower and less of a challenge for the reconstruction.

ALICE chose to use neon, rather than argon, for the primary gas in their first run; the decision was driven by a number of factors, but two-track separation capability was one of the primary motivations due to the extremely high track multiplicities in the experiment. Neon performs better than argon in this regard. A better comparison for the HPgTPC's operation in DUNE is the two-track separation that was obtained in PEP4 [67]. PEP4 ran an 80-20 mixture of Ar-CH_4 at 8.5 atmospheres, yielding a two-track separation performance of 1 cm.

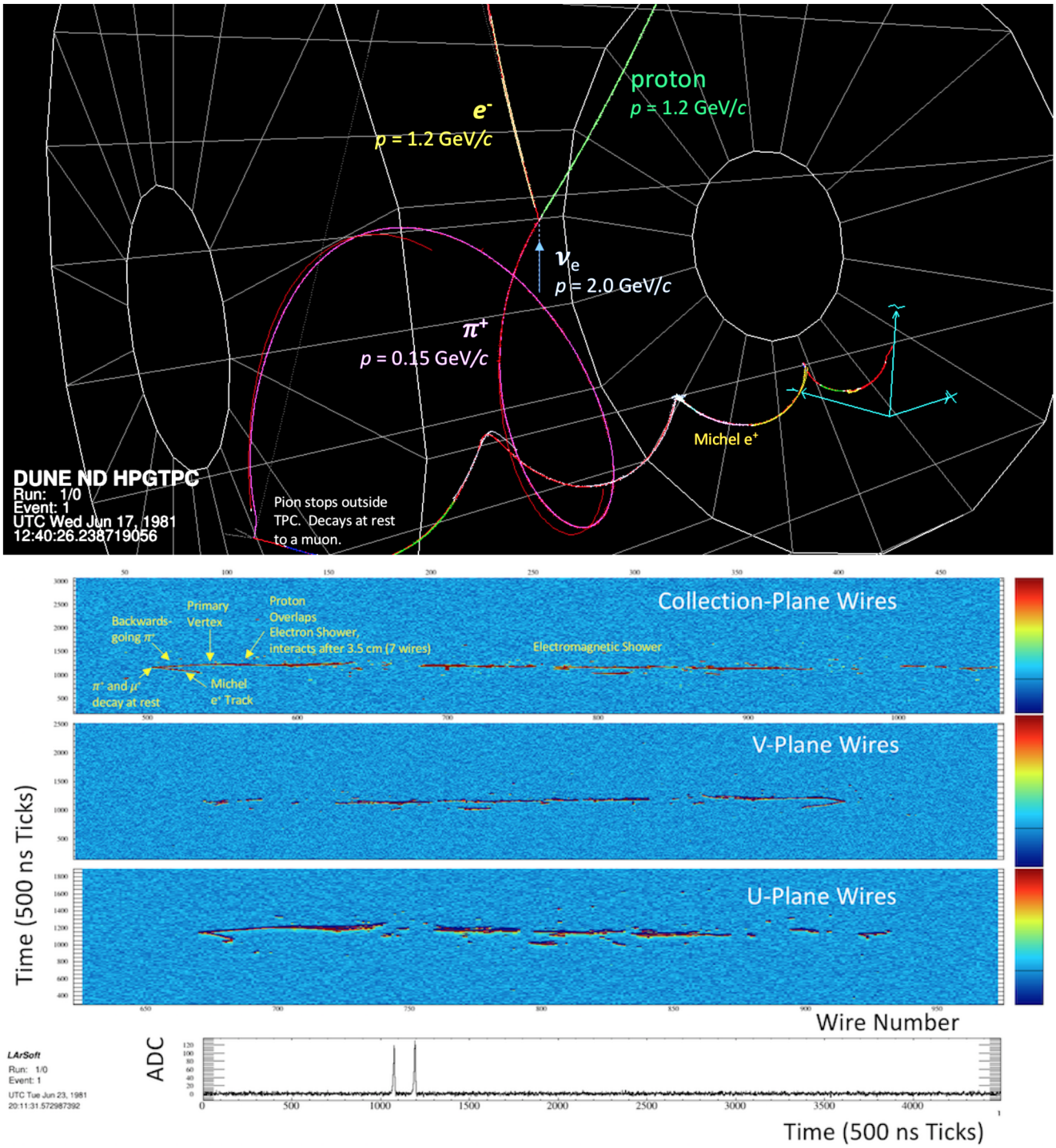


Figure A.26: (Top) Track-reconstructed ν_e CC event in the HPgTPC, simulated and reconstructed with GArSoft. The annotations are from Monte Carlo (MC) truth. (Bottom) The same ν_e CC event, but simulated in a SP module using Liquid Argon Software (LArSoft). The topmost blue panel shows the collection-plane view, the middle blue panel shows the V view, and the bottom blue panel shows the U view. Wire number increases on the horizontal axes and sample time along the vertical axes. The wire number in the collection view is labeled on the top of the panel, while the V and U wire numbers are below their respective panels. Simulated analog-to-digital converter (ADC) values are indicated by the colors. The curve in the bottom-most panel is a simulated waveform from a collection-plane wire. The annotations are from MC truth.

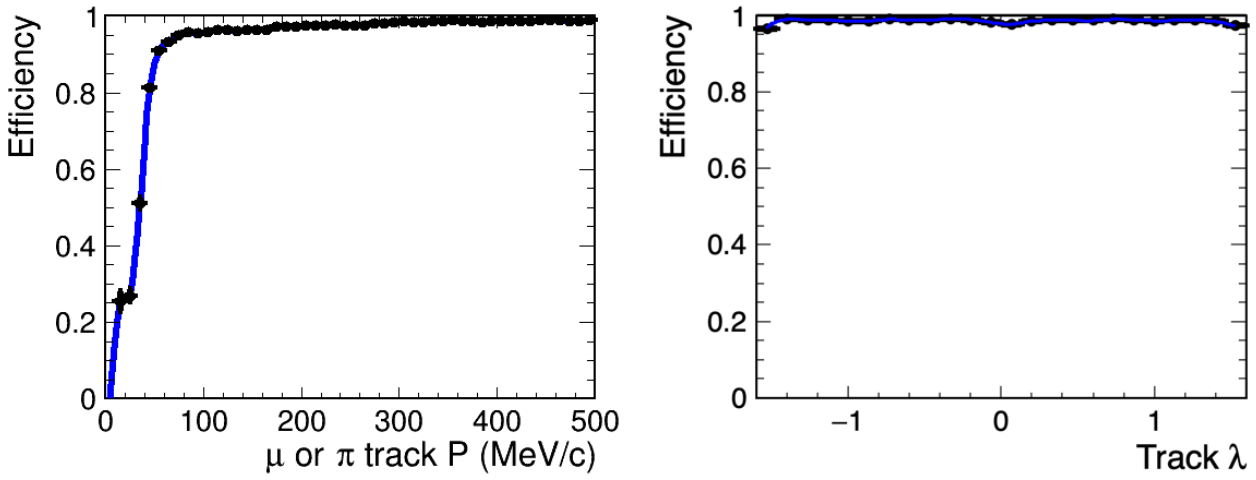


Figure A.27: (Left) The efficiency to find tracks in the HPgTPC as a function of momentum, p, for tracks in a sample of GENIE events simulating 2 GeV and ν_μ interactions in the gas, using GArSoft. (Right) The efficiency to find tracks as a function of λ, the angle with respect to the center plane, for tracks with $p > 200\,\text{MeV}/c$.

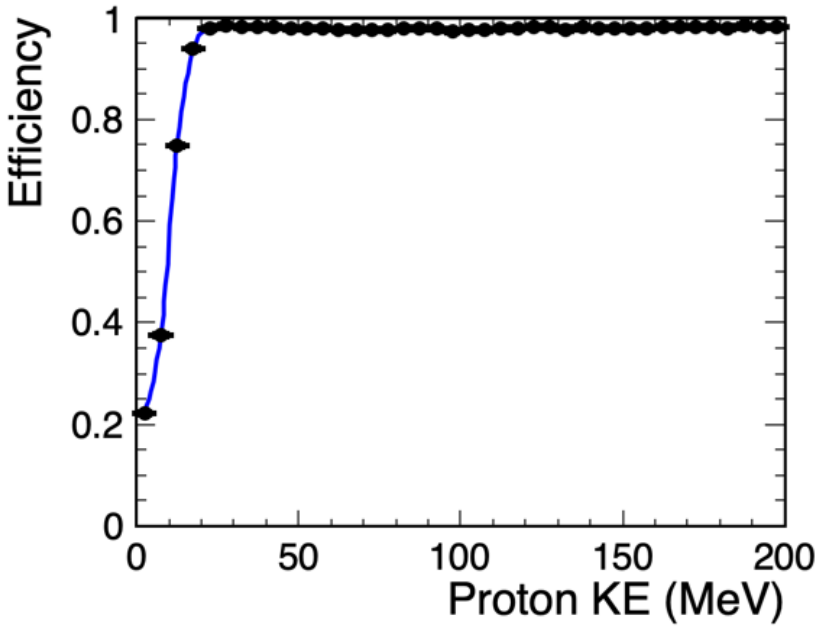


Figure A.28: Tracking efficiency for protons in the HPgTPC as a function of kinetic energy.

In ALICE, the ionization produced by charged particle tracks is sampled by the TPC pad rows (there are 159 pad rows in the TPC) and a truncated mean is used for the calculation of the PID signal. Figure A.29 (left) shows the ionization signals of charged particle tracks in ALICE for pp collisions at $\sqrt{s} = 7$ TeV. The different characteristic bands for various particles are clearly visible and distinct at momenta below a few GeV. When repurposing ALICE as the HPgTPC component of the MPD, better performance is expected for particles leaving the active volume, since the detector will be operating at higher pressure (10 atmospheres vs. the nominal ALICE 1 atmosphere operation), resulting in ten times more ionization per unit track length available for collection. Figure A.29 (right) shows the charged particle identification for PEP-4/9 [71], a higher pressure gas TPC that operated at 8.5 atmospheres, which is very close to the baseline argon gas mixture and pressure of the DUNE HPgTPC.

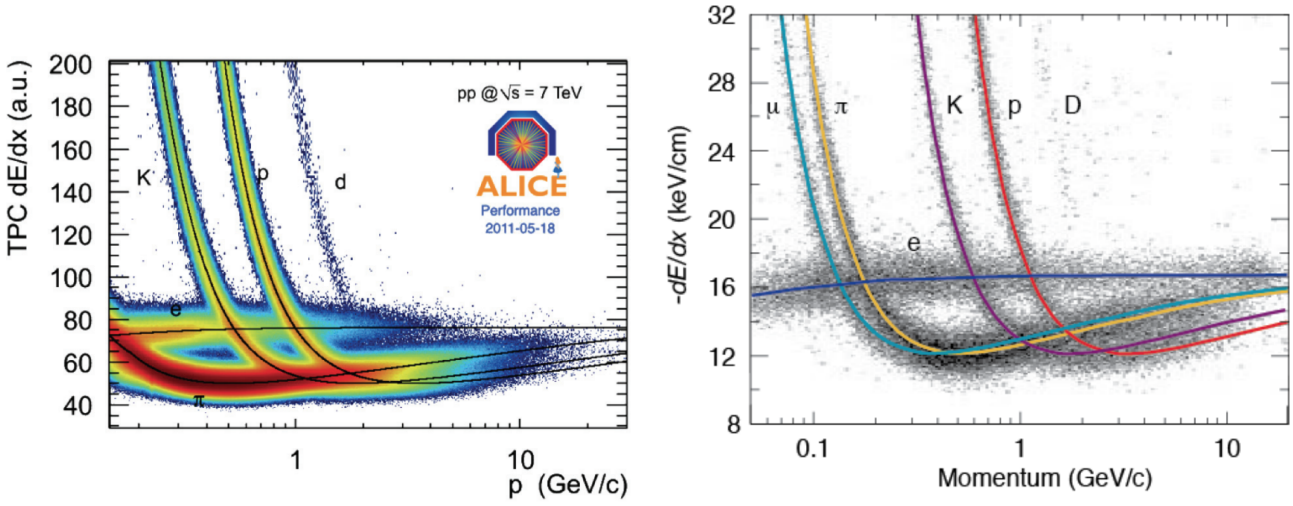


Figure A.29: Left: ALICE TPC dE/dx-based particle identification as a function of momentum (from [72]). Right: PEP-4/9 TPC (80:20 Ar-CH4, operated at 8.5 Atm, from [71]) dE/dx-based particle identification.

A.5.3.2.2 Momentum and Angular Resolution for Charged Particles

The ability to determine the sign of the charge of a particle in the HPgTPC tracking volume is limited by the spatial resolution of the measured drift points in the plane perpendicular to the magnetic field, as well as multiple Coulomb scattering (MCS) in the gas. For a fixed detector configuration, the visibility of the curvature depends on the particle's p_{T}, its track length in the plane perpendicular to the field, and the number and proximity of nearby tracks. Because primary vertices are distributed throughout the tracking volume, the distribution of the lengths of charged-particle tracks is expected to start at very short tracks, unless sufficient FV cuts are made to ensure enough active volume remains to determine particle's track sign. The kinetic energies of particles that leave short tracks and stop in the detector will be better measured from their tracks' lengths than from their curvatures. Protons generally stop before their tracks curl around, but low-energy electrons loop many times before coming to rest in the gas.

Within the FV of the HPgTPC, charged particles can be tracked over the full 4π solid angle. Even near the central electrode, tracking performance will not be degraded due to the very thin

(25 μm of mylar) nature of the central electrode. Indeed, tracks crossing the cathode provide an independent measurement of the event time, since the portions of the track on either side of the cathode will only line up with a correct event time assumed when computing drift distances. The 4π coverage is true for all charged particles. ALICE ran with a central field of 0.5 T and their momentum resolution from p–Pb data [73] is shown in Figure A.30.

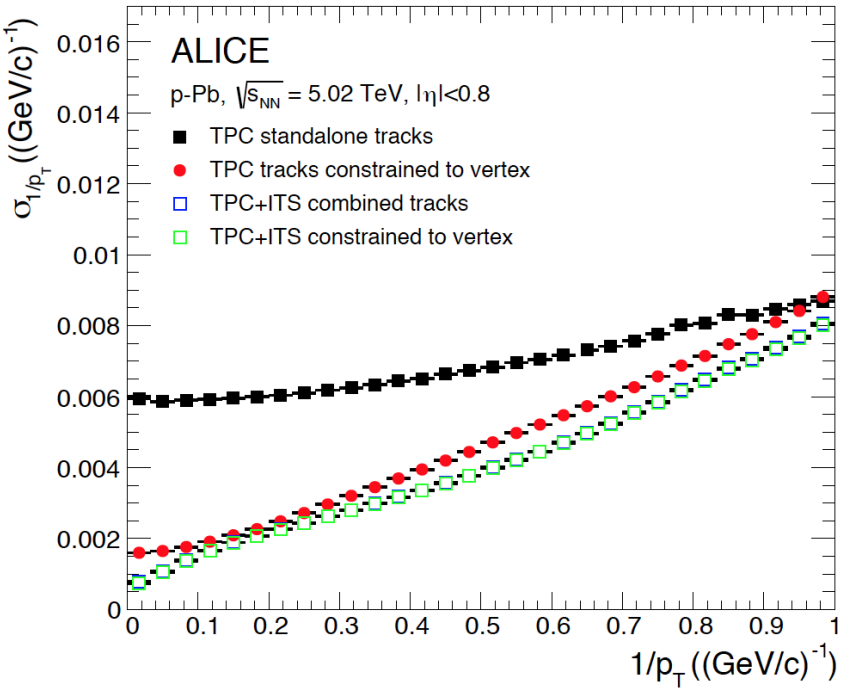


Figure A.30: The black squares show the TPC stand-alone p_T resolution in ALICE for p–Pb collisions. From Ref. [73].

The momentum resolution of muons in neutrino scatters using the GArSoft simulation and reconstruction package is shown in Figure A.31, using a sample of 2 GeV ν_μ CC events. This resolution differs from ALICE's achieved resolution due to the higher pressure, the heavier argon nucleus compared with neon, the non-centrality of muons produced throughout the detector, and the fact that the GArSoft simulation and reconstruction tools have yet to be fully optimized. The momentum resolution achieved for muons is $\Delta p/p = 4.2\%$, and is expected to improve with optimization of the simulation and reconstruction tools. The 3D angular resolution of muons is approximately 0.8 degrees, as shown in Figure A.31.

A.5.3.2.3 Machine Learning for Low Energy Protons

As a complement to the existing reconstruction, an initial exploration of several machine learning methods has been performed. The main goal of this effort has been to attempt to reconstruct very low energy protons and pions where traditional tracking methods might struggle. While this study is still in very early stages, there has been success so far in using a fully connected multi-layer perceptron (MLP) to both regress the kinetic energy of and classify between protons and pions. Additionally a Random Sample Consensus (RANSAC) based clustering algorithm has been

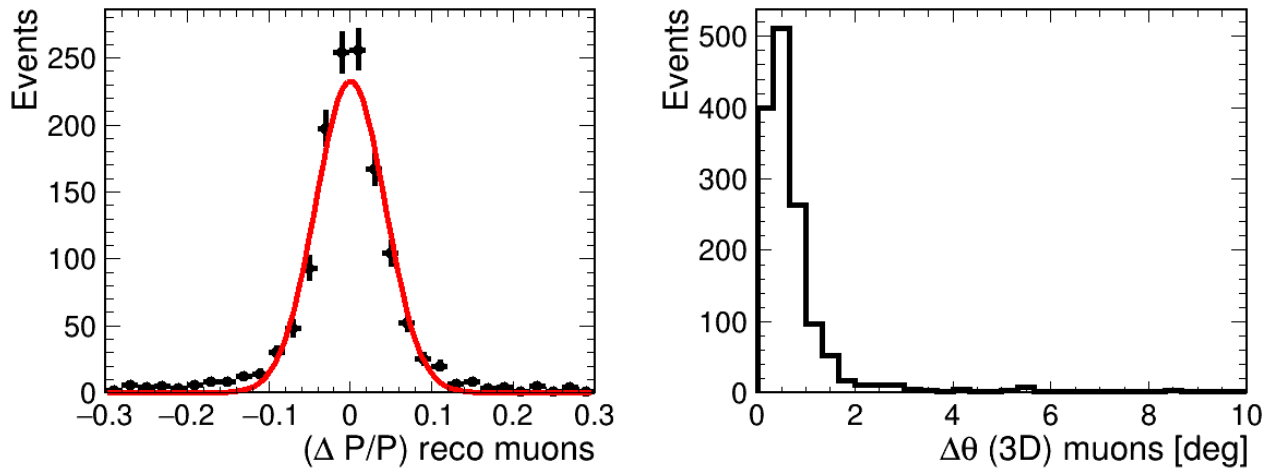


Figure A.31: Left: the momentum resolution for reconstructed muons in GArSoft, in a sample of 2 GeV ν_μ CC events simulated with GENIE. The Gaussian fit to the $\Delta p/p$ distribution has a width of 4.2%. Right: the 3D angular resolution for the same sample of muons in GArSoft.

developed to group hits into short tracks for events where there are multiple particles. Together, these two algorithms can be used to measure the kinetic energy of multiple particles in a single event.

As a demonstration, a test sample of multiple proton events was generated where each event has:

- 0-4 protons, number determined randomly with equal probabilities
- all protons share a common starting point (vertex) whose position in the TPC is randomly determined
- each proton is assigned independently and randomly:
  - a direction in space (isotropically distributed)
  - a scalar momentum between 0 and 200 MeV/c (flat distributed)

The RANSAC-based clustering algorithm assigns individual hits to proton candidate sets of hits which are passed to a MLP that was trained on a set of individual proton events in the TPC to predict kinetic energy. Figure A.32 shows the kinetic energy residuals, the reconstruction efficiency, and a 2D scatter plot of the measured kinetic energy versus the true kinetic energy for each individual proton with kinetic energy between 3 and 15 MeV in the test sample. Additionally, the residual for the total kinetic energy in each multi-proton event is given.

A.5.3.2.4 ECAL Performance

The expected performance of the calorimeter was studied with Geant4-based [74] simulations and GArSoft [75]. In the following, a first scenario referred to as scenario A (shown by the red curve in the figures below) in which the ECAL is located inside the pressure vessel is considered. The

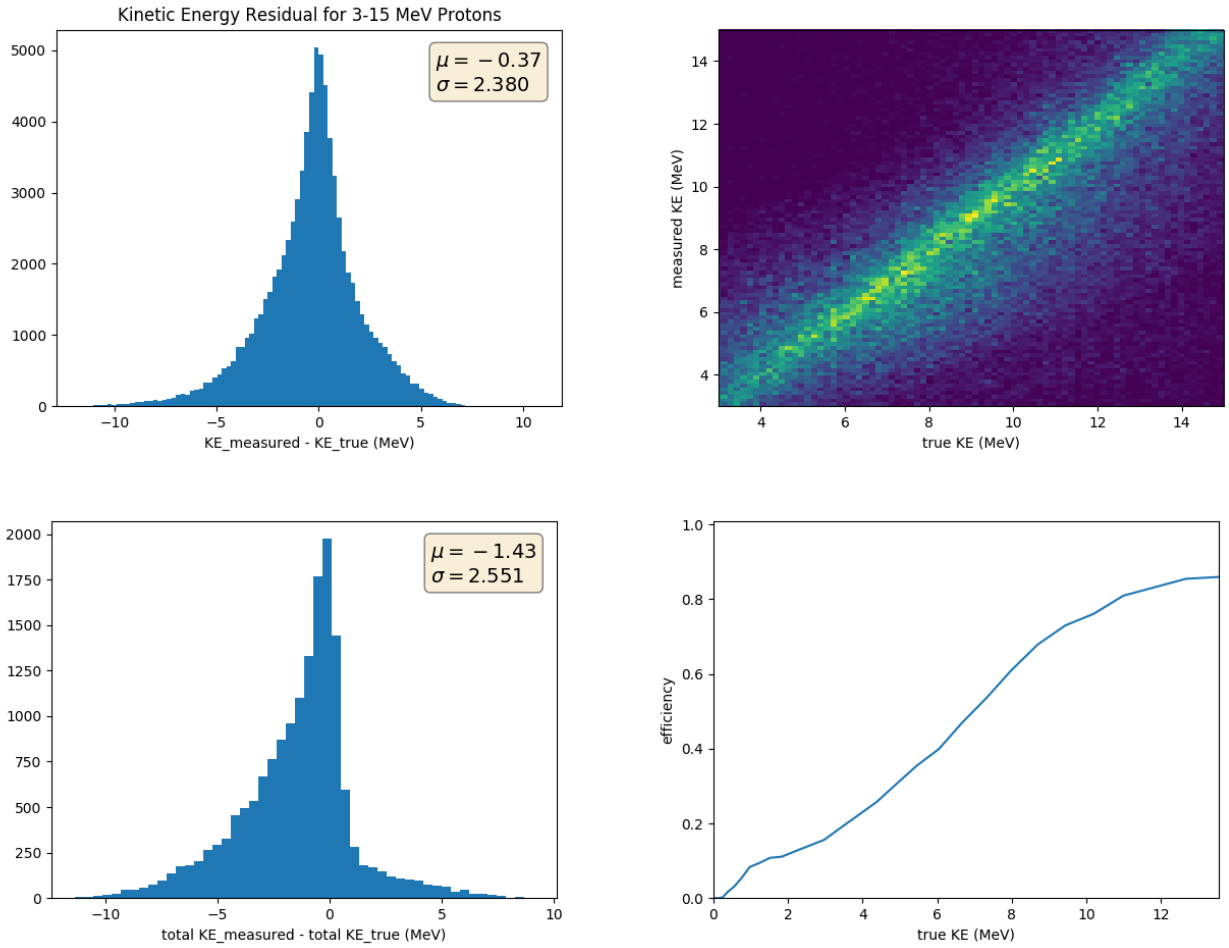


Figure A.32: (Top left) Kinetic energy residual, (Top right) measured KE vs. true KE, and (Bottom right) reconstruction efficiency for individual protons with 3 MeV to 15 MeV KE in the test set. (Bottom left) Residual of the total kinetic energy of all protons in each event in the test sample.

barrel geometry consists of 55 layers with the following layout:

- 8 layers of 2 mm copper + 10 mm of 2.5×2.5 cm^2 tiles + 1 mm FR4
- 47 layers of 4 mm copper + 10 mm of cross-strips 4 cm wide

For the present studies, copper has been chosen as absorber material as initial studies have shown that this material provides a good compromise between calorimeter compactness, energy resolution, and angular resolution. However, the choice of absorber material is still under study. The choice of granularity, scintillator thickness, and the arrangement of tiles and strips is still under optimization in order to reduce the number of readout channels while keeping the calorimeter performance. Two alternative scenarios are shown below: scenario B (black curve) has a different arrangement of the tile and strip layers, and scenario C (blue curve) has thinner absorbers in the front layers. Digitization effects are accounted for by introducing an energy threshold of 0.25 MIPs (∼200 keV) for each detector cell/strip, a Gaussian smearing of 0.1 MeV for the electronic noise, SiPM saturation effects, and single photon statistics.

Energy Resolution The energy resolution is determined by fitting the visible energy with a Gaussian. Converted photons are rejected based on Monte-Carlo information. A fit function of the form $\frac{\sigma_E}{E} = \frac{A}{\sqrt{E}} \oplus \frac{B}{E} \oplus C$ is used, where A denotes the stochastic term, B the noise term, C the constant term, and E is in GeV. Figure A.33 shows the energy resolution as a function of the photon energy. For scenario A, shown in red, the energy resolution is around $\frac{6.7\%}{\sqrt{E}}$. With further optimization, it is believed that an energy resolution of (or below) $\frac{6\%}{\sqrt{E}}$ is achievable. It should be noted that due to the lack of non-uniformities, dead cells, and other effects in the simulation, the energy resolution is slightly optimistic.

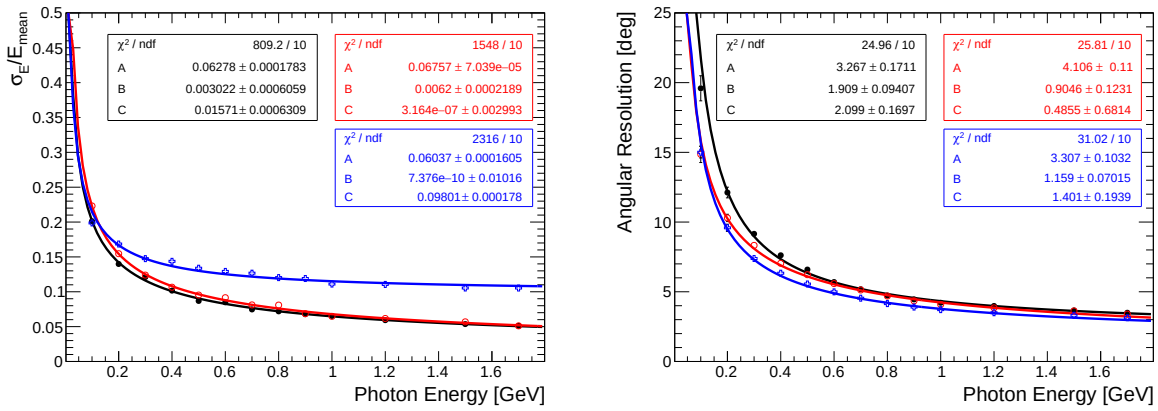


Figure A.33: Left: energy resolution in the barrel as a function of the photon energy for three ECAL scenarios. The energy resolution is determined by a Gaussian fit to the visible energy. Right: the angular resolution in the barrel as a function of the photon energy for the three ECAL scenarios. The angular resolution is determined by a Gaussian fit to the 68% quantile distribution. For both figures, the scenario A is shown by the red curve, scenario B by the black curve and scenario C by the blue curve. The fit function is of the form $\frac{\sigma_E}{E} = \frac{A}{\sqrt{E}} \oplus \frac{B}{E} \oplus C$.

Angular Resolution The angular resolution of the calorimeter has been determined using a principal component analysis (PCA) of all reconstructed calorimeter hits. The direction is taken as the first eigenvector (main axis) of all the reconstructed hits. The angular resolution is determined by taking the 68% quantile of the reconstructed angle distribution and fitting a Gaussian distribution. The mean of the Gaussian is taken as the angular resolution and the error as its variance. Figure A.33 shows the angular resolution as a function of the photon energy. In scenario A, shown in red, an angular resolution of $\frac{3.85^\circ}{\sqrt{E}} \oplus 2.12^\circ$ can be achieved. This can potentially be further improved with a different arrangement of the tile and strip layers, an optimization of the absorber thickness, and an improved reconstruction method. However, the requirements will be further refined and will impact the detector optimization. The angular resolution is mainly driven by the energy deposits in the first layers of the ECAL. Using an absorber with a large X_0 creates an elongated shower that helps in determining the direction of the shower. In general, high granularity leads to a better angular resolution, however, studies have shown that there is no additional benefit to having cell sizes below 2×2 cm^2 [65].

Neutron detection The ECAL is sensitive to neutrons due to the scintillator containing hydrogen. Previous simulation studies showed that a detection efficiency above 60% can be achieved for neutron energies greater than 50 MeV. However, the energy measurement is not very accurate (around 50-60% below 600 MeV) [65]. Other methods of detection such as time of flight (ToF) could be used to improve the neutron energy measurement by measuring precisely the hit time of the neutron and its travel distance in the calorimeter. This is currently under study.

π^0 reconstruction For identification of neutral pions, both the energy and angular resolution are relevant. In an initial study, the position of the neutral pion is determined by using a χ^2-minimization procedure taking into account the reconstructed energy of the two photons and the reconstructed direction of the photon showers [65]. The location of the decay vertex of the neutral pion can be determined with an accuracy between 10 cm to 40 cm, depending on the distance from the downstream calorimeter and the π^0 kinetic energy. This is sufficient to associate the π^0 to an interaction in the HPgTPC, since the gas will have less than one neutrino interaction per beam spill. The pointing accuracy to the pion decay vertex may be further improved by a more sophisticated analysis technique and by using precision timing information, and is a subject of current study.

A.5.4 The DUNE-PRISM Program

The goals of the off-axis measurements are twofold:

- **To identify problems in the cross section modeling.** By comparing ND data to MC at many off-axis locations with different energy spectra, the neutrino interaction model will be more tightly constrained than it would be with only on-axis measurements, and the potential for biases in the measured oscillation parameters can be identified, i.e., the off-axis data might be sensitive to mismodelings that are degenerate or indeterminate with only on-axis

measurements.

- **To overcome problems in the cross section modeling.** The most important novel feature of a DUNE-PRISM detector is that measurements at different off-axis positions can be linearly combined to determine any set of observables for any user-defined neutrino energy spectrum. In particular, it is possible to predict the expected distribution of an observable, such as the reconstructed neutrino energy, for a neutrino flux with oscillations using linear combinations of ND off-axis spectra. This will greatly reduce the dependence on neutrino interaction modeling within the oscillation analysis.

A.5.4.1 Impact of Cross Section Modeling on Neutrino Oscillations

One strategy to understand the potential impact of using imperfect neutrino interaction models is to extract oscillation parameters from a "fake" data set that is different from the model used in the analysis. This fake data set represents a reality that includes effects unknown to or not accounted for properly by the model used in the analysis to fit the data. In this way, it is possible to understand potential biases in the measured oscillation parameter values extracted from a full near+far detector fit due to the use of an incorrect cross section model in the fit.

The fake data set considered here assumes that 20% of the kinetic energy that the interaction model originally assigned to protons was instead carried away by neutrons. The resulting model is then further modified by adjusting the differential cross section in proton energy as a function of true neutrino energy until the measured kinematic distributions in the on-axis ND match the prediction from the default model. This procedure is similar to actions that are routinely taken in actual neutrino oscillation experiments to resolved discrepancies between ND data and the Monte Carlo simulation. There are many potential modifications to the cross section model that can be chosen to resolve such disagreements. Incorrect choices can lead to biased oscillation parameter measurements because the associated incorrect particle composition and cross section model can lead to an incorrect relation between reconstructed and true energy.

The resulting fake data is analyzed as though it were the actual data taken by the experiment. The ND and FD data are fit simultaneously to constrain nuisance parameters in the flux and cross section models, and to extract the measured value of the neutrino oscillation parameters. The results of this fit are shown in Figure A.34. The fit to the fake data shows a clear bias in the measured oscillation parameter values that lie outside the 95% confidence limit contours.

A comparison of the fake data and the nominal Monte Carlo reconstruction energy distributions is shown in Figure A.35. In the on-axis location, good agreement is seen, as was intended in the construction of the fake data samples. This good agreement is assured since the model is tuned to the on-axis data. Conversely, clear disagreement is seen between these samples when moving off-axis. As the off-axis location is varied, this comparison can be made across a wide range of neutrino energy distributions.

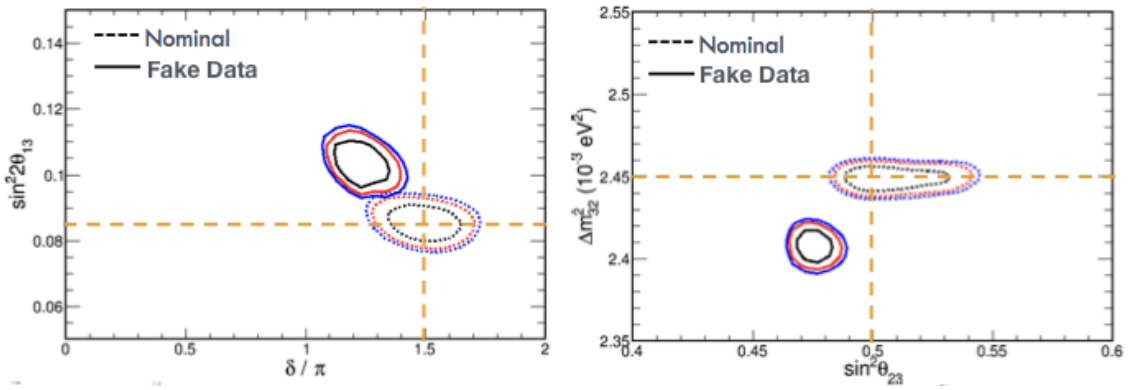


Figure A.34: The results of a full two-flavor, antineutrino+neutrino, near+far oscillation fit are shown for a fit to the nominal MC (dashed) and a fit to the fake data set (solid). The true values of the oscillation parameters in each of the data sets are indicated by the dashed yellow lines. Clear biases can be see in all oscillation parameters that are well outside the 1σ (black), 2σ (red), and 3σ (blue) contours.

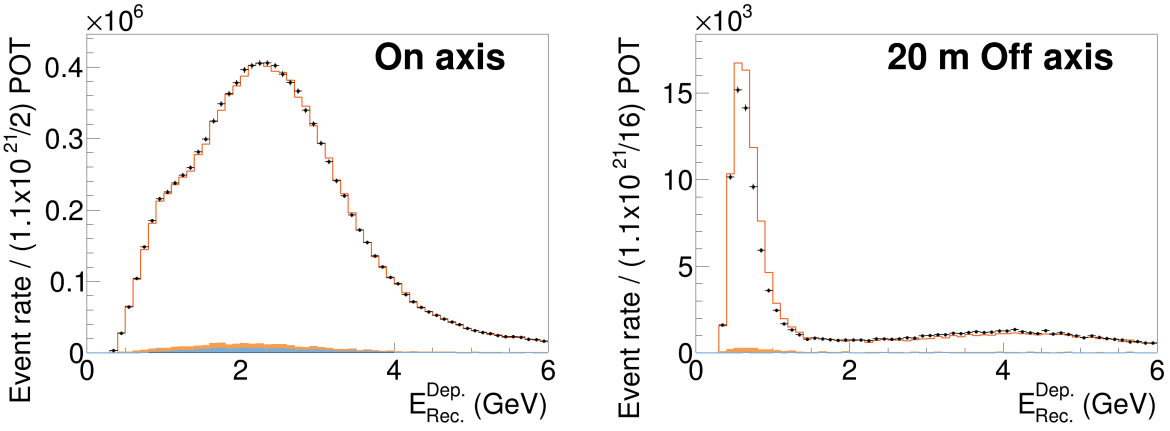


Figure A.35: A comparison between the fake data (green) and nominal Monte Carlo (red) reconstructed neutrino energy distributions are shown for the on-axis ND location (left) and a position 18 m off-axis (right).

A.5.4.2 DUNE-PRISM Linear Combination Analysis

In addition to identifying problems in cross section modeling, DUNE-PRISM measurements provide a mechanism for creating FD predictions directly from the ND data that is largely independent of neutrino interaction modeling. By constructing linear combinations of measurements taken under exposure to different neutrino fluxes, it is possible to determine the distribution of any observable (e.g. reconstructed neutrino energy) for a different neutrino flux of interest. This means, for example, from the ND data alone it is possible to create a distribution of the expected reconstructed neutrino energy distribution at the FD in the event of oscillations with a specific set of parameters. This distribution, created using this data-driven technique, can then be compared to that seen in the FD with a reduced dependence on the flux and neutrino interaction models and their associated uncertainties.

A few example fits of the off-axis ND muon neutrino spectra to an oscillated FD muon neutrino energy spectrum are shown in Figure A.36. Good agreement is seen near the first and second oscillation maxima at 2.5 GeV and 0.7 GeV, respectively. The ability to fit the FD spectrum breaks down outside the central range of energy because the constituent off-axis spectra used in the fit extend only slightly outside this range and cannot duplicate the spectrum in any combination. This does not pose a significant problem for the oscillation analysis because the fit is good for the bulk of the events and in the region that drives the CP sensitivity. This technique can also be applied to match the off-axis muon neutrino spectra to the ND intrinsic electron neutrino spectrum, in order to make a precise measurement of $\sigma(\nu_e)/\sigma(\nu_\mu)$ with a common flux, or to the FD oscillated electron neutrino energy spectra for the measurement of δ_{CP}.

A.6 Fixed On-axis Component of the DUNE ND

A.6.1 Motivation and Introduction

In spite of tremendous efforts to ensure stable operation, neutrino beams are dynamic in nature. Experiments must track changes in the beam as a function of time in order to understand and model the neutrino flux spectrum well enough to achieve their physics goals. In addition, neutrino interactions observed by experiments in the beam, if taken at a sufficient rate with good energy and spatial resolutions, can provide unique and invaluable information as a beam diagnostic. The issue of beam stability is particularly important for DUNE because the wide-band beam is sensitive to a large range of beamline changes and the DUNE-PRISM program makes use of spectral shifts induced by off-axis translation which must be distinguished from time-dependent neutrino spectral changes intrinsic to the beam. On-axis beam monitoring, in particular, is critical because the DUNE far detector sees that beam. The on-axis spectrum must be modeled and used for the extraction of the oscillation parameters at the far detector.

There are many valuable lessons for DUNE/LBNF in the NuMI experience. One of those lessons is that unexpected things happen to neutrino beamline elements that can take them well outside the typical error tolerance. One example of this at NuMI was degradation in the target due to

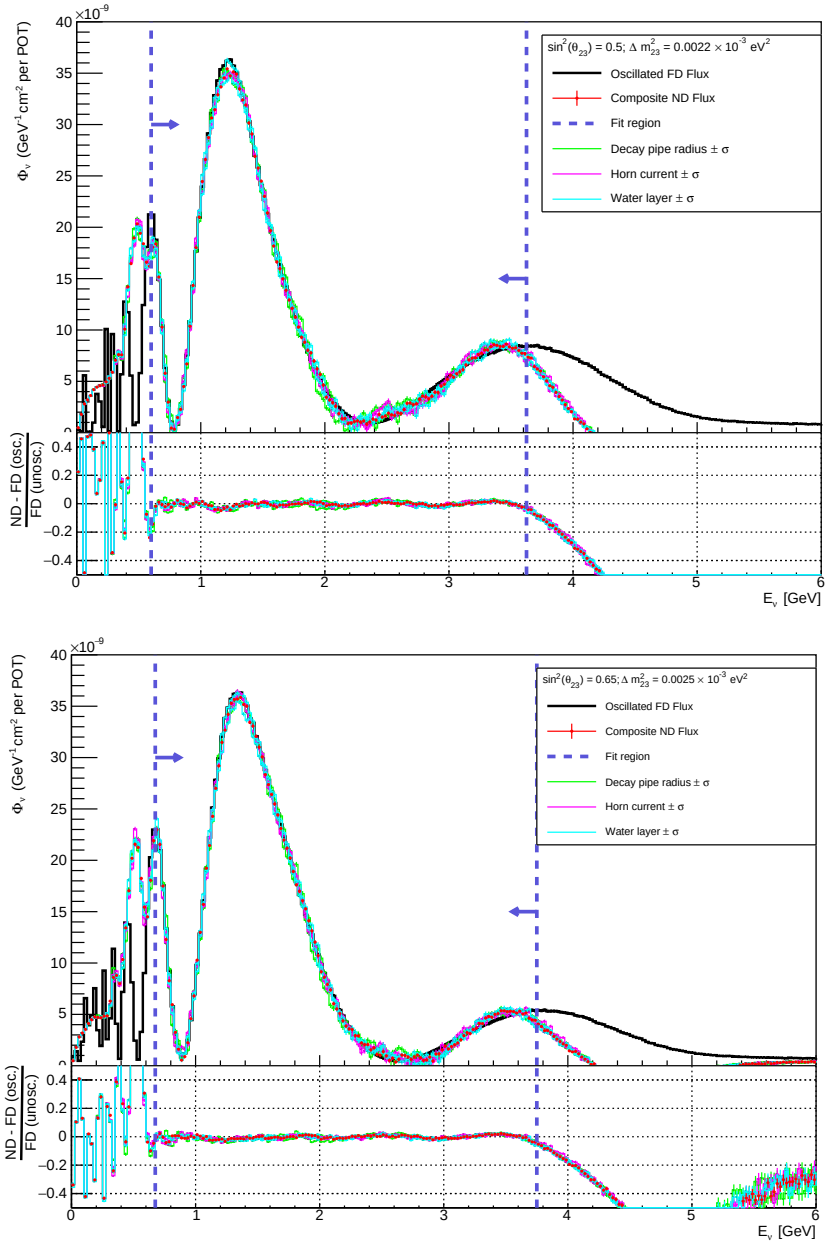


Figure A.36: Linear combinations of off-axis fluxes giving far-detector oscillated spectra for a range of oscillation parameters. The FD oscillated flux is shown in black, the target flux is shown in green, and the linearly combined flux obtained with the nominal beam MC is shown in red. Systematic effects due to 1 σ variations of the decay pipe radius (green), horn current (magenta) and horn cooling water layer thickness (teal) are shown.

broken upstream target fins. This was observed and diagnosed prior to target autopsy by the change in the observed near detector neutrino event spectrum [76]. Figure A.37 shows MINOS near detector data in bins of reconstructed neutrino event energy. Within each bin are points representing successive periods of the data taking run. A time-dependent shift in the three peak bins, i.e., a change in the spectral shape, is obvious in the plot. Another example of a significant and noticeable change in the beam spectra at NuMI was caused by magnetic horn tilt due to degradation of a supporting washer [77]. Yet another significant wiggle in the beam spectral shape has been observed in the MINERvA and NOvA medium energy run [9]. Notably, this wiggle is not as significant in the off-axis data taken by the NOvA near detector as it is for on-axis MINERvA. MINERvA studies indicate the observed spectral shift is best modeled by a shifted horn position or a slight change in the inner horn radius relative to the expected value.

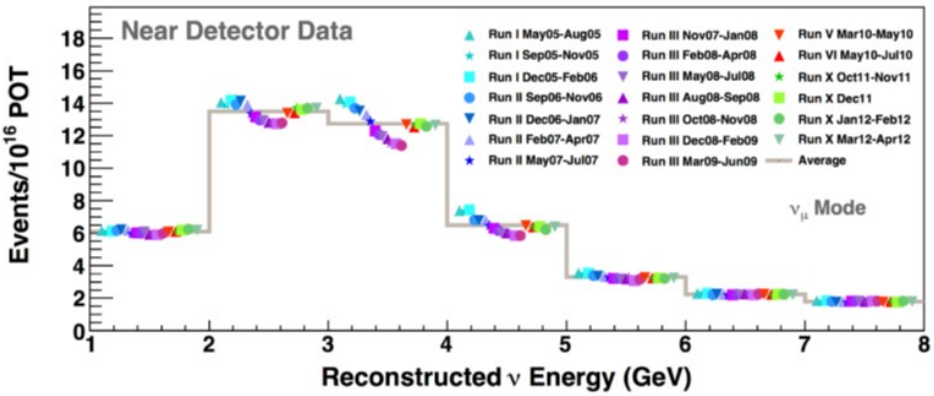


Figure A.37: The low energy run MINOS event rate as a function of neutrino energy broken down in time. From [76].

Given the past experience from NuMI, it is thought to be critically important that the DUNE ND monitor and track the beam spectrum over time. ArgonCube and the MPD will make on-axis neutrino beam spectrum measurements when they are located on-axis. There are two broadly different concepts under discussion for how to monitor the on-axis beam when ArgonCube and the MPD move off-axis as required by the DUNE-PRISM program. One concept is to have a dedicated on-axis beam monitor that is capable of measuring the neutrino beam spectrum as a function of time. Such a capability would require target mass and a magnet or range stack with tracking to measure the momentum of muons arising from CC ν_μ interactions. The other concept assumes a dedicated on-axis neutrino interaction rate monitor. Both the on-axis rate monitor and the off-axis spectrometer would each track beam stability. In the case of an observed instability of either the rate or the off-axis spectrum, ArgonCube and the MPD would move back on-axis to make a spectrum measurement. It is likely the DUNE-PRISM run plan would include intermittent on-axis measurements as well regardless of observed instabilities. Since the first concept involves a magnet or large range stack, it is likely to be more expensive to implement than the option that makes use of the dedicated rate monitor on-axis. On the other hand, the latter option with intermittent on-axis spectral measurements involves additional movements of the large, DUNE-PRISM detectors, precision comparison of spectral measurements separated in time with detectors that have moved in the interim, and accepting the risk that rate and off-axis spectral monitoring are both less sensitive to some changes in the beam than on-axis spectral monitoring. Figure A.38 provides an illustration, for a small subset of relevant beam parameters, of the differing sensitivities of integrated rate monitoring as compared to spectral monitoring of the beam. Additional studies

are in progress.

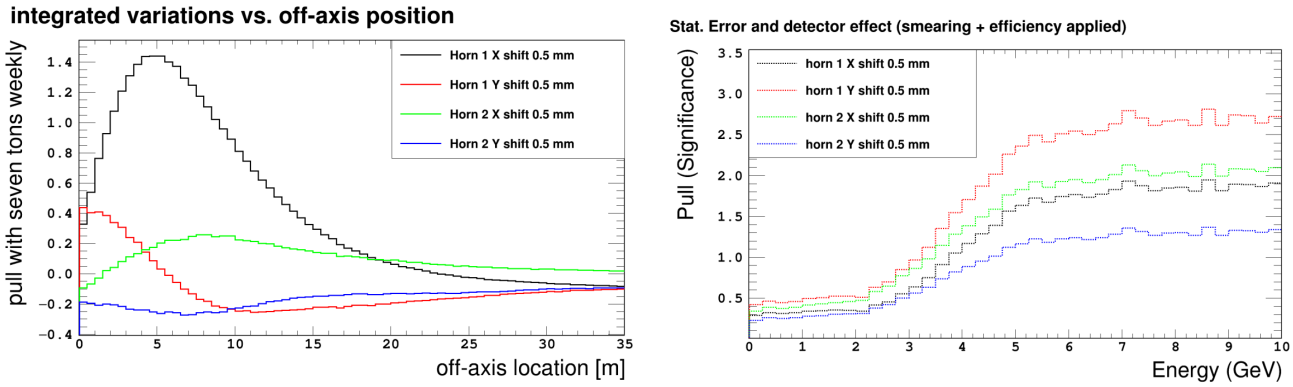


Figure A.38: Comparison of rate monitoring and spectral monitoring of the neutrino beam for 1-sigma shifts of the horn positions. On the left is shown the significance of the variation in the observed rate for one week of running with a seven ton fiducial mass detector. It is shown as a function of off-axis angle (including zero, i.e., on-axis). On the right is shown the significance of the shape change as a function of energy for one week of running with an 8.7 ton fiducial mass on-axis spectrometer.

The reference design described below in Section A.6.2 assumes the beam monitoring is done with a dedicated on-axis magnetic spectrometer. The device described is a capable beam monitor in that it has the required mass and muon momentum resolution as will be shown in Section A.6.2.4. In addition, the on-axis spectrometer described below has capabilities that go beyond beam monitoring, which are useful for building confidence in the flux model and providing information that is potentially useful for the evolution of the neutrino interaction model. Other concepts, including one that utilizes an on-axis rate monitor, are under consideration.

A.6.2 Three-Dimensional Projection Scintillator Tracker Spectrometer

SAND consists of an active target core of scintillator called the 3DST surrounded by TPCs and an ECAL in a 0.5 T magnetic field. This system has two main goals in the context of the larger ND complex. First, SAND functions as an on-axis, high mass target and muon spectrometer that is capable of producing a statistically significant neutrino beam spectrum measurement in a short period. This dedicated, on-axis beam monitoring will be important in light of the movement of ArgonCube and the MPD within the context of the DUNE-PRISM program. Second, the 3DST can measure neutrons on an event-by-event basis, including those at a lower neutron kinetic energy than those seen by the other components of the ND. The inclusion of neutrons in the event reconstruction on an event-by-event basis is a powerful new tool that can be used for flux measurements and to probe neutrino interaction physics and modeling.

The 3DST is a fully active plastic scintillator detector made up of optically isolated 1 cm^3 cubes [78]. The cubes are read out by wavelength shifting (WLS) fibers along 3 orthogonal axes providing three two-dimensional projections that yield effective three-dimensional reconstruction.

The 3DST is dense enough to provide a large statistics sample with reasonable containment of

hadrons and photons from neutrino interactions. The high statistics and granularity of the 3DST will allow for timely beam monitoring, flux determination via different methods (with charge separation), and the study of many different neutrino interaction morphologies. The sub-ns timing resolution provides the capability to include neutrons in the event reconstruction via Time-of-Flight (ToF) with a reasonably high efficiency.

To date, neutrino experiments have been largely blind to neutrons on an event-by-event basis. This is not ideal, in part because the neutron content of neutrino and antineutrino interactions differ, and in part because neutrons can carry a significant part of the outgoing energy and momentum of a neutrino interaction which compromises the reconstruction of events with missing neutrons. Preliminary studies show the 3DST is likely to be able to measure neutrons to a lower neutron KE (KE_n) than the other component detectors of the ND and pursue event-by-event analysis with fully reconstructed final state particles, including neutrons. The addition of neutrons in event reconstruction will open the avenue to improved single transverse variable analyses that are expected to yield an improved neutrino energy resolution for flux (particularly antineutrinos) determination and for studies that may aid the evolution of the neutrino interaction model.

The 3DST uses the same technology as the SuperFGD detector that is being constructed for the T2K ND upgrade [79]. The two detectors are functionally identical, though somewhat different in size. The SuperFGD will be installed 2021 and will act effectively as a prototype for the larger 3DST in the DUNE ND.

A.6.2.1 Detector Configuration

The 3DST detector concept is shown in Figure A.39. The scintillator composition is polystyrene doped with 1.5% of paraterphenyl (PTP) and 0.01% of POPOP. After fabrication, the scintillator surface of the cubes is etched with a chemical agent that results in the formation of a white, reflecting polystyrene micro-pore deposit over the scintillator. Three orthogonal through holes of 1.5 mm diameter are drilled in the cubes to accommodate WLS fibers. This novel geometry provides full angular coverage for particle produced in neutrino interactions. The momentum threshold for protons is about 300 MeV/c (if at least three hits are requested).

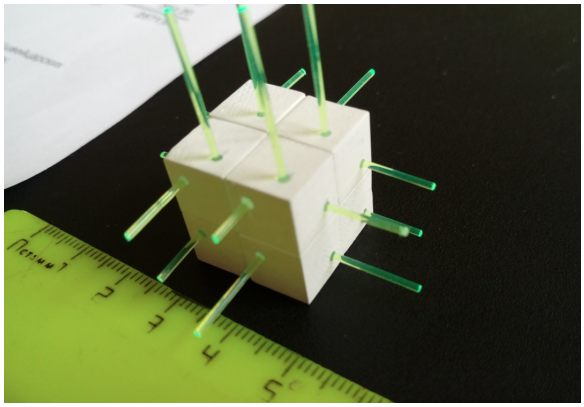


Figure A.39: A few plastic scintillator cubes assembled with wavelength-shifting (WLS) fibers.

The 3DST and surrounding elements are shown in Figure A.40. The size of the 3DST detector is

under discussion. Detectors of size 2.4×2.4×2.0 m^3, 3.0×2.0×2.0 m^3, and 2.0×2.0×2.0 m^3 have been used in different studies. The primary considerations that drive the size are space, statistics, and neutron containment.

The 3DST is surrounded by low mass trackers to measure the kinematics of charged particles produced but not stopping in 3DST, and an ECAL to identify and reconstruct photons and electrons exiting the 3DST. The trackers are TPCs in the reference design. Straw tube trackers are also under consideration. All the detectors will be immersed in a 0.5 T magnetic field provided by the KLOE magnet. The TPCs are envisioned to be similar to those being constructed for the T2K ND280 detector upgrade, described in [79]. They are approximately 80 cm thick and use a gas mixture of Ar-CF4-iC4H10 (95% - 3% - 2%).

The KLOE magnet and ECAL already exist and have been used successfully for many years in a running experiment. The work and infrastructure necessary to transport the devices to Fermilab, as well as to install and operate them in the ND hall are under study.

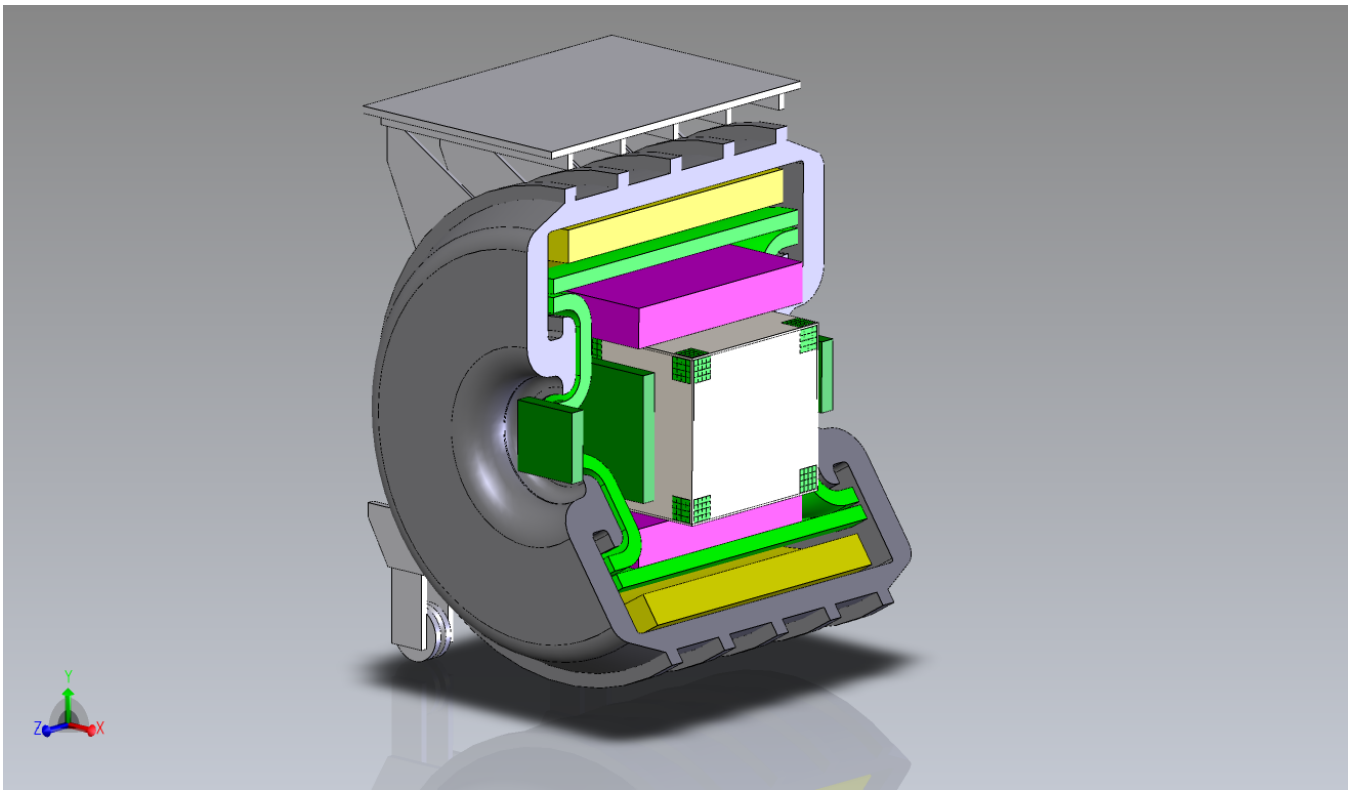


Figure A.40: The 3DST inside the KLOE magnet. The drawing shows the 3DST in the center (white), TPCs (orange), ECAL (green), magnet coil (yellow), and the return yoke (gray).

A.6.2.2 3DST Detector Performance

The performance of devices built on the 3DST concept have been tested in several test beams at CERN [80]. A small prototype of 5 × 5 × 5 cubes collected data in the T10 test-beam area at

CERN in 2017, with the goal of characterizing the response of the plastic scintillator cubes. The detector was instrumented with 75 WLS fibers (1 mm diameter Y11(200) Kuraray S-type of 1.3 m length). One end of the fiber was attached to a photosensor while the other end was covered by a reflective Al-based paint (Silvershine). The photosensors in the beam test were Hamamatsu MPPCs 12571-025C with a 1×1 mm^2 active area and 1600 pixels. The data were collected with a 16-channel CAEN digitizer DT5742 with 5 GHz sampling rate and 12-bit resolution.

The average light yield was about 40 p.e./MIP in a single fiber, and the total light yield from two fibers in the same cube was measured on an event-by-event basis to be about 80 p.e., as expected. The light cross-talk probability between a cube fired by a charged particle and a neighboring cube was studied. The light measured in the neighboring cube was about 3.4% of the light collected from the fired cube. The timing resolution for a single fiber was measured to be ∼0.95 ns. If the light of a cube is read out by two WLS fibers, the timing resolution becomes better than 0.7 ns and would improve further if the light collected by all the three WLS fibers is taken into account. In Figure A.41 the light yield and the time spectra obtained from two fibers reading out the light in the same cube are shown.

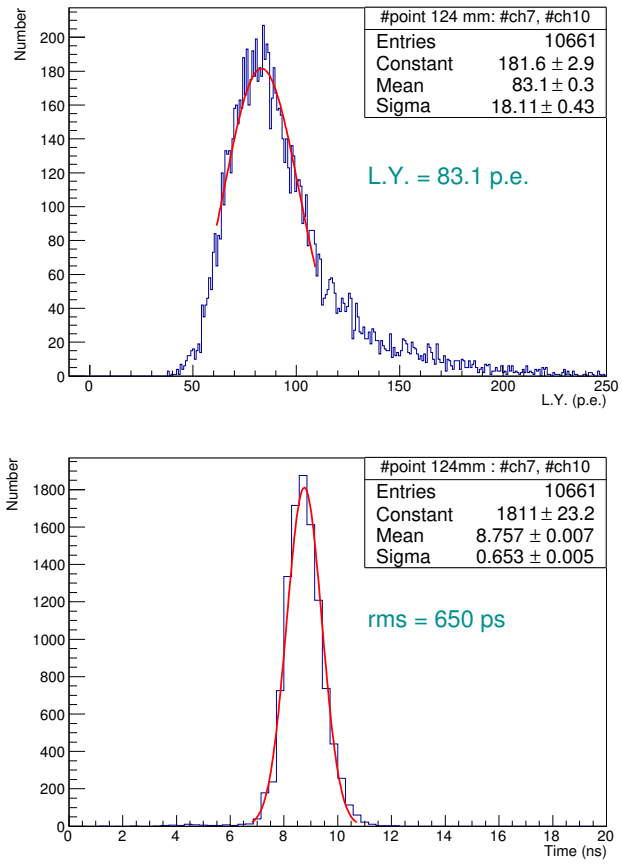


Figure A.41: Charge and time spectra for a single 3DST cube. Charge signal is a sum from two fibers, the time is an average time between two fibers.

In the summer of 2018, a prototype made of 9,216 cubes with a size of $8\times24\times48$ cm^3 collected data in the CERN T9 test-beam line. A different electronic readout was used, which was based on the CITIROC chip used in the Baby MIND experiment. Preliminary results confirmed the light

yield performances of the 2017 test-beam data. A more detailed analysis of the data is currently ongoing. Some event displays are shown in Figure A.42.

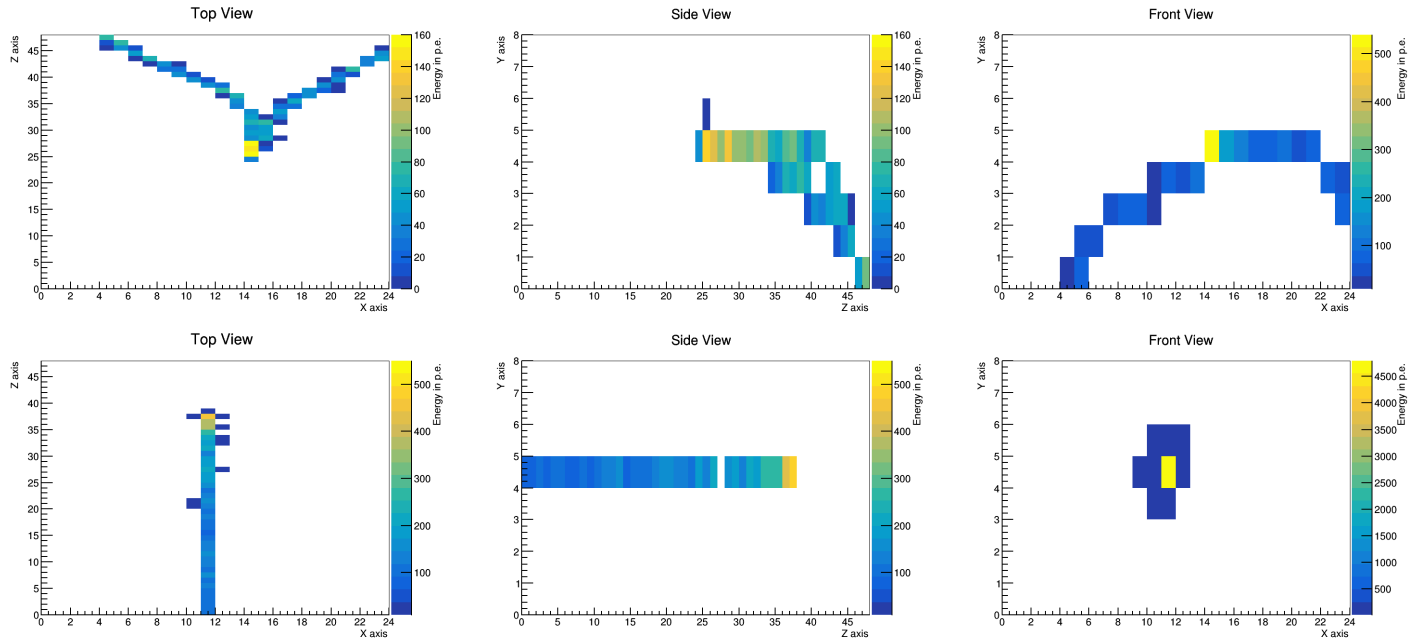


Figure A.42: Event displays showing the three two-dimensional projections of energy from a photon conversion (top) and a stopping proton (bottom). From data collected at the 2018 test beams at the CERN T9 area.

A.6.2.3 Expected Statistics

The default size of the 3DST, 2.4×2.4×2.0 m^3, gives a total target mass of 12 metric tons. Implementing a generic veto region around each side of the detector of 10 cm, gives a fiducial mass of 8.7 tons. Table A.3 gives the number of events expected per year in the FV of such a 3DST detector. The numbers given in the table are assuming the 80 GeV, 3 horn, optimized LBNF beam flux and 1.46×10^{21} POT/year.

A.6.2.4 Beam monitoring

SAND is a capable on-axis beam monitor. The plot in Figure A.43 shows the number of events seen in 2.5 days of nominal running across the face of the 3DST. The beam center can be measured to 11 cm in that time. The right plot of Figure A.38, previously shown, shows the significance of the change in the reconstructed neutrino energy spectra as a function of reconstructed energy for one week of nominal running for 1σ shifts in the transverse position of horns 1 and 2. The leptonic and hadronic energies were smeared with a parameterization appropriate for SAND.

Table A.3: This table summarizes the projected event rates per year for a 2.4 m × 2.4 m × 2.0 m 3DST detector, assuming the 80 GeV, three horn, optimized LBNF beam. A 10 cm veto region at each side was required.

Channel	ν mode	$\bar{\nu}$ mode
ν_μ CC inclusive	13.6×10^6	5.1×10^6
CCQE	2.9×10^6	1.6×10^6
CC π° inclusive	3.8×10^6	0.97×10^6
NC total	4.9×10^6	2.1×10^6
ν_μ-e$^-$ scattering	1067	1008
ν_e CC inclusive	2.5×10^5	0.56×10^5

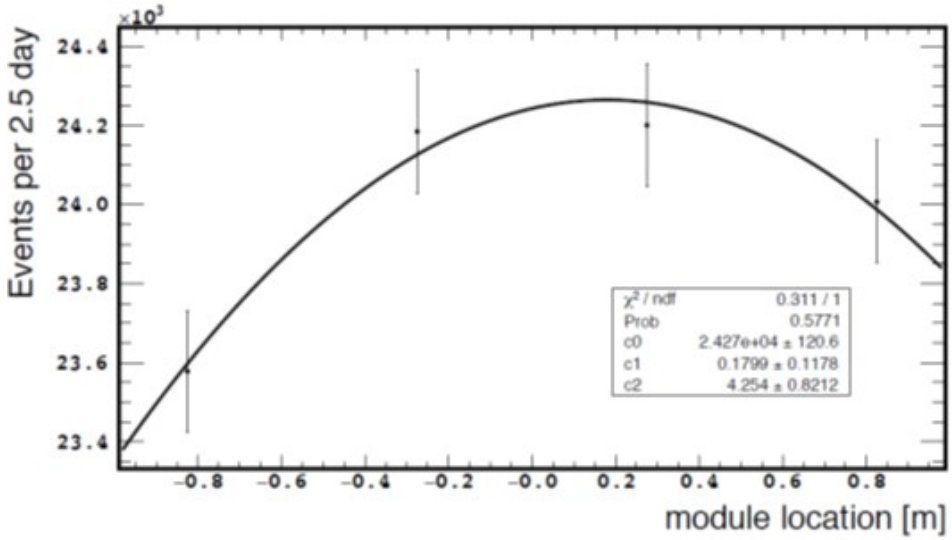


Figure A.43: Beam center determination after 2.5 days of running with SAND.

A.6.2.5 Neutron Detection Performance

The MINERvA experiment demonstrated the ability of measuring neutrons produced in neutrino interactions with a plastic scintillator detector [81]. The 3DST should be able to do this far better than MINERvA because of its high granularity and exquisite timing resolution (both much better than MINERvA).

Neutron scattering can be seen clearly in 3DST simulations. Figure A.44 shows an example of an $\overline{\nu}_\mu$ CC single charged pion interaction. The neutron-induced energy deposition due to proton recoil can be seen apart from the vertex region. Inspired by MINERvA, recent studies (described below) have shown that the 3DST can tag the presence of neutrons as well as determine the neutron energy via time-of-flight. This capability is likely to be helpful for improving both neutrino and antineutrino interaction models, and of potential use when faced with "unknown unknown" sources of systematic uncertainties. The argon-based detectors in the ND complex are expected to have some ability to detect neutrons, but studies indicate the sensitivity will be limited to regions of relatively high neutron kinetic energy (due to backgrounds and event confusion that arise at lower neutron kinetic energy where the considered event time window must be larger). The 3DST will be sensitive to neutrons down to significantly lower kinetic energy.

The neutron measurements in the 3DST are on carbon and likely will have limited direct bearing on tuning the neutron model for argon. However, the analysis of events including neutrons on an event-by-event basis may lead to improvements in the neutrino interaction model for carbon. Insights and neutrino interaction model improvements on carbon may inform the model used for argon. A notable example of this from the recent past is the 2p2h process, which is included in many current interaction models for argon even though the evidence for multi-nucleon processes was extracted from data taken on hydrocarbon targets.

Since work to date has focused on establishing the ability and quality of the neutron detection in the 3DST (as shown below), detailed studies making use of the neutron reconstruction in simulated analyses are in an early stage. Simulations show the selection of $\overline{\nu}_\mu$ CCQE events with small missing transverse momentum, using a technique described in [82], yields a sample with a substantially improved energy resolution. This sample consists of events with relatively small nuclear effects which is useful for flux determination and studies of nuclear effects in neutrino interactions. It is also expected that neutron multiplicity can be used as an indication that multi-nucleon interactions or large FSI effects are present, which may be helpful for selecting events particularly useful for exploration of the interaction model.

With a $2.4\times2.4\times2.0$ m^3 3DST detector, Figure A.45 shows the reconstructed neutron energy residual for 100 MeV kinetic energy neutron using time-of-flight with a lever arm (distance between neutron hit and neutrino vertex) larger than 0.5 m and smaller than 1 m. This study was conducted with a neutron particle gun simulation. The tail is due to both the timing resolution as well as the mis-reconstructed neutron flight distance due to non-visible interactions like elastic scattering with carbon. The neutron energy resolution is about 18%.

Neutrons produced by neutrino interactions happening outside the 3DST FV (out-FV), such as

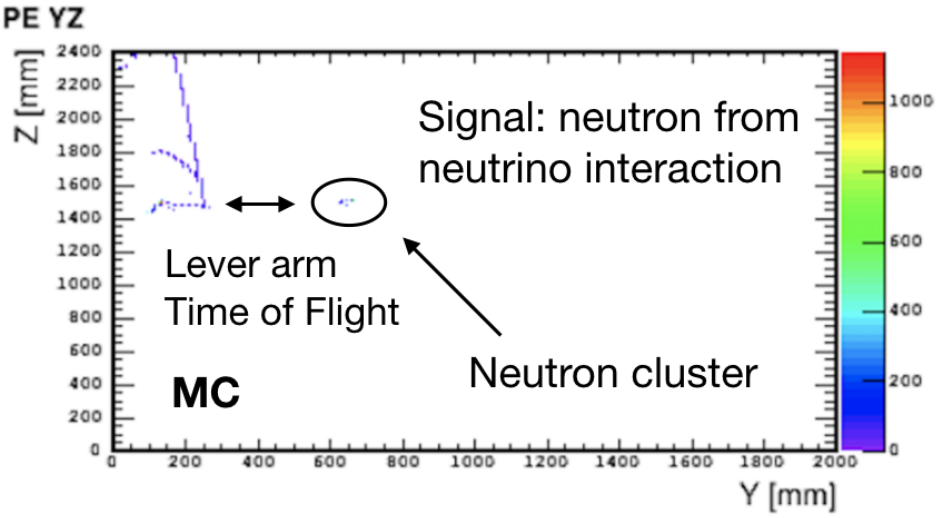


Figure A.44: An example of the antineutrino interaction in a 2.4×2.4×2.0 m^3 3DST. The number of photoelectrons (PE) is plotted. An isolated cluster of hits corresponds to a neutron indirect signature produced by the antineutrino interaction.

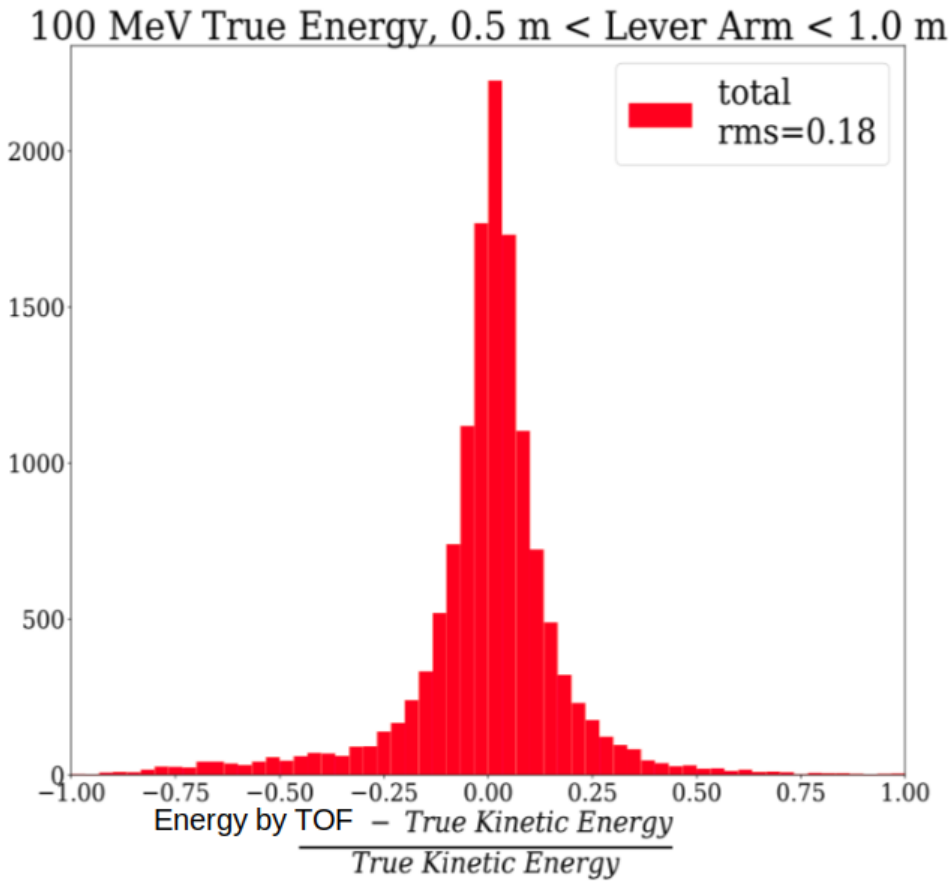


Figure A.45: Reconstructed neutron energy residual with lever arm larger than 0.5 m and smaller than 1 m for 100 MeV for a 2.4×2.4×2.0 m^3 3DST detector.

in the ECAL, Magnet, front detector, and rock can act as a background to the neutron signal from neutrino interactions. A simulation study was performed to understand the significance of background. In this study, the SAND detector was place in an underground alcove and significant dead material was placed upstream. The FV was taken to be an inner core of 1.0×1.0×1.0 m^3 of scintillator inside a 3DST of size 2.0×2.0×2.0 m^3. Neutrino beam spills of separation 1.3 s were used. Within each spill, the neutrinos were distributed uniformly in time. For each neutrino interaction occurring inside the FV, the earliest neutron-induced hit leaving an energy greater than 0.5 MeV in one cube was recorded. This threshold is thought to be conservative for the 3DST system because of the large light yield expected. If that hit was from the neutrino interaction vertex, it was considered a signal neutron-induced hit. On the other hand, if that hit was created by a particle from outside the FV, it was considered a background neutron-induced hit. Figure A.46 shows the time difference between the neutrino interaction vertex time (t_{vtx}) and the following earliest neutron-induced hit time ($t_{neutron}$). Note that a pure signal neutron sample can be obtained by cutting on ($t_{neutron} - t_{vtx}$).

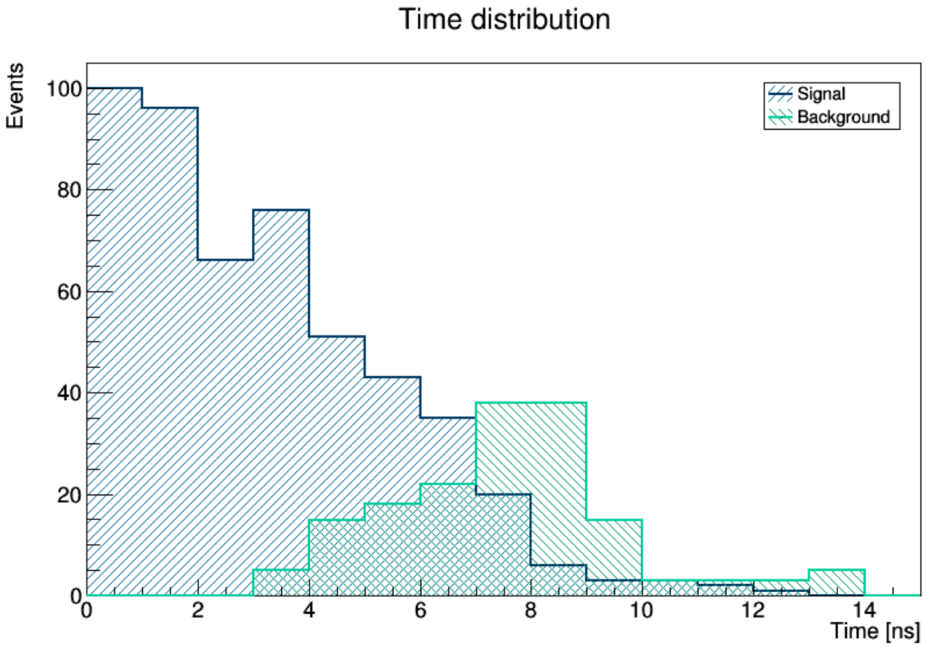


Figure A.46: Time difference between the neutrino interaction vertex time inside the 1.0×1.0×1.0 m^3 FV core of the 3DST and the earliest neutron-induced hit time. The neutron-induced hit leaves at least 0.5 MeV in a single cube. The neutron-induced background hits arise from neutrons produced in neutrino interactions outside the FV.

It is likely to be possible to veto CC and NC interactions with pions in the materials surrounding the 3DST. Such a veto would reduce backgrounds from neutrons generated by these out-FV events. In this study, such a veto was not used. This will be investigated in the future.

To quantify the background, the purity is defined as the ratio of events where the first neutron-induced hit by time is from the signal vertex to all events which have a neutron-induced hit in the FV. Figure A.47 shows the purity in time - lever arm space. Lines indicate regions populated by neutrons with different kinetic energies.

The reconstructed energy resolution in the same (time, lever arm) 2D space was studied. For

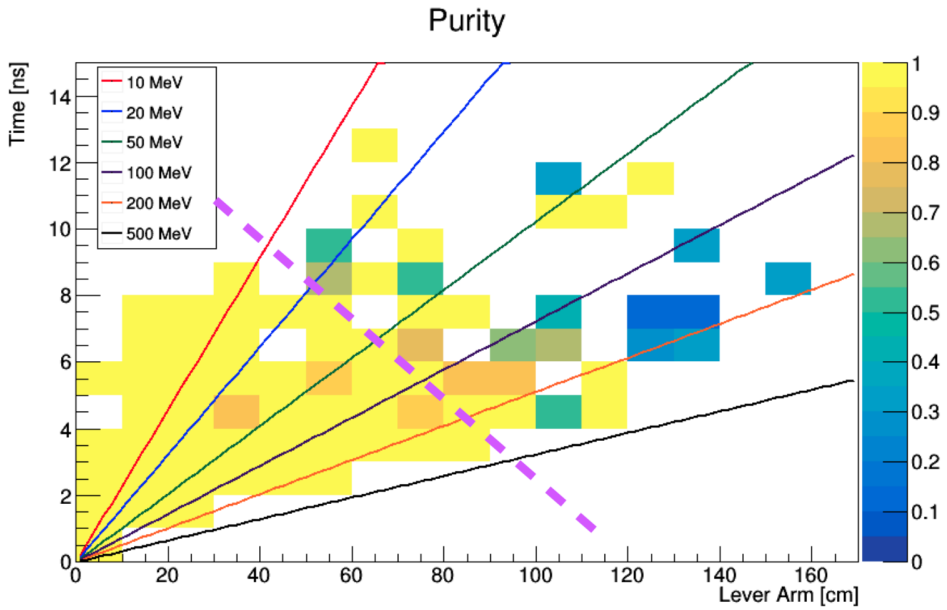


Figure A.47: Purity of the neutron-induced hit in the (time, lever arm) space. The dashed line corresponds to the cut required to select an almost 100% pure sample of signal neutrons. The solid lines are theoretical curves for neutrons with different kinetic energies. Note that this study was performed with a total volume of $2\times2\times2$ m^3. See text for details.

this work, the time was smeared by 0.58 ns, corresponding to a per fiber time resolution of 1 ns (the documented performance in the CERN test beam is 0.9 ns). Though higher light yield can help improve the time resolution, this effect has not been taken into account. Figure A.48 shows the reconstructed-by-ToF neutron energy resolution. In general, $\sim$ 20% energy resolution can be reached with most of the lever arm and time windows, in the region selected by the background cut.

A.7 Meeting the Near Detector Requirements

As discussed in Sections A.2 and A.1, the DUNE ND complex has many missions, and the components of the ND address these missions in a complementary fashion. In this section we first discuss the key overarching requirements driving the ND complex. We then discuss some thought experiments and case studies that illustrate how different parts of the complex work together. These case studies naturally suggest more detailed capabilities, performance statistics, and technical requirements that we are in the process of tabulating. Most of these require additional studies before numerical values can be tabulated.

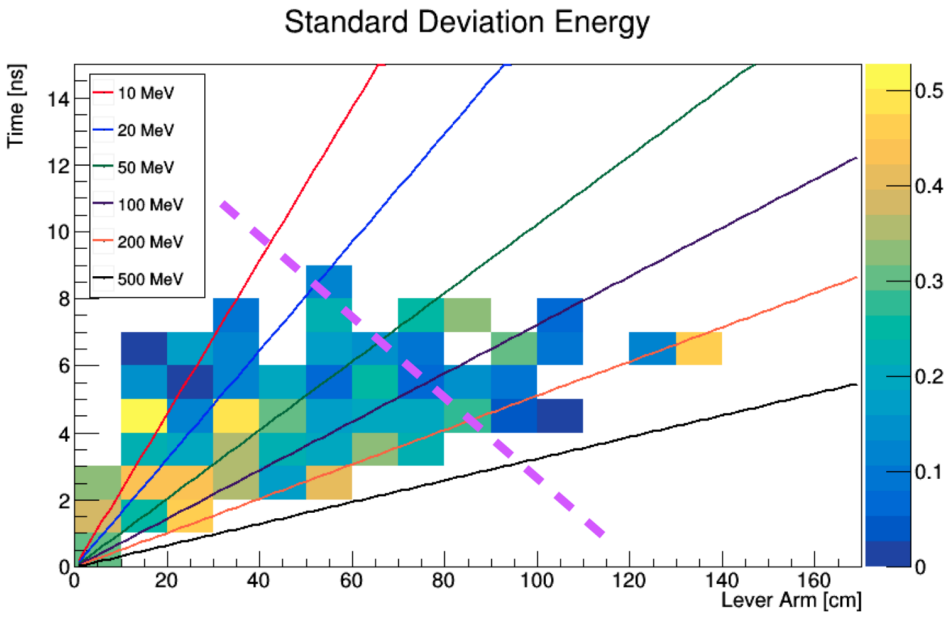


Figure A.48: Energy resolution of the neutron candidates in the (time, lever arm) space. The dashed line corresponds to the cut required to select an almost 100% pure sample of signal neutrons. The solid lines are theoretical curves for neutrons with different kinetic energies. Note that this study was performed with a total volume of 2.0×2.0×2.0 m^3. See text for details.

A.7.1 Overarching Requirements

- **Predict the neutrino spectrum at the FD:** The ND must provide a prediction for the energy spectrum of ν_μ, $\bar{\nu}_\mu$, ν_e and $\bar{\nu}_e$ at the FD. The prediction must be provided as a function of the oscillation parameters and systematic uncertainties must be small enough to achieve the required CP coverage. This is the primary requirement of the DUNE ND.
- **Measure interactions on argon:** The ND must measure neutrino interactions on argon to reduce uncertainties due to nuclear modeling. The ND must be able to determine the neutrino flavor and measure the full kinematic range of the interactions that will be seen at the FD.
- **Measure the neutrino energy:** The ND must be able to reconstruct the neutrino energy in CC events and control for any biases in energy scale or resolution, keeping them small enough to achieve the required CP coverage. These measurements must also be transferable to the FD.
- **Constrain the cross-section model:** The ND must measure neutrino cross-sections in order to constrain the cross-section model used in the oscillation analysis. In particular, cross-section mismodeling that causes incorrect FD predictions as a function of neutrino flavor and true or reconstructed energy must be constrained well enough to achieve the required CP coverage.
- **Measure neutrino fluxes:** The ND must measure neutrino fluxes as a function of flavor and neutrino energy. This allows for neutrino cross section measurements to be made and constrains the beam model and the extrapolation of neutrino energy spectra from the ND to the FD.

- **Obtain data with different fluxes:** The ND must measure neutrino interactions in different beam fluxes (especially ones with different mean energies) to deconvolve flux and cross section, verify the beam model, and guard against systematic uncertainties on the neutrino energy reconstruction.
- **Monitor the neutrino beam:** The ND must monitor the neutrino beam energy spectrum with sufficient statistics to be sensitive to intentional or accidental changes in the beam that could affect the oscillation measurement.

A.7.2 Event Rate and Flux Measurements

The three most straightforward flux measurements are described here. Other powerful but more complex techniques are described in Section A.4.

A.7.2.1 CC ν_μ and $\overline{\nu}_\mu$ Interactions

Each core component of the ND complex will have large data samples with which to constrain the flux model: ArgonCube will accumulate 3.7×10^7 CC ν_μ events per year (on axis, less when off axis); The 3DST will see 1.4×10^7 CC ν_μ per year on axis; and the HPgTPC will see 1.6×10^6 CC ν_μ events per year (on axis, less when off axis).

A.7.2.2 Intrinsic Electron Neutrino and Antineutrino Fluxes

The intrinsic ν_e and $\overline{\nu}_e$ component of the beam is discussed in Section A.4.4. This is an important component to quantify in the ND since it represents an irreducible background for the appearance oscillation analysis at the FD. The number of CC ν_e events expected in the ND per year (on axis) are 6.7×10^5, 2.5×10^5, and 2.5×10^4 for ArgonCube, the 3DST, and the HPgTPC, respectively. The primary background comes from NCπ° production. The systematics are dominated by the flux model and the interaction model (which enters in the background subtraction). In the past, statistics has been a limitation. That will not be the case for DUNE ND. With large samples, ArgonCube and the 3DST each will measure this component of the beam fairly quickly with somewhat different systematic errors. Although accumulating statistics more slowly, the HPgTPC will provide the best overall measurements the ν_e and $\overline{\nu}_e$ components of the beam. Photons mostly do not convert in the gas. This eliminates the primary background to electron (anti)neutrino identification and the accompanying interaction model uncertainty in the background subtraction. In addition, the HPgTPC has a magnetic field that allows for the sign separation of ν_e and $\overline{\nu}_e$.

A.7.2.3 Neutrino-Electron Scattering

This process and estimates of the ND performance measuring the flux using this technique is discussed in Sections A.4.1 and A.5.2.8. Measuring the flux using this process is a critical ND

mission because it is independent of nuclear effects. This is a rare process that can be used by both ArgonCube and SAND components of the ND to measure the neutrino flux. The target nucleus is irrelevant for neutrino-electron scattering. The measurement places a premium on the overall target mass (for statistics) as well as electron energy and angular resolutions. The primary backgrounds are CC interactions of intrinsic beam ν_e and NCπ° interactions. ArgonCube will do this measurement well as indicated by the results of a study shown in Figure A.16. Also, that study shows a MINERvA-like scintillator detector can do the measurement fairly well. SAND will have better angular resolution than the detector used in the study. Note that the detector and reconstruction systematic errors will be different for the two very different detectors. For such an important measurement, the duplication is good, and with many uncorrelated errors it may be possible to combine the ArgonCube data set with that from SAND for a somewhat improved constraint.

A.7.3 Control of Systematic Errors

A.7.3.1 PRISM program

The PRISM program of on- and off-axis measurements is an essential component of the ND complex and plays a key role in reducing systematic uncertainties on neutrino cross-sections and reconstructed energy. PRISM is described in Section A.5.4.

A.7.3.2 Absolute muon energy scale

The ND complex must provide knowledge of the absolute muon energy scale in the LAr ND with sufficient accuracy to meet the oscillation physics requirement and the ancillary low-nu capability. The complex will utilize MPD magnetic field survey information, as well as K_s and Λ decays to charged hadrons within the MPD, to establish the charged particle momentum scale in the MPD. The measurement will be translated to the LAr ND by tracking and momentum analyzing, in the MPD, cosmic ray muons going through the MPD into the LAr ND. The LAr ND will then measure the momentum of the muons (particularly stopping muons) by range and multiple coulomb scattering (MCS) to establish its muon momentum scale and verify the reconstruction and detector simulation.

The momentum scale will be translated to the FD by measuring and comparing the range and MCS of stopping tracks in the data and the simulation.

A.7.3.3 Hadronic Energy Scale; Hadronic Response of the LArTPC

The ND complex must calibrate the response (energy measured vs true energy) of the LAr ND and FD to the hadronic system in neutrino interactions with an accuracy to meet the oscillation physics goals. The complex will utilize a simulation benchmarked against the single particle response

measured in ProtoDUNE as a baseline. It is expected that the response will differ for different particle species and will not be constant as a function of energy. Additional calibration is needed due to the imperfectly known particle spectra in neutrino interactions, and the confusion that the LAr ND and FD will experience in identifying the composition of particles in the final state. The ND complex will accomplish the calibration by first observing ν_μ-CC interactions in the MPD. The MPD will identify the protons, charged pions and photons in the final state, and precisely reconstruct their energy via curvature in the magnetic field and, for photons, energy deposition in the calorimeter. The MPD will also observe, statistically, the energy going into neutrons using time of flight.

The muon kinematics will then be used to select one or more semi-inclusive set of events occurring in the LAr ND and MPD that have identical hadronic final states. A comparison of the reconstructed hadronic energy in the LAr ND with the precisely measured MPD calibrates the response and establishes the hadronic energy scale in LAr. It will also be possible to take the reconstructed data events from the MPD and simulate them in the LAr to compare to the actual events in the LAr. This will serve as a cross-check and as a way of studying the response. For example, one could drop any primary neutron information from the MPD reconstructed events and simulate the rest in LAr ND to compare to the LAr ND data as a way of understanding the amount of neutron energy seen by the LAr ND.

A.7.3.4 Beam Monitoring

Previous experience with the NUMI, JPARC, and Booster neutrino beams has shown that DUNE must prepare for changes in the beam that occur on timescales as short as a few days but that are not readily detected by primary and secondary beam monitors. Sudden changes in the beam have the potential of polluting the PRISM program if they occur when the LAr ND and MPD are taking data at off-axis locations. The ND complex addresses this problem with the SAND detector which will continuously measure the ν_μ and $\bar{\nu}_\mu$ energy spectrum on-axis.

A.7.3.5 LArTPC energy resolution

The PRISM measurement program demands that the energy resolution of the LAr ND and FD be as similar as possible, and that any differences can be understood and corrected for[6]. The resolution can be constrained using a similar approach as followed for the hadronic response.

A.7.3.6 LAr ND acceptance

Neutrino flavor change due to oscillation occurs over a broad energy range which demands that the ND complex is able to achieve a broad energy coverage. The LAr ND has acceptance limits (relative to the FD) at large muon angle ($\theta > 25\,\text{deg}$) and high hadronic energy due to its limited size.

[6] In fact this is true if the experiment only makes on-axis measurements.

Moreover, there is a strongly energy dependent and deep acceptance dip for $1.0 < E_\mu < 1.5\ GeV/c$ due to dead material between the active portions of the LAr ND and MPD TPC. The experiment must understand these features of the LAr ND event sample in order to use it to make predictions for the FD.

To address this shortcoming the MPD must have a nearly 4π acceptance for charged tracks and photons, a high tracking efficiency, and the ability to reconstruct events with high E_ν. A comparison of MPD and LAr ND event rates as a function of kinematic variables will verify the LAr ND acceptance model.

A.7.3.7 LAr detection thresholds

The energy threshold for detecting charged particles in LAr will be verified using the MPD in a way that is similar to the more general LAr ND acceptance study described above.

A.7.3.8 Managing pile-up

At the location of the ND, the LBNF beam is expected to generate approximately 1 neutrino interaction per 10 tons per 10 μs spill. Each of the core detectors in the ND complex can eliminate most of the pile-up background with timing from optical elements. For ArgonCube, it is estimated that there will be approximately 0.5 neutrino interactions per spill per ArgonCube module. Prompt scintillation light from the argon detected in ArCLight detectors or something similar is used to provide t_o and separate events (both connected and disconnected parts of the event). For the HPgTPC, an estimate based on a significantly (15×) more massive magnet than the superconducting option presented in section A.5.3.1.3 suggests there will be approximately 75 tracks per 10 μs spill from interactions in surrounding materials passing through the TPC. The excellent <10 ns timing resolution of the ECAL surrounding the TPC will be used to provide a t_o and to define a time window for pileup rejection. Similarly the exquisite (sub-ns) time resolution of the cubes in the 3DST can be used to generate a narrow window in time around neutrino interactions and limit the potential for overlapping events.

A.7.3.9 Energy Carried by Neutrons

The ND complex must measure or otherwise account for the neutrino energy that goes into neutrons because much of that energy ends up being undetectable by a LArTPC. The fraction of hadronic energy carried by neutrons is sizable and it also differs between ν_μ and $\bar{\nu}_\mu$: 20% vs 40% for the flux peak. To meet the oscillation physics goals these fractions must be known sufficiently well.

The complex will approach this challenge in multiple ways. First, the PRISM measurement program is required to map the relationship between true and reconstructed energy using inclusive CC scattering. These measurements are sensitive to cumulative mismodelings but may have trouble pinning down their origin. To augment the PRISM program, the MPD and SAND are required to

measure the energy carried by neutrons using calorimetry and time of flight. The MPD has the advantage of measuring neutron production off of an Ar target, but the disadvantage of doing so with lower statistics than SAND. The MPD measurement is also challenging due to the interaction rate in its calorimeter and the composition of the calorimeter driven by its multi-role nature. The advantage of SAND is in finer granularity and a better ability to reconstruct neutron energy on an event by event basis.

A.7.3.10 ν_e-CC rate and π^0/γ background

Neutral current events with a final state π^0, or a single γ, are a potentially problematic background to the ν_e and $\bar{\nu}_e$ appearance measurements. The ND complex will address this background by using the MPD to precisely measure the rate of ν_e (and $\bar{\nu}_e$) CC interactions as a function of energy and other kinematic variables. The measurement will have relatively small π^0 and γ backgrounds because photons have a low conversion probability in the MPD TPC. The LAr ND will make a similar measurement. The efficiency and background of that measurement will benchmarked using the data from the MPD.

Appendix B

ND Hall and Construction

Figure B.1 shows the current design of the underground hall as required for the near detector (ND) construction concept. The underground hall must house the detector components and allow for the required movement. The layout shows the space required for the detector, safety, and egress. This is work in progress.

The overall construction method places requirements on the conventional facilities. The primary access shaft is large enough for lowering the pressure vessel and the magnet coils. The liquid argon (LAr) cryostat is shown in its construction position near the main shaft. The multipurpose detector and the LAr detector are also shown in the on-axis position. Since the 3DST detector does not need to move for DUNE Precision Reaction-Independent Spectrum Measurement (DUNE-PRISM), it is shown in a dedicated alcove downstream of the LAr and multipurpose detectors.

The overall method of detector construction must be consistent with the construction concepts of each of the elements as outlined in previous sections. The construction method must also allow for parallel activities on major components and reduce demand on individual facilities. The underground hall will be the last facility to be completed. Therefore, insofar as possible, components must be constructed elsewhere and lowered as large assemblies.

The current assumptions for the overall construction involving the major components are listed below. Only the major components are considered, as they place the main constraints on the conventional facilities.

- The primary access shaft diameter is sufficient to accommodate the lowering of the pressure vessel and magnet coils separately. The coils and pressure vessel are constructed on the surface and lowered. This allows for remote and parallel construction.
- Two transport frames and moving systems are built in the cavern. These frames will be used to support and move the multipurpose detector and the LAr detector.
- Articulated carriers are built to carry services supporting the moving detectors.
- The components of System for on-Axis Neutrino Detection (SAND) are constructed remotely and assembled in the underground alcove cavern.

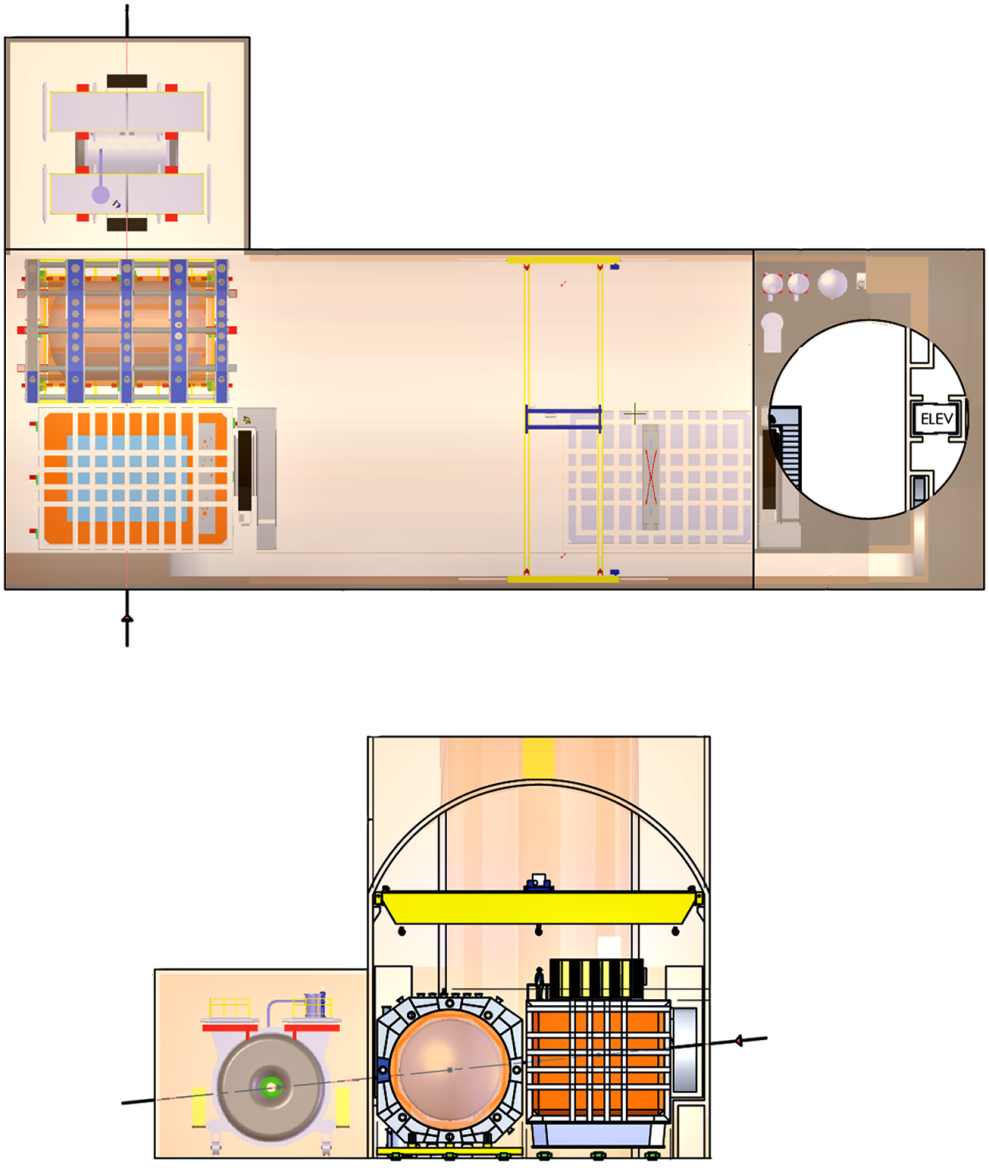


Figure B.1: Deep Underground Neutrino Experiment (DUNE) ND hall shown from above (top) and from the side transverse to the beam (bottom). The liquid argon time-projection chamber (LArTPC), multi-purpose detector (MPD), and 3D scintillator tracker (3DST) detectors are shown in position on the beam axis in both drawings.

- The five magnet coils are constructed and integrated with cryostats remotely. The magnet coils and cryostats are lowered into the ND hall and assembled together to form the magnet system on one of the transport frames.
- The pressure vessel is fabricated remotely and transported to the ND hall surface building. The TPC and some of the electromagnetic calorimeter (ECAL) components are constructed in the surface building and installed in the pressure vessel. The pressure vessel must be fabricated and certified by a qualified fabricator.
- The LAr cryostat is constructed in the cavern on the second transport frame near the main shaft. The construction of the cryostat starts by erecting and assembling the warm exoskeleton from pre-fabricated structural steel members. The warm membrane is then installed and welded in situ. Insulation is then installed inside the warm vessel. The cold membrane is the last component and is welded in situ to form the final containment vessel for the LAr. A thin window is installed on the side facing the multipurpose detector.
- The LAr modules are constructed remotely and lowered down the shaft and installed in the cryostat. The modules are inserted/extracted from the top of the cryostat using an overhead lifting device.
- The LAr services are installed.
- The high-pressure gaseous argon TPC (HPgTPC) inside the pressure vessel is lowered in the hall and then mounted inside the magnet system.
- The ECAL segments are lowered into the hall and mounted around the pressure vessel.
- Services are installed.

The basic requirement for DUNE-PRISM is that both the MPD and ArgonCube can move horizontally to a position off the beam axis. The direction of the motion is to one side of the beam and the total motion is approximately 30.5 m.

Though the MPD and ArgonCube will be moved together to different positions for operations, they will be able to move independently for engineering, construction, and maintenance reasons. The specific method of movement is not yet determined. However, it is anticipated that tracks and rollers will be used in a fashion similar to what has been done for other large particle physics detectors. The driving mechanism may be a rack and pinion drive, or a similar system, which also allows for continuous motion. It is planned that the speed of movement will allow for the entire motion to be completed in one 8-hour shift. This requires a speed of approximately 6 cm/min. If it is desired that data can be taken during the movement, a slower speed may be used. If moved at a speed of about 0.6 cm/min, an entire round trip would take about one week.

Services for both the MPD and ArgonCube will need to remain connected while moving, or be disconnected and reconnected at intermediate positions. Ideally, the former will be possible, and articulated service carriers will maintain the connections during movement. In the case of ArgonCube this presents particular challenges and will require flexible conduits.

Glossary

2p2h two particle, two hole. 8, 11, 12

3D scintillator tracker (3DST) The core part of the 3D projection scintillator tracker spectrometer in the near detector conceptual design. 5, 6, 13, 16, 59–67, 70, 73, 75, 76

analog-to-digital converter (ADC) A sampling of a voltage resulting in a discrete integer count corresponding in some way to the input. 46

ALICE A Large Ion Collider Experiment, at CERN. 44

ArCLight a light detector ArgonCube effort. 18, 22, 24, 73

ArgonCube The name of the core part of the Deep Underground Neutrino Experiment (DUNE) near detector (ND), a liquid argon time-projection chamber (LArTPC). 4, 5, 10, 16–29, 31, 32, 58, 59, 70, 71, 73, 77

ASIC application-specific integrated circuit. 21

charged current (CC) Refers to an interaction between elementary particles where a charged weak force carrier (W^+ or W^-) is exchanged. 4, 6, 11, 12, 15, 16, 24, 33–35, 37, 46, 49, 50, 58, 64, 65, 67, 69–74

CCQE charged current quasielastic interaction. 5, 9, 11, 12, 64, 65

charge parity (CP) Product of charge and parity transformations. 2, 69

charge-parity symmetry violation (CPV) Lack of symmetry in a system before and after charge and parity transformations are applied. For CP symmetry to hold, a particle turns into its corresponding antiparticle under a charge transformation, and a parity transformation inverts its space coordinates, i.e., produces the mirror image. 13

detector module The entire DUNE far detector is segmented into four modules, each with a nominal 10 kt fiducial mass. 13

Deep Underground Neutrino Experiment (DUNE) A leading-edge, international experiment for neutrino science and proton decay studies. 2–5, 7–13, 15–19, 21, 23–25, 29–31, 56, 58, 60, 68–70, 75, 76

DUNE Precision Reaction-Independent Spectrum Measurement (DUNE-PRISM) a mobile near detector that can perform measurements over a range of angles off-axis from the neutrino beam direction in order to sample many different neutrino energy distributions. 4, 5, 10, 12, 17, 54, 56, 59, 75, 77

electromagnetic calorimeter (ECAL) A detector component that measures energy deposition of traversing particles (in the near detector conceptual design). 4, 5, 13, 33, 35, 36, 38, 40–45, 50, 52, 53, 59, 61, 67, 73, 77

field cage (FC) The component of a LArTPC that contains and shapes the applied E field. 18

far detector (FD) The 70 kt total (40 kt fiducial) mass LArTPC DUNE detector, composed of four 17.5 kt total (10 kt fiducial) mass modules, to be installed at the far site at SURF in Lead, SD, USA. 2–6, 8–15, 17, 18, 34, 37, 45, 54, 56, 57, 69, 72

front-end (FE) The front-end refers a point that is "upstream" of the data flow for a particular subsystem. For example the single-phase (SP) front-end electronics is where the cold electronics meet the sense wires of the TPC and the front-end data acquisition (DAQ) is where the DAQ meets the output of the electronics. 38

Fermi National Accelerator Laboratory (Fermilab) U.S. national laboratory in Batavia, IL. It is the laboratory that hosts DUNE and serves as its near site. 18, 22

FHC forward horn current (ν_μ mode). 24–26, 31, 32

field programmable gate array (FPGA) An integrated circuit technology that allows the hardware to be reconfigured to execute different algorithms after its manufacture and deployment. 21

final-state interactions (FSI) Refers to interactions between elementary or composite particles subsequent to the initial, fundamental particle interaction, such as may occur as the products exit a nucleus. 7, 8, 11, 65

fiducial volume (FV) The detector volume within the time projection chamber (TPC) that is selected for physics analysis through cuts on reconstructed event position. 6, 22–26, 33, 34, 48, 63, 65, 67

Generates Events for Neutrino Interaction Experiments (GENIE) Software providing an object-oriented neutrino interaction simulation resulting in kinematics of the products of the interaction. 11, 45, 47, 50

high-pressure gaseous argon TPC (HPgTPC) A TPC filled with gaseous argon; a possible component of the DUNE ND. 4, 6, 13, 23, 33–38, 40–48, 53, 70, 73, 77

high voltage (HV) Generally describes a voltage applied to drive the motion of free electrons through some media, e.g., LAr. 18, 37–39

ICARUS A neutrino experiment that was located at the Laboratori Nazionali del Gran Sasso (LNGS) in Italy, then refurbished at European Organization for Nuclear Research (CERN) for re-use in the same neutrino beam from Fermi National Accelerator Laboratory (Fermilab) used by the MiniBooNE, MicroBooNE and SBND experiments. The ICARUS detector is being reassembled at Fermilab. 26

inner readout chamber (IROC) inner (radial) readout chamber for gaseous argon TPC. 38

KLOE KLOE is a e^+e^- collider detector spectrometer operated at DAFNE, the ϕ-meson factory at Frascati, Rome. In DUNE it will consist of a 26 cm Pb+scintillating fiber ECAL surrounding a cylindrical open detector region that is 4.00 m in diameter and 4.30 m long. The ECAL and detector region are embedded in a 0.6 T magnetic field created by a 4.86 m diameter superconducting coil and a 475 tonne iron yoke. 5, 61

L/E length-to-energy ratio. 6

liquid argon (LAr) Argon in its liquid phase; it is a cryogenic liquid with a boiling point of −90 °C (87 K) and density of 1.4 g/ml. 5, 18–22, 24, 28–33, 35–37, 43, 72, 75, 77

LArPix ASIC pixelated charge readout for a TPC. 21

Liquid Argon Software (LArSoft) A shared base of physics software across LArTPC experiments. 46

liquid argon time-projection chamber (LArTPC) A TPC filled with liquid argon; the basis for the DUNE far detector (FD) modules. 4–6, 12, 13, 16, 18, 21–23, 33–38, 40, 43–45, 73, 76

long-baseline (LBL) Refers to the distance between the neutrino source and the FD. It can also refer to the distance between the near and far detectors. The "long" designation is an approximate and relative distinction. For DUNE, this distance (between Fermilab and Sanford Underground Research Facility (SURF)) is approximately 1300 km. 8, 12, 33, 34

Long-Baseline Neutrino Facility (LBNF) The organizational entity responsible for developing the neutrino beam, the cryostats and cryogenics systems, and the conventional facilities for DUNE. 6, 16, 17, 21, 45, 56, 63, 64, 73

LHC Large Hadron Collider. 38

Monte Carlo (MC) Refers to a method of numerical integration that entails the statistical sam-

pling of the integrand function. Forms the basis for some types of detector and physics simulations. 46, 53, 55

MicroBooNE The LArTPC-based MicroBooNE neutrino oscillation experiment at Fermilab. 26, 36, 38

MINERvA The MINERvA neutrino cross sections experiment at Fermilab. 3, 10–12, 16, 30, 33, 58, 65, 71

MINOS A long-baseline neutrino experiment, with a near detector at Fermilab and a far detector in the Soudan mine in Minnesota, designed to observe the phenomena of neutrino oscillations (ended data runs in 2012). 3, 11, 18, 20, 58

minimum ionizing particle (MIP) Refers to a particle traversing some medium such that the particle's mean energy loss is near the minimum. 28

multi-purpose detector (MPD) A component of the near detector conceptual design; it is a magnetized system consisting of a high-pressure gaseous argon TPC (HPgTPC) and a surrounding electromagnetic calorimeter (ECAL). 4, 17, 26–28, 33–38, 40–44, 48, 58, 59, 71–74, 76, 77

Mu2e An experiment sited at Fermilab that searches for charged-lepton flavor violation and seeks to discover physics beyond the standard model (SM). 43

MWPC multi-wire proportional chamber. 38

NA61 CERN hadron production experiment. 31

neutral current (NC) Refers to an interaction between elementary particles where a neutrally charged weak force carrier (Z^0) is exchanged. 6, 9, 15, 33–35, 64, 67, 70, 71

near detector (ND) Refers to the detector(s) installed close to the neutrino source at Fermilab. 2–15, 17–21, 23–25, 29–31, 33, 34, 36, 41, 53–56, 58–61, 65, 68–77

NOvA The NOvA off-axis neutrino oscillation experiment at Fermilab. 3, 9–11, 33, 58

NuMI a set of facilities at Fermilab, collectively called "Neutrinos at the Main Injector." The NuMI neutrino beamline target system converts an intense proton beam into a focused neutrino beam. 9–11, 13, 15, 21, 30, 56, 58

outer readout chamber (OROC) outer (radial) readout chamber for gaseous argon TPC. 38

PCB printed circuit board. 41

photon detection system (PD system) The detector subsystem sensitive to light produced in

the LAr. 22

Pontecorvo-Maki-Nakagawa-Sakata (PMNS) A type of matrix that describes the mixing between mass and weak eigenstates of the neutrino. 2

ProtoDUNE Either of the two DUNE prototype detectors constructed at CERN. One prototype implements SP technology and the other dual-phase (DP). 10, 18, 24, 25

ProtoDUNE-ND a prototype DUNE ND. 18

quasi-elastic (QE) Refers to interaction between elementary particles and a nucleus in an energy range where the interaction can be modeled as occurring between constituent quarks of one nucleon and resulting in no bulk recoil of the resulting nucleus. 7, 8, 11

RHC reverse horn current ($\overline{\nu}_\mu$ mode). 31

readout chamber (ROC) readout chamber for gaseous argon TPC. 38, 39

System for on-Axis Neutrino Detection (SAND) The beam monitor component of the near detector that remains on-axis at all times and serves as a dedicated neutrino spectrum monitor. 5, 59, 63, 64, 67, 71–75

Short-Baseline Neutrino (SBN) A Fermilab program consisting of three collaborations, MicroBooNE, SBND, and ICARUS, to perform sensitive searches for ν_e appearance and ν_μ disappearance in the Booster Neutrino Beam. 3

silicon photomultiplier (SiPM) A solid-state avalanche photodiode sensitive to single photoelectron signals. 22, 41

SP module single-phase DUNE FD module. 45, 46

SRC short-range correlated nucleon-nucleon interactions. 7, 8

SSC The Superconducting Super Collider was to be a huge underground ring complex beneath the area near Waxahachie, Texas, USA, that would have been the worldâĂŹs most energetic particle accelerator. It was begun in 1990, but canceled by the U.S. Congress in 1993 (scientificamerican.com Oct 2013). 43

T2K T2K (Tokai to Kamioka) is a long-baseline neutrino experiment in Japan studying neutrino oscillations. 3, 9, 10, 15, 33, 60

time projection chamber (TPC) A type of particle detector that uses an E field together with a sensitive volume of gas or liquid, e.g., liquid argon (LAr), to perform a 3D reconstruction of a particle trajectory or interaction. The activity is recorded by digitizing the waveforms of

current induced on the anode as the distribution of ionization charge passes by or is collected on the electrode. 5, 9, 18, 19, 21, 22, 24, 38, 39, 59, 61, 73

UA1 UA1 (Underground Area 1) was a particle detector at CERN's Super Proton Synchrotron (SPS). It ran from 1981 until 1990, when the SPS was used as a proton-antiproton collider, searching for traces of W and Z particles in collisions. (CERN) The UA1 dipole magnet was reused in the NOMAD experiment and currently provides the magnetic field for the T2K ND280 detector. 42

wavelength-shifting (WLS) A material or process by which incident photons are absorbed by a material and photons are emitted at a different, typically longer, wavelength. 60

References

[1] A. Friedland and S. W. Li, "Understanding the energy resolution of liquid argon neutrino detectors," *Phys. Rev.* **D99** no. 3, (2019) 036009, arXiv:1811.06159 [hep-ph].

[2] DUNE HPgTPC working group, "High-Pressure Argon gas TPC Option for the DUNE Near Detector," DUNE doc 6652, 2018. https://docs.dunescience.org/cgi-bin/private/ShowDocument?docid=6652&asof=2019-11-1.

[3] R. A. Smith and E. J. Moniz, "NEUTRINO REACTIONS ON NUCLEAR TARGETS," *Nucl. Phys.* **B43** (1972) 605. [Erratum: Nucl. Phys.B101,547(1975)].

[4] A. Bodek, M. E. Christy, and B. Coopersmith, "Effective spectral function for quasielastic scattering on nuclei from ${}^{2}_{1}$H to ${}^{208}_{82}$Pb," *AIP Conf. Proc.* **1680** (2015) 020003, arXiv:1409.8545 [nucl-th].

[5] **MINERvA** Collaboration, D. Ruterbories *et al.*, "Measurement of Quasielastic-Like Neutrino Scattering at $\langle E_\nu \rangle \sim 3.5$ GeV on a Hydrocarbon Target," *Phys. Rev.* **D99** no. 1, (2019) 012004, arXiv:1811.02774 [hep-ex].

[6] **T2K** Collaboration, K. Abe *et al.*, "Search for CP Violation in Neutrino and Antineutrino Oscillations by the T2K Experiment with 2.2×10^{21} Protons on Target," *Phys. Rev. Lett.* **121** no. 17, (2018) 171802, arXiv:1807.07891 [hep-ex].

[7] **NOvA** Collaboration, M. A. Acero *et al.*, "New constraints on oscillation parameters from ν_e appearance and ν_μ disappearance in the NOvA experiment," *Phys. Rev.* **D98** (2018) 032012, arXiv:1806.00096 [hep-ex].

[8] J. Wolcott, "Impact of cross section modeling on NOvA oscillation analyses." https://indico.cern.ch/event/703880/contributions/3159021/attachments/1735451/2806895/2018-10-17_Wolcott_XS_unc_on_NOvA_osc_-_NuInt.pdf, 2018.

[9] D. Jena, "MINERvA adventures in flux determination," in *NuInt 2018*, Fermilab. Oct., 2018. https://indico.cern.ch/event/703880/contributions/3159052/attachments/1735968/2817449/NuInt2018_DeepikaJena_Flux.pdf.

[10] **MiniBooNE** Collaboration, A. A. Aguilar-Arevalo *et al.*, "Measurement of the Neutrino

Neutral-Current Elastic Differential Cross Section on Mineral Oil at $E_\nu \sim 1$ GeV," *Phys. Rev.* **D82** (2010) 092005, arXiv:1007.4730 [hep-ex].

[11] **K2K** Collaboration, R. Gran *et al.*, "Measurement of the quasi-elastic axial vector mass in neutrino-oxygen interactions," *Phys. Rev.* **D74** (2006) 052002, arXiv:hep-ex/0603034 [hep-ex].

[12] **MINOS** Collaboration, P. Adamson *et al.*, "Study of quasielastic scattering using charged-current ν_μ-iron interactions in the MINOS near detector," *Phys. Rev.* **D91** no. 1, (2015) 012005, arXiv:1410.8613 [hep-ex].

[13] M. Martini, M. Ericson, and G. Chanfray, "Energy reconstruction effects in neutrino oscillation experiments and implications for the analysis," *Phys. Rev.* **D87** no. 1, (2013) 013009, arXiv:1211.1523 [hep-ph].

[14] **NOvA** Collaboration, P. Adamson *et al.*, "First measurement of muon-neutrino disappearance in NOvA," *Phys. Rev.* **D93** no. 5, (2016) 051104, arXiv:1601.05037 [hep-ex].

[15] C. Andreopoulos *et al.*, "The GENIE Neutrino Monte Carlo Generator," *Nucl. Instrum. Meth.* **A614** (2010) 87–104, arXiv:0905.2517 [hep-ph].

[16] A. Bodek and J. L. Ritchie, "Further Studies of Fermi Motion Effects in Lepton Scattering from Nuclear Targets," *Phys. Rev.* **D24** (1981) 1400.

[17] S. Dytman, "Neutrino event generators," *AIP Conf. Proc.* **896** no. 1, (2007) 178–184.

[18] P. Rodrigues, C. Wilkinson, and K. McFarland, "Constraining the GENIE model of neutrino-induced single pion production using reanalyzed bubble chamber data," *Eur. Phys. J.* **C76** no. 8, (2016) 474, arXiv:1601.01888 [hep-ex].

[19] J. Nieves, J. E. Amaro, and M. Valverde, "Inclusive quasi-elastic neutrino reactions," *Phys. Rev.* **C70** (2004) 055503, arXiv:nucl-th/0408005 [nucl-th]. [Erratum: Phys. Rev.C72,019902(2005)].

[20] R. Gran, "Model Uncertainties for Valencia RPA Effect for MINERvA," arXiv:1705.02932 [hep-ex].

[21] J. Nieves, I. Ruiz Simo, and M. J. Vicente Vacas, "Inclusive Charged–Current Neutrino–Nucleus Reactions," *Phys. Rev.* **C83** (2011) 045501, arXiv:1102.2777 [hep-ph].

[22] R. Gran, J. Nieves, F. Sanchez, and M. J. Vicente Vacas, "Neutrino-nucleus quasi-elastic and 2p2h interactions up to 10 GeV," *Phys. Rev.* **D88** no. 11, (2013) 113007, arXiv:1307.8105 [hep-ph].

[23] J. Schwehr, D. Cherdack, and R. Gran, "GENIE implementation of IFIC Valencia model for QE-like 2p2h neutrino-nucleus cross section," arXiv:1601.02038 [hep-ph].

[24] M. Alam *et al.*, "GENIE Production Release 2.10.0," arXiv:1512.06882 [hep-ph].

[25] A. Bercellie, "Pion production at MINERvA." https://indico.cern.ch/event/703880/contributions/3157434/attachments/1734544/2808228/Minerva_LE_Pions_NUINT2018.pdf, 2018.

[26] **MINERvA** Collaboration, O. Altinok *et al.*, "Measurement of ν_μ charged-current single π^0 production on hydrocarbon in the few-GeV region using MINERvA," *Phys. Rev.* **D96** no. 7, (2017) 072003, arXiv:1708.03723 [hep-ex].

[27] L. Aliaga, O. Altinok, A. Bercellie, A. Bodek, A. Bravar, *et al.*, "Single neutral pion production by charged-current $\bar{\nu}_\mu$ interactions on hydrocarbon at $\langle E_\nu \rangle = 3.6$ GeV." 2015.

[28] **MINERvA** Collaboration, C. L. McGivern *et al.*, "Cross sections for ν_μ and $\bar{\nu}_\mu$ induced pion production on hydrocarbon in the few-GeV region using MINERvA," *Phys. Rev.* **D94** no. 5, (2016) 052005, arXiv:1606.07127 [hep-ex].

[29] NOvA and M. collaborations, "Private communication.".

[30] M. Day and K. S. McFarland, "Differences in quasielastic cross sections of muon and electron neutrinos," *Phys. Rev. D* **86** (Sep, 2012) 053003. http://link.aps.org/doi/10.1103/PhysRevD.86.053003.

[31] M. Kordosky. Private communication regarding a MINERvA analysis. It should at least be in the arXiv by Spring 2019.

[32] R. Belusevic and D. Rein, "Neutrino Reactions in the Low Y Region," *Phys. Rev.* **D38** (1988) 2753–2757.

[33] A. Bodek, U. Sarica, D. Naples, and L. Ren, "Methods to Determine Neutrino Flux at Low Energies:Investigation of the Low ν Method," *Eur. Phys. J.* **C72** (2012) 1973, arXiv:1201.3025 [hep-ex].

[34] **DUNE** Collaboration, R. Acciarri *et al.*, "Long-Baseline Neutrino Facility (LBNF) and Deep Underground Neutrino Experiment (DUNE)," arXiv:1601.05471 [physics.ins-det].

[35] **DUNE** Collaboration, R. Acciarri *et al.*, "Long-Baseline Neutrino Facility (LBNF) and Deep Underground Neutrino Experiment (DUNE)," arXiv:1512.06148 [physics.ins-det].

[36] **ArgonCube** Collaboration, C. Amsler *et al.*, "ArgonCube: a novel, fully-modular approach for the realization of large-mass liquid argon TPC neutrino detectors," Tech. Rep. CERN-SPSC-2015-009. SPSC-I-243, CERN, Geneva, Feb, 2015. https://cds.cern.ch/record/1993255.

[37] J. Asaadi *et al.*, "First Demonstration of a Pixelated Charge Readout for Single-Phase

Liquid Argon Time Projection Chambers," arXiv:1801.08884 [physics.ins-det].

[38] A. Krieger, D. Dwyer, M. Garcia-Sciveres, D. Gnani, and C. Grace, "A micropower readout ASIC for pixelated liquid Ar TPCs," in *Topical Workshop on Electronics for Particle Physics*. 2017. https://pos.sissa.it/313.

[39] M. Auger, Y. Chen, A. Ereditato, D. Goeldi, I. Kreslo, D. Lorca, M. Luethi, T. Mettler, J. R. Sinclair, and M. S. Weber, "ArCLight-A Compact Dielectric Large-Area Photon Detector," *Instruments* **2** no. 1, (2018) 3, arXiv:1711.11409 [physics.ins-det].

[40] M. Auger, R. Berner, Y. Chen, A. Ereditato, D. Goeldi, P. P. Koller, I. Kreslo, D. Lorca, T. Mettler, F. Piastra, J. R. Sinclair, M. Weber, , C. Wilkinson, D. A. Dwyer, S. Kohn, P. Madigan, C. M. Marshall, and J. Asaadi, "A Concept for the Fourth DUNE Far Detector Module," DUNE doc 10419, 2018. https://docs.dunescience.org/cgi-bin/private/ShowDocument?docid=10419&asof=2019-11-1.

[41] A. Ereditato, C. C. Hsu, S. Janos, I. Kreslo, M. Messina, C. Rudolf von Rohr, B. Rossi, T. Strauss, M. S. Weber, and M. Zeller, "Design and operation of ARGONTUBE: a 5 m long drift liquid argon TPC," *JINST* **8** (2013) P07002, arXiv:1304.6961 [physics.ins-det].

[42] M. Zeller *et al.*, "First measurements with ARGONTUBE, a 5m long drift Liquid Argon TPC," *Nucl. Instrum. Meth.* **A718** (2013) 454–458.

[43] A. Ereditato *et al.*, "Performance of cryogenic charge readout electronics with the ARGONTUBE LAr TPC," *JINST* **9** no. 11, (2014) P11022, arXiv:1408.7046 [physics.ins-det].

[44] **LArIAT** Collaboration, F. Cavanna, M. Kordosky, J. Raaf, and B. Rebel, "LArIAT: Liquid Argon In A Testbeam." arXiv:1406.5560, 2014.

[45] M. Auger *et al.*, "ProtoDUNE-ND: proposal to place the ArgonCube 2x2 Demonstrator on-axis in NuMI," DUNE doc 12571, 2019. https://docs.dunescience.org/cgi-bin/private/ShowDocument?docid=12571N&asof=2019-11-1.

[46] **Particle Data Group** Collaboration, M. Tanabashi *et al.*, "Review of Particle Physics," *Phys. Rev.* **D98** no. 3, (2018) 030001.

[47] E. Tuncer, I. Sauers, D. R. James, and A. R. Ellis, "Electrical insulation characteristics of glass fiber reinforced resins," *IEEE Transactions on Applied Superconductivity* **19** no. 3, (June, 2009) 2359–2362.

[48] P. Adamson *et al.*, "The NuMI Neutrino Beam," *Nucl. Instrum. Meth.* **A806** (2016) 279–306, arXiv:1507.06690 [physics.acc-ph].

[49] E. Grace and J. A. Nikkel, "Index of refraction, Rayleigh scattering length, and Sellmeier coefficients in solid and liquid argon and xenon," *Nucl. Instrum. Meth.* **A867** (2017) 204–208, arXiv:1502.04213 [physics.ins-det].

[50] C. M. Marshall, "LArTPC - optimal height of detector," in *DUNE Collaboration Meeting*. 2, 2018. https://indico.fnal.gov/event/14581/session/5/contribution/86.

[51] T. Heindl, T. Dandl, A. Fedenev, M. Hofmann, R. KrÃijcken, L. Oberauer, W. Potzel, J. Wieser, and A. Ulrich, "Table-top setup for investigating the scintillation properties of liquid argon," *JINST* **6** (2011) P02011, arXiv:1511.07720 [physics.ins-det].

[52] S. Kubota, M. Hishida, M. Suzuki, and J.-z. Ruan(Gen), "Dynamical behavior of free electrons in the recombination process in liquid argon, krypton, and xenon," *Phys. Rev. B* **20** (Oct, 1979) 3486–3496. https://link.aps.org/doi/10.1103/PhysRevB.20.3486.

[53] A. Hitachi, T. Takahashi, N. Funayama, K. Masuda, J. Kikuchi, and T. Doke, "Effect of ionization density on the time dependence of luminescence from liquid argon and xenon," *Phys. Rev. B* **27** (May, 1983) 5279–5285. https://link.aps.org/doi/10.1103/PhysRevB.27.5279.

[54] Gushchin *et al.*, "Electron dynamics in condensed argon and xenon," *Journal of Experimental and Theoretical Physics* **55** no. 4, (4, 1982) 650.

[55] V. Chepel and H. Araujo, "Liquid noble gas detectors for low energy particle physics," *JINST* **8** (2013) R04001, arXiv:1207.2292 [physics.ins-det].

[56] **DUNE** Collaboration, B. Abi *et al.*, "The Single-Phase ProtoDUNE Technical Design Report," arXiv:1706.07081 [physics.ins-det].

[57] **MicroBooNE** Collaboration, P. Abratenko *et al.*, "Determination of muon momentum in the MicroBooNE LArTPC using an improved model of multiple Coulomb scattering," *JINST* **12** no. 10, (2017) P10010, arXiv:1703.06187 [physics.ins-det].

[58] **MINERvA** Collaboration, J. Park *et al.*, "Measurement of Neutrino Flux from Neutrino-Electron Elastic Scattering," *Phys. Rev.* **D93** no. 11, (2016) 112007, arXiv:1512.07699 [physics.ins-det].

[59] C. M. Marshall, K. S. McFarland, and C. Wilkinson, "Neutrino-electron elastic scattering for flux determination at the dune oscillation experiment," *Phys. Rev. D* **101** (Feb, 2020) 032002. https://link.aps.org/doi/10.1103/PhysRevD.101.032002.

[60] **NA61/SHINE** Collaboration, A. Laszlo, "The NA61/SHINE Experiment at the CERN SPS," *Nucl. Phys.* **A830** (2009) 559C–562C, arXiv:0907.4493 [nucl-ex].

[61] **ALICE** Collaboration, G. Dellacasa *et al.*, "ALICE: Technical design report of the time projection chamber," Tech. Rep. CERN-OPEN-2000-183, CERN-LHCC-2000-001, 2000.

[62] J. Alme *et al.*, "The ALICE TPC, a large 3-dimensional tracking device with fast readout for ultra-high multiplicity events," *Nucl. Instrum. Meth.* **A622** (2010) 316–367, arXiv:1001.1950 [physics.ins-det].

[63] F. Simon, C. Soldner, and L. Weuste, "T3B âĂŤ an experiment to measure the time structure of hadronic showers," *JINST* **8** (2013) P12001, arXiv:1309.6143 [physics.ins-det].

[64] **CALICE** Collaboration, C. Adloff *et al.*, "Construction and Commissioning of the CALICE Analog Hadron Calorimeter Prototype," *JINST* **5** (2010) P05004, arXiv:1003.2662 [physics.ins-det].

[65] L. Emberger and F. Simon, "A highly granular calorimeter concept for long baseline near detectors," *J. Phys. Conf. Ser.* **1162** no. 1, (2019) 012033, arXiv:1810.03677 [physics.ins-det].

[66] J. Layter, "Results from pep-4 tpc," in *Electroweak Effects at High Energies*, pp. 201–213. Springer, 1985.

[67] **PEP4** Collaboration, D. H. Stork, "First Operation of the TPC Facility at PEP," *J. Phys. Colloq.* **43** no. C3, (1982) 42.

[68] **TPC/Two Gamma** Collaboration, R. J. Madaras *et al.*, "SPATIAL RESOLUTION OF THE PEP-4 TIME PROJECTION CHAMBER," *IEEE Trans. Nucl. Sci.* **30** (1983) 76–81.

[69] **ALICE** Collaboration, C. W. Fabjan *et al.*, "ALICE: Physics performance report, volume II," *J. Phys.* **G32** (2006) 1295–2040.

[70] C. Cheshkov, "Fast Hough-transform track reconstruction for the ALICE TPC," *Nucl. Instrum. Meth.* **A566** (2006) 35–39.

[71] C. Grupen, "Physics of particle detection," *AIP Conf. Proc.* **536** no. 1, (2000) 3–34, arXiv:physics/9906063 [physics].

[72] C. Lippmann, "Performance of the ALICE Time Projection Chamber," *Phys. Procedia* **37** (2012) 434–441.

[73] **ALICE** Collaboration, B. Abelev *et al.*, "Performance of the ALICE Experiment at the CERN LHC," *Int. J. Mod. Phys.* **A29** (2014) 1430044, arXiv:1402.4476 [nucl-ex].

[74] **GEANT4** Collaboration, S. Agostinelli *et al.*, "GEANT4: A Simulation toolkit," *Nucl. Instrum. Meth. A* **506** (2003) 250–303.

[75] "Garsoft redmine repository." https://cdcvs.fnal.gov/redmine/projects/garsoft. Accessed Feb. 19, 2019.

[76] A. Holin, "NUMI beam lessons and work in progress MINOS/MINOS+." https://indico.cern.ch/event/674901/contributions/2799260/, 2017.

[77] J. Hylen, "NuMI Horn 1 mis-alignment." https://indico.fnal.gov/event/13292/, 2016.

[78] A. Blondel *et al.*, "A fully active fine grained detector with three readout views," *JINST* **13** no. 02, (2018) P02006, arXiv:1707.01785 [physics.ins-det].

[79] **T2K** Collaboration, K. Abe *et al.*, "T2K ND280 Upgrade - Technical Design Report," arXiv:1901.03750 [physics.ins-det].

[80] O. Mineev *et al.*, "Beam test results of 3D fine-grained scintillator detector prototype for a T2K ND280 neutrino active target," *Nucl. Instrum. Meth.* **A923** (2019) 134–138, arXiv:1808.08829 [physics.ins-det].

[81] **MINERvA** Collaboration, M. Elkins *et al.*, "Neutron measurements from anti-neutrino hydrocarbon reactions," arXiv:1901.04892 [hep-ex].

[82] **T2K** Collaboration, K. Abe *et al.*, "Characterization of nuclear effects in muon-neutrino scattering on hydrocarbon with a measurement of final-state kinematics and correlations in charged-current pionless interactions at T2K," *Phys. Rev.* **D98** no. 3, (2018) 032003, arXiv:1802.05078 [hep-ex].